THE GROWTH AND CHARACTERIZATION OF GROUP IV ALLOYS FOR NEAR TO MID-INFRARED DETECTORS

by

John Thomas Hart

A dissertation submitted to the Faculty of the University of Delaware in partial fulfillment of the requirements for the degree of Doctor of Philosophy in Electrical and Computer Engineering

Fall 2016

© 2016 John Thomas Hart
All Rights Reserved

ProQuest Number: 10250359

All rights reserved

INFORMATION TO ALL USERS
The quality of this reproduction is dependent upon the quality of the copy submitted.

In the unlikely event that the author did not send a complete manuscript
and there are missing pages, these will be noted. Also, if material had to be removed,
a note will indicate the deletion.

ProQuest 10250359

Published by ProQuest LLC (2017). Copyright of the Dissertation is held by the Author.

All rights reserved.
This work is protected against unauthorized copying under Title 17, United States Code
Microform Edition © ProQuest LLC.

ProQuest LLC.
789 East Eisenhower Parkway
P.O. Box 1346
Ann Arbor, MI 48106 – 1346

THE GROWTH AND CHARACTERIZATION

OF GROUP IV ALLOYS FOR NEAR TO

MID-INFRARED DETECTORS

by

John Thomas Hart

Approved: _____

Kenneth E. Barner, Ph.D.
Chair of the Department of Electrical and Computer Engineering

Approved: _____

Babatunde A. Ogunnaike, Ph.D.
Dean of the College of Engineering

Approved: _____

Ann L. Ardis, Ph.D.
Senior Vice Provost for Graduate and Professional Education

I certify that I have read this dissertation and that in my opinion it meets the academic and professional standard required by the University as a dissertation for the degree of Doctor of Philosophy.

Signed: _____

James Kolodzey, Ph.D.
Professor in charge of dissertation

I certify that I have read this dissertation and that in my opinion it meets the academic and professional standard required by the University as a dissertation for the degree of Doctor of Philosophy.

Signed: _____

Matt Doty, Ph.D.
Member of dissertation committee

I certify that I have read this dissertation and that in my opinion it meets the academic and professional standard required by the University as a dissertation for the degree of Doctor of Philosophy.

Signed: _____

Yuping Zeng, Ph.D.
Member of dissertation committee

I certify that I have read this dissertation and that in my opinion it meets the academic and professional standard required by the University as a dissertation for the degree of Doctor of Philosophy.

Signed: _____

Gary Katulka, Ph.D.
Member of dissertation committee

I certify that I have read this dissertation and that in my opinion it meets the academic and professional standard required by the University as a dissertation for the degree of Doctor of Philosophy.

Signed: _____

James Nakos, Ph.D.
Member of dissertation committee

ACKNOWLEDGMENTS

PhD research does not happen in a vacuum; I have a lot of people to thank for the many years of both intellectual and emotional support. Without the people below, and many more that are unnamed, this dissertation, and my life, would be as empty as the vacuum systems I've spent so much time with.

First and foremost, I'd like to thank my fiancé Yulia Kushner for supporting me in moving across the country to follow my dreams. Yulia also deserves credit for the incredible patience and love it takes to have a fiancé in graduate school for so long. I'd also like to thank my family for the lifetime of support and for always encouraging me to pursue my interests. To Dr. Jon Church, Dr. Ken Schmieder, Dr. Chris McGann, and Dr. Nicole Kotulak thank you for the movie nights, the rock climbing, the conversations, and the beer.

I'd like to thank my advisor Dr. James Kolodzey for the years of support and mentorship throughout my PhD. Specifically, I'd like to thank you for creating a group dynamic that nurtures independence and self-motivation. I thank my dissertation committee members, Dr. Matt Doty, Dr. James Nakos, Dr. Yuping Zeng, and Dr. Gary Katulka, for their extensive time and numerous meaningful discussions. My group members throughout the years have been invaluable research partners. I extend my thanks to Dr. Ramsey Hazbun, who has been my lab buddy from day-one. To Ryan Hickey, whose hard work on the MBE is the reason we all can graduate. Thanks to both of you for not only being great lab partners but also great friends. I'd also like to thank my other group members throughout the years: David Eldridge, Dainan Zhang,

Dominic Imbrenda, Dr. Nupur Bhargava, Dr. Jay Gupta, Dr. Matt Coppinger, and Dr. Sangcheol Kim. Kjeld Krag-Jensen deserves much credit for being the backbone of everything DuPont hall, who deserves more thanks from all of us PhD students than I can properly express. Kevin Schreve deserves many thanks for being the go-to guy for so many questions over the years.

There are many people outside of the University of Delaware that I had the pleasure of working with. I'd like to begin by thanking Dr. Thomas Adam from SUNY Albany, for always being an excellent resource for our group and really coming through in a great way for help with the UHV-CVD. Dr. Stefan Zollner and Nalin Fernando from New Mexico State University for VASE measurements and for making collaboration easy, interesting, and mutually rewarding. Dr. Yihwan Kim and Dr. Yi-Chiau Huang from Applied Materials for providing RPCVD grown GeSn samples for the photoconductor work. Dr. Gary Katulka and his team from the Army Research Labs for interesting discussions as well as fun and motivating projects to work on. The Airliquide/ Voltaix team for funding and being an excellent knowledge base for our CVD research. Dave Beatson for interesting discussion, financial support, and being a source of great motivation. The IBM/ Global Foundries team for an internship that was both fun and intellectually rewarding, as well as doing an excellent job of making my time up there absolutely invaluable. I'd also like to thank Dr. Dave Harame for being instrumental in making my internship happen and for being a role model for breadth of knowledge, goal setting, and persistence.

The knowledge and experiences I've gained and shared with everyone are, and forever will be, my most treasured possessions in life.

TABLE OF CONTENTS

Appendix

LIST OF TABLES

LIST OF FIGURES

ABSTRACT

Near infrared and mid infrared optoelectronic devices have become increasingly important for the telecommunications, security, and medical imaging industries. An infrared system fully integrated in a silicon chip manufactured in a high-volume CMOS foundry is therefore a much desired technology. Such a technology would allow the integration of mid-IR technology with new functionality, lower costs, smaller size, weight and power, and higher reliability. The focus of this dissertation is on the advancement of low temperature Group IV epitaxy of tin containing alloys for use in near to mid- infrared technologies. To that end, various epitaxial techniques and improvements were made and several detector device structures were characterized.

Low temperature epitaxy is vital to achieve Sn containing Group IV films, and both ultra-high vacuum chemical vapor deposition (UHV-CVD) and molecular beam epitaxy (MBE) were utilized to this end. New precursors are needed in CVD to maintain film growth at reduced temperatures. The novel precursors tetrasilane and digermane were studied for their low temperature compatibility. Crystalline silicon and silicon germanium alloys were deposited and characterized, finding high quality, bulk-like films. Tin-chloride was investigated as a possible Sn precursor, but was found to etch Ge. Multiple innovations in GeSn epitaxy in MBE were made, including both n- and p-type doping and higher Sn concentrations than those previously achieved for devices.

While careful consideration needed to be taken into account for the growth of GeSn, normal clean room processing was not found to have any adverse effect on the material. Photoconductive and photodiode type detectors of GeSn films on Si substrates were fabricated. The wavelength response of the material was measured to continually increase into the mid-infrared as the Sn content was increased, reaching almost 4μm for a 15.6% Sn device at room temperature. The responsivity of the detectors was measured, and characterized as a function of temperature. The bandgap was extracted as a function of alloy concentration and strain, and was found to closely follow what was predicted in literature. The work presented here advances the state of the art for high Sn content films, moving towards successful commercial integration and manufacturability.

Chapter 1

INTRODUCTION AND MOTIVATION

1.1 Introduction: Near to Mid-IR Applications

There are many useful applications in the near to mid- infrared range including, but not limited to, gas detection and environmental monitoring [1][2], night-fighting equipment [3], astronomy [4], ranging [5], bio agent and medical sensing [6], solar power [7]–[9], and industrial process control [10]. One additional potential use of near to mid-IR imaging that was investigated at the University of Delaware, was that of portable dead reckoning cameras that are tolerant of adverse environmental conditions. To illustrate the utility of infrared imaging, Figure 1.1 shows the transmission % of infrared light through smoke and fog, showing a transmission window through both fog and smoke in the 2.5 – 3 μm wavelength region.

A mid-IR system fully integrated in a silicon chip manufactured in a high-volume CMOS foundry is therefore a much desired technology as it would allow the integration of mid-IR technology with new functionality, lower costs, smaller size, weight and power, and higher reliability [11]. The remainder of this chapter builds the motivation behind alloying Sn into the more typical Group IV semiconductors Ge and Si, in order to achieve integrated MIR light sensors and light emitters.

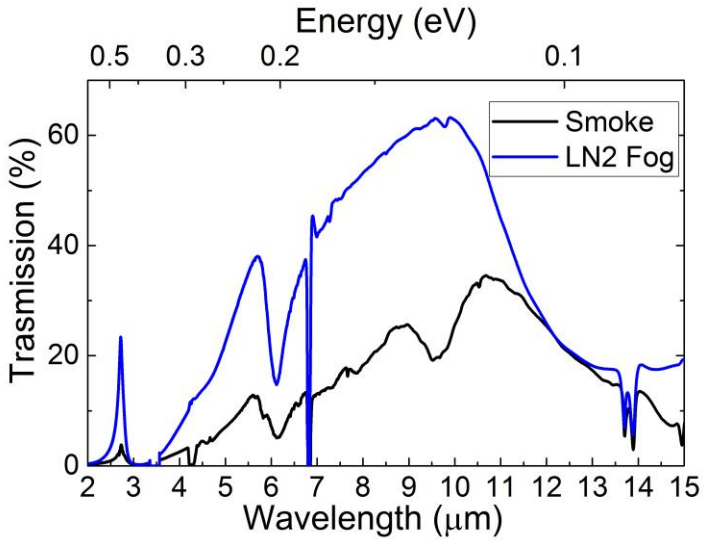

Figure 1.1: Transmission of infrared light through smoke and fog over a path length of approximately 10 cm in the FTIR described in Chapter 6. The transmission peak in the 2.5-3μm range is particularly relevant for this work.

1.2 Group IV epitaxy: Silicon, Germanium, and Tin

1.2.1 Promises

Sn is isoelectronic with Si and Ge, meaning less possibility of cross contamination causing unintentional doping problems. In many ways, adding Sn to an existing semiconductor fab can be seen as a similar direction to adding Ge to Si a few decades ago: a shift in source materials and temperature budgets, but likely no additional tool sets are required.

The promise of adding Sn to Ge is that GeSn alloys have the required near infrared to mid infrared band gaps for device applications. Figure 1.2 shows the bandgap vs. lattice constant for many semiconductors. Adding Sn to Ge is predicted to have a large negative energy bowing parameter, meaning the bandgap extends rapidly

to the Mid-IR with small amounts of Sn. Much more attractive than solely a lower bandgap is the prediction that Ge, a semiconductor with an indirect, L-valley minimum bandgap, will transition to an alloy with a direct, Γ-valley minimum bandgap for these relatively small amounts of Sn, shown by the color change in Figure 1.2. The exact indirect-direct crossover point is the subject of discussion in the research community, but generally expected values range from 6-12% in relaxed GeSn layers [12]–[14].

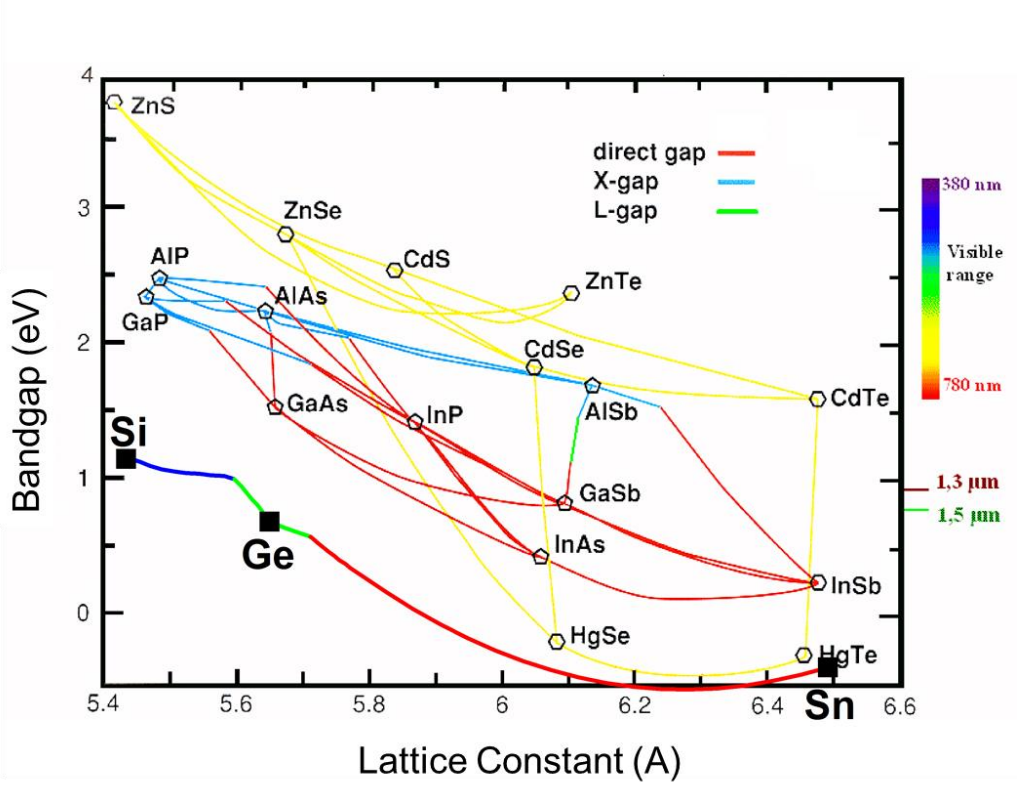

Figure 1.2: The bandgap vs. lattice constant for various semiconducting films. The bandgap models for GeSn are for relaxed films at room temperature, and are from [15] and [16]. This plot of band energy versus composition suggest that the direct band edge (Γ valley) will be the minimum for GeSn films with Sn contents above about 7 %.

1.2.2 Challenges

Sn containing Group IV alloys remain somewhat difficult to work with to this day because of the low solubility of Sn in Si and Ge, as highlighted in Figure 1.3, from ref [17]. The maximum, thermodynamically stable, concentration of Sn in Ge is around 1%. The maximum concentration decreases as the Si content is increased, reaching just 0.1% for pure Si. This limit of Sn content necessitates the use of non-equilibrium epitaxial growth techniques like molecular beam epitaxy (MBE) and chemical vapor deposition (CVD) to create a metastable material. Using these metastable growth techniques GeSn films have been grown with Sn concentrations all the way up to 46% [18].

Meta-stability also presents a problem with high temperature steps in device fabrication including metallization and dopant activation, among others. The maximum "thermal budget", which is the temperature and time combination before the Sn will start to segregate out of the lattice, seems to decrease with increasing Sn content [19], [20].

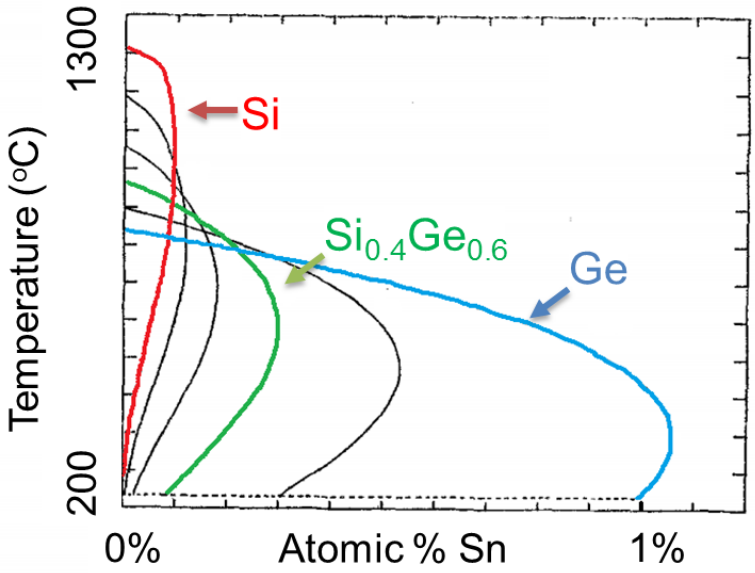

Figure 1.3: A phase diagram showing the solid solubility limit of Sn in alloys of Si and Ge [17]. The curves show the maximum solubility for a given temperature and alloy concentration, ranging from pure Si to pure Ge in steps of 20%.

Two more challenges result from the fact that the Sn lattice constant (Sn = 6.489 Å) is much larger than that of both Ge (Ge = 5.658 Å) and Si (Si = 5.431 Å), as seen in Figure 1.2, which leads to highly strained films for even a small concentration of Sn. The first, seen in Figure 1.4, is the very low predicted critical thickness for GeSn films with enough Sn to theoretically be direct. For Sn concentrations above 10%, the People and Bean model [21] predicts that the critical thickness is less than 50 nm.

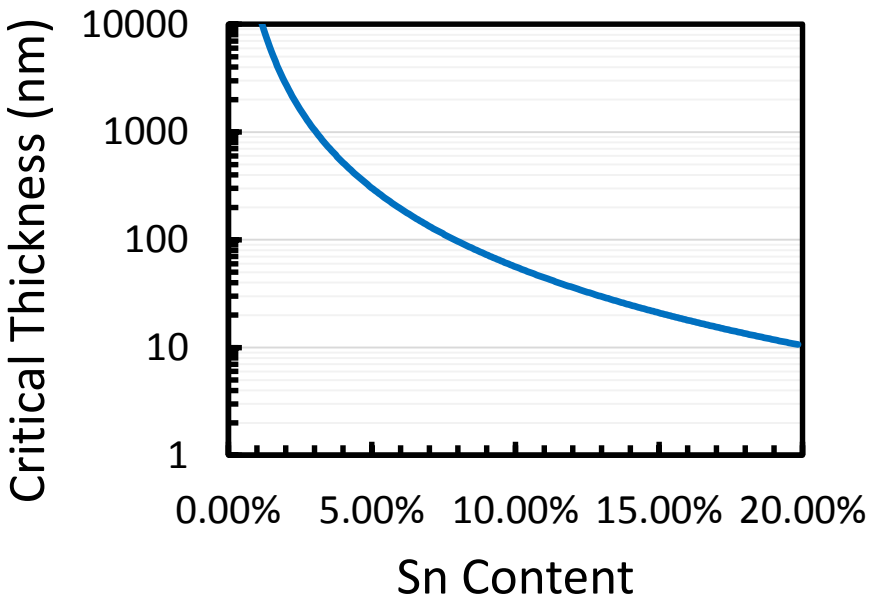

Figure 1.4: The critical thickness of GeSn films grown on Ge substrates according to the People and Bean model [22].

The second, shown in Figures 1.5 and 1.6, is that the bandgap of GeSn will change with the amount of strain on the layer, and due to the large lattice constant difference this has a large effect on the film. Figure 1.5 shows that for relaxed GeSn films, the material becomes direct for Sn concentrations of approximately 7%. As the film is compressively strained, however, the Γ-valley will move higher in energy relative to the L-valley and the material will become progressively less direct. On the other hand, tensile strain does the opposite and makes the film more direct.

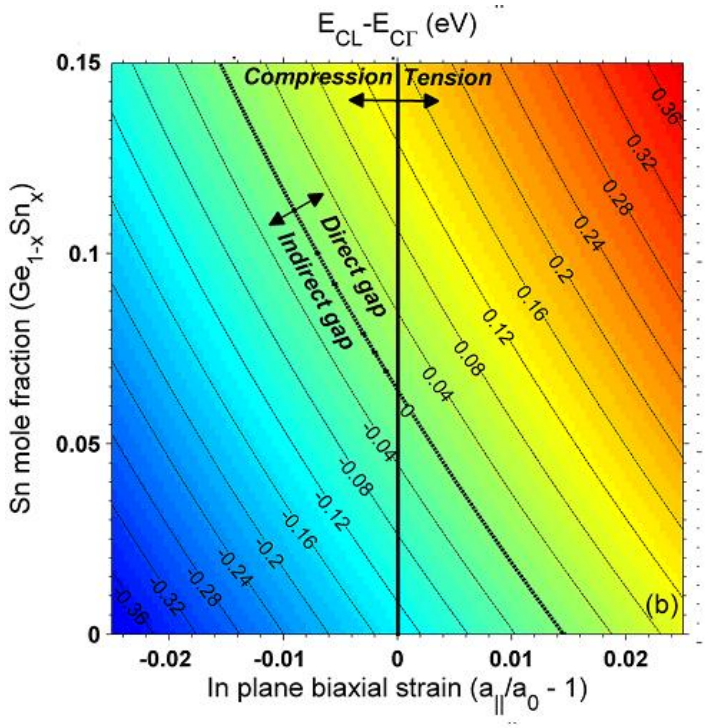

Figure 1.5: The energy difference between the L-valley (E_{CL}) and the Γ-valley ($E_{C\Gamma}$) in GeSn films as a function of in plane biaxial strain from [15]. Positive strain values designate tensile strain while negative strain values are compressive strain. Positive values of $E_{CL} - E_{c\Gamma}$ are direct while negative are indirect.

The primary consequence of the effect of strain on the bandgap is shown in Figure 1.6. The main trend of note is for growth on Ge substrates, or 5.66 Å lattice constant. While the bandgap does decrease as Sn is added, the material does not transition to a direct bandgap material for any amount of Sn. This would indicate that for any application where a direct bandgap material is needed, LEDs or lasers for example, the material cannot have much compressive strain.

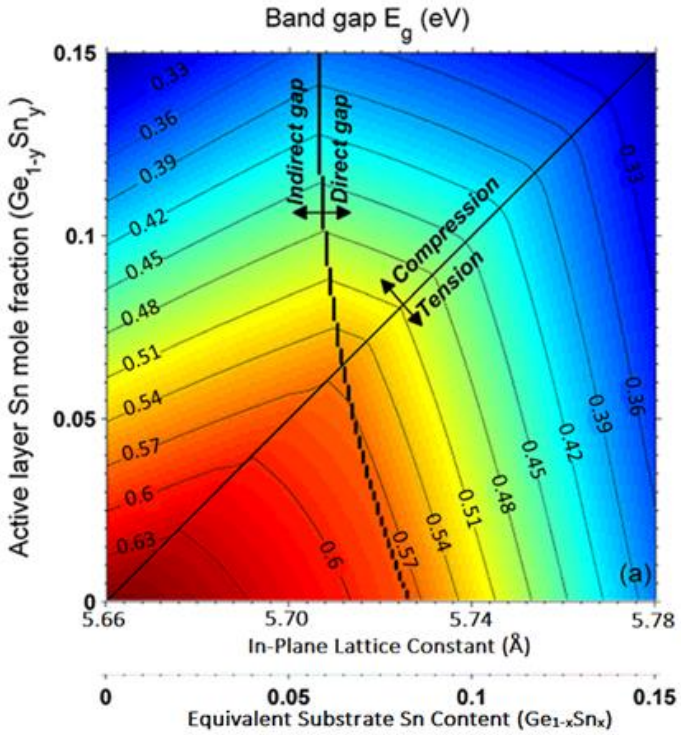

Figure 1.6: The bandgap of GeSn films as a function of in-plane lattice constant, or the equivalent substrate Sn content. Adapted from [15].

1.3 State of the Art

Good progress has been made for GeSn optoelectronic devices with ever higher Sn concentrations. The focus on high Sn has resulted in light emission from an optically pumped laser with a high Sn content of 12.6% [6], the highest Sn content LED with 12% [25], and the highest for detection, a Ge/p-GeSn homojunction with 12% Sn [26].

1.4 Dissertation Summary

This dissertation focuses on the growth, fabrication, and characterization of Group IV semiconductor films for near and mid-infrared detectors and

optoelectronics. The first half of the dissertation deals with the epitaxy of Group IV semiconductors in both CVD and MBE before moving on to the optical and electrical characterization of the resulting films.

Chapter 2 discusses the Oerlikon/ Leybold Sirius Ultra-High Vacuum Chemical Vapor Deposition (UHV-CVD) tool at the University of Delaware. A description of the tool and its baseline operating parameters are noted. Modifications and calibrations to the tool made at the University of Delaware are presented.

In Chapter 3 the morphological stability of SiGe alloy films for heterojunction bipolar transistors was investigated. The study focused on Ge concentrations important to the next generation IBM 9HP BiCMOS process and placed emphasis on maintaining the quality of the alloy film as the Ge concentrations in the devices were increased. An empirical growth rate for 3D surface features as a function of film thickness and growth rate was determined. Growth temperature was found to have the most profound effect on the growth mode.

Chapter 4 builds on the knowledge of Chapter 2 and Chapter 3 by assessing novel precursors tetrasilane, digermane, and tin tetrachloride for low temperature UHV-CVD. Crystalline Si, crystalline SiGe, and amorphous Si films were grown and characterized. The effects of tin tetrachloride co-flow with digermane were measured and assessed for their potential for GeSn film deposition in UHV.

Chapter 5 deals with contributions to the MBE growth of GeSn films. Doping is discussed of both p- and n-type GeSn with Ga and P respectively. The temperature of the substrate during growth is discussed, and its effects on both the resistivity of the film as well as the Sn incorporation. Finally, the process on record (POR) recipe for Ge buffer layer virtual substrates is documented.

Chapter 6 describes the Thermo Fisher Scientific iS50r Fourier transform infrared (FTIR) spectroscopy tool. Instrument setup, calibration, and theory of operation are presented, with an emphasis on semiconductor detector type device characterization.

In Chapter 7 photoconductive devices fabricated from RPCVD grown GeSn devices is presented. Spectral photocurrent of the devices was measured and the bandgap of the material was extracted as a function of Sn concentration and compared with theory. The temperature dependence of the devices is also discussed.

Chapter 8 describes the characterization of GeSn homojunction photodiodes grown by MBE. The electronic current-voltage characteristics are presented and a short circuit current and open circuit voltage are measured under illumination from a broadband source. The optical characteristics including the responsivity and band gap were measured with the FTIR down to cryogenic temperatures.

Finally, in Chapter 9, a summary of this dissertation is given and areas of future work for GeSn research at the University of Delaware are discussed.

The results of the basic and applied research covered in this dissertation have been published in several journals and conference proceedings [27]–[30].

Chapter 2

LOW TEMPERATURE EPITAXY EMPLOYING ULTRA-HIGH VACUUM CHEMICAL VAPOR DEPOSITION

2.1 Introduction

It is advantageous to minimize the amount of high temperature steps during semiconductor device manufacturing for many reasons, including among others: minimizing defects caused by a thermal expansion mismatch between materials, dopant movement and segregation, alloy intermixing, and physical device reshaping. The widely used term 'thermal budget' was coined to represent the idea that a given device has a tolerance to high temperature steps beyond which the device becomes degraded. There are many additional advantages beyond the thermal budget that are specific to group IV epitaxial processes in particular. For example, in Chapter 3, the effect of lowering the growth temperature on the surface morphology of silicon germanium films for BiCMOS is described. Additionally, SiGeSn alloys are metastable materials that require low temperatures to fully incorporate Sn atoms into the atomic lattice.

Chemical vapor deposition, which is the most widely used commercial form of epitaxy, historically required temperatures in excess of 900^{o}C in order to ensure quality material with few defects. In the mid 1980's, Ghidini and Smith [31] produced an influential paper with measurements on the growth rate of SiO_2 from silicon in H_2O and O_2 ambient. Their key result was the observation that, to maintain a silicon surface free of oxidation, the partial pressure of H_2O and O_2 had an Arrhenius relationship

with temperature. For 550^{o}C, the maximum pressure was less than $1*10^{-8}$ torr of H_2O to maintain oxygen free silicon epitaxy, a result which was subsequently used as the basis for designing the first low temperature epitaxy systems including the ultra-high vacuum (UHV) variant by Meyerson which maintains the low impurity concentrations through utilization of ultra-high vacuum environment [32]. These UHV CVD reactors were the first commercial systems capable of silicon epitaxy below 550^{o}C, substantially reducing the thermal budget of epitaxial growth.

The UHV-CVD tool used in this work was donated to the University of Delaware by IBM Microelectronics. The tool is a prototype unit of a design that is still being used in production today for SiGe BiCMOS chips. Over time, various additions and ideal procedures for the use of the tool have been developed for the CVD system in order to fulfill research goals at the University of Delaware. While standard operating procedures were also developed at IBM for the UHV-CVD tool, unfortunately the majority of the knowledge was not able to be directly transferred to Delaware due to practical material and equipment constraints being different for a university research environment vs. an industrial production environment and proprietary information from IBM. The remainder of this chapter describes the tool capabilities and details the changes that were made at the University of Delaware to either the epitaxy process or the CVD tool itself. The chapter concludes with a discussion of epitaxy tools in general and the strengths and weaknesses of UHV-CVD.

2.2 Description of UHV-CVD Tool

The UHV-CVD used in this work is an Oerlikon/ Leybold Sirius CVD-300 model, a derivative of the original design by Meyerson [32]. A schematic of the tool is shown in Figure 2.1.

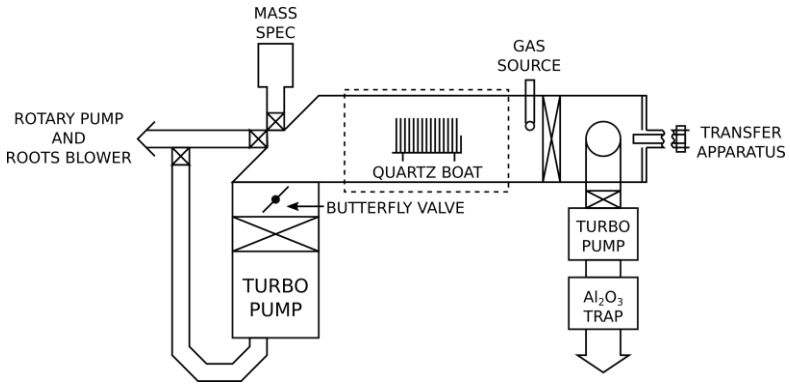

Figure 2.1: A simplified schematic of the UHV-CVD system. Shown is the reaction chamber loaded with a quartz boat full of wafers on the left and the intro chamber on the right. The configuration of the pumping system and butterfly valve are shown in their respective configuration for the main chamber. The source gases are introduced into the growth chamber through one common inlet, near the gate valve that separates the growth from intro chambers. The wafers are transferred between chambers through the gate valve utilizing a magnetically coupled transfer rod.

The reactor chamber is a double walled quartz tube that is continually pumped with a turbo-molecular pump backed by a Roots blower and a rotary vane pump. The temperature in the epitaxy chamber is maintained by a 5-zone PID controller, able to maintain temperatures up to 650^{o}C with <1^{o}C variation across the zones. The temperature is measured by thermocouples on the outside of the chamber, and it is assumed that the wafers are at the same temperature due to the isothermal design although this is not calibrated. Due to its hot-wall design, the UHV-CVD is not able to safely change temperatures faster than 0.5^{o}C/min. The reason for this limitation is because as growths are performed, the quartz walls get coated with layers of material, silicon/germanium etc., which have a different coefficient of thermal expansion than quartz. The difference in expansion coupled with rapid temperature swings can result in cracks, shattering, and implosion.

The tool supports a multi-wafer batch system that is capable of carrying up to twenty-five 200mm diameter wafers with an additional five dummy wafers on either side of the boat for increased temperature uniformity. Multiple iterations of boats have been used at the University of Delaware before closing on the present design. The reasoning for the present design reveals many of the interesting problems inherent with this tool. For example, initially 1-2 different sized dummy wafers were used on either side of the growth wafer, and eventually quarter 125mm wafers were used, both of these methods had problems with uniformity across the wafer. The non-uniformity is thought to be from temperature non-uniformity across the growth wafer. Currently, whole 125mm wafers are used for both dummy and growth wafers. Although this has substantially increased the uniformity across the wafer there still exists a ~1" region around the outside of the wafer with visibly different layer characteristics. From XRD scans, the center 3" diameter area has been found to have little variation in alloy concentration or film growth rate. In addition to whole wafers, four whole dummy wafers are placed on either side of the growth wafer which further increased the uniformity. Increasing from four to five dummy wafers was found to have little increased effect.

In order to reduce impurities introduced by the loading procedure, a separate wafer loading chamber is attached to the growth chamber, separated by a gate valve that is open only during wafer transfer between chambers. The load chamber is pumped by an independent turbo-molecular/ rotary vane pump combination as shown in Figure 2.1. For vacuum analysis the reactor chamber is equipped with a capacitance manometer gauge for vacuum measurement in the range 10^{-4} to 10^{1} torr, an ion gauge for vacuum in the range 10^{-9} to 10^{-3} torr, and a quadrupole mass spectrometer residual

gas analyzer (RGA). Typical base pressures of this CVD system are on the order of 10^{-9} torr (10^{-7} Pa) at growth temperatures of 550°C. Typical background RGA readings at growth temperatures can be seen in Table 2.1. As can be seen from the RGA measurements, the overwhelming majority of gas present is hydrogen, which is a result of the turbo-molecular pump being inefficient at pumping hydrogen compared to other gasses. The high presence of hydrogen does not have much effect, however, as most precursors involved in CVD desorb hydrogen already and it has not been found to have an adverse effect on epitaxial growth, and in fact can have some beneficial attributes which will be discussed in further detail in Chapter 3 and 3.1.

Table 2.1: Typical RGA readings for the UHVCVD at 550°C

Mass	Species	RGA current (A)	N2 Equivalent (torr)
2	H_2	$2*10^{-11}$	$5*10^{-8}$
18	H_2O	$4*10^{-14}$	$2*10^{-10}$
28	N_2, CO	$3*10^{-13}$	$2*10^{-9}$
32	O_2	$1*10^{-14}$	$1*10^{-10}$
44	CO_2	$1*10^{-14}$	$1*10^{-10}$

Due to the ultra-high vacuum nature of the UHV-CVD deposition technique, complications due to gas flow patterns are not important. The mean free path of the molecules is on the order of 10's of centimeters and the gas molecules are assumed to be ballistic over the dimensions of the reactor tube. In addition, the gas phase reactions between gas particles are assumed to be unlikely, which is validated by the absence of particulate formation in post epitaxy analysis by atomic force microscopy. The growth rates in UHV-CVD are typically on the order of nm/min, which is both an advantage

and a disadvantage as will be discussed in further detail at the end of the chapter in section Figure 2.4.

2.3 Modifications and Calibrations at the University of Delaware

2.3.1 Tool bake out procedure

In order to reduce contamination from H_2O, O_2, and other molecules, the CVD chamber is heated to temperatures above normal growth temperatures. The objective is to use heat to liberate any molecules on the walls of the chamber which would then get pumped out. Once the chamber is returned to a lower temperature, the background pressure will be much lower. A bake out procedure was developed specially for the UHV-CVD machine based on the experiment explored below. The bake out procedure is performed anytime the tool has lost vacuum or regularly after a certain period of time, at least every 3 months, though more frequent if the background pressure is above typical levels. The background pressure at 550^{o}C after bake out is in the low 10^{-9} torr range.

Figure 2.2 shows the bake out recipe that was standard operating procedure before 2013. The tube temperature is raised, slowly, with 30 min halts every 50^{o}C until the tube temperature reaches 550^{o}C, where the temperature was then held constant overnight. The next morning the RGA and turbo pump heater jackets were turned on and the temperature was set to 650^{o}C. It is important at this point to turn off the RGA to prevent overheating. Once the CVD tube reached 650^{o}C, the temperature was held for approximately two days and the tube pressure was recorded over time.

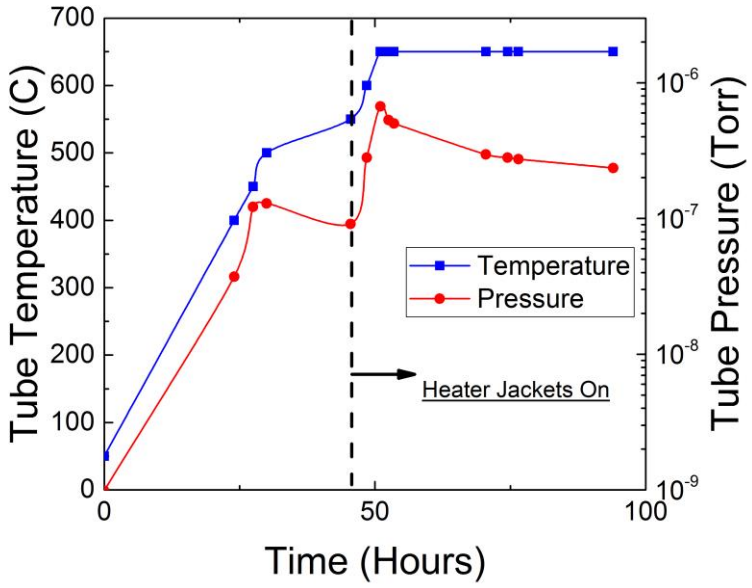

Figure 2.2: A plot of the tube temperature and pressure during a bake out. A dashed line at 45 hours indicates when the tube heater jackets were switched on and the RGA was switched off. The final tube temperature was 650ºC and the final pressure was $2.3*10^{-7}$ torr.

In order to model the bake out progress, the pressure vs. time at bake out of the tube at 650ºC was recorded as shown in Figure 2.3. The time of these data points was adjusted by a constant offset, T0, and fit to a power function as it provided the best fit. The offset time T0 was chosen by finding the value that maximized the R^2 value of the power law fitting function. The 1.5 hrs for T0 gave the highest R^2 value of 0.9995, and thus was the best fit. It can be conjectured, then, that all of the bake-out steps prior to when the CVD tube reached 650 ºC subtracted just 1.5 hrs off of the final bake-out time. The conclusion is that the residual gas evacuation of the first 50 hours of bake-out time would have been accomplished in 1.5hrs at 650 ºC. The new standard bake out procedure is to raise the temperature to 650 ºC in one step (still raising the temp by

only 0.5 ^{o}C/min to minimize the chance of a tube crack) to reduce the time of the bakeout.

When the tube pressure reached $2.3*10^{-7}$ torr the bake out is finished, which takes around 50 hours from when the tube reaches 650 ^{o}C. Extrapolating to longer times, it would take 6 more days of bake-out to reach $1.5*10^{-7}$ torr and 75 more days of bake-out to reach $7.5*10^{-8}$ torr. The pressure of $2.3*10^{-7}$ torr was not decided randomly; it is a target pressure reached for a bake out in Sirius-UHVCVD tools in commercial use. After the bake out is finished, the tube temperature is lowered to 550 ^{o}C and the heater jackets are turned off. The next step in the process is coating the tube with silicon to bury any remaining defects on the quartz walls. Usually this coating step consists of 2 hours at 550 ^{o}C with silane, or in the case of our tool at the University of Delaware Tetrasilane, flow, resulting in >150 nm of Si.

In conclusion, the standard bake out procedure is to raise the tube temperature to the maximum value (650 ^{o}C) in one step with no pauses. The heater jackets should be turned on when the tube is at maximum temperature. The bake out is finished at a final pressure of $2.3*10^{-7}$ torr, at which point the tube temperature should be lowered to 550 ^{o}C and silane flowed for 2 hrs to coat the tube.

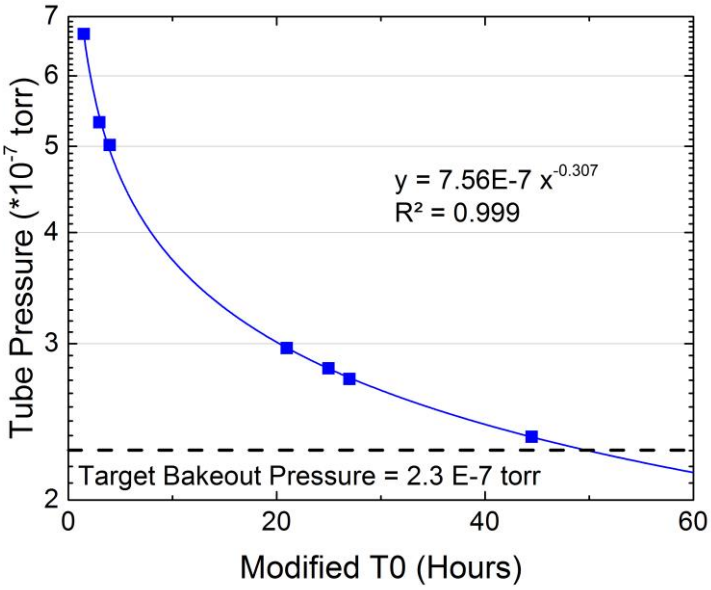

Figure 2.3: Tube pressure vs. bake out time at 650 ^{o}C. The starting time of the pressure decay dependence, or T0, has been modified to maximize the R^2 value of the power function fit shown. The modified T0 value is 1.5 hrs. A dashed line indicates the target bake out pressure.

2.3.2 Utilizing a vapor pressure source for UHV-CVD precursors

Two precursor sources that are installed on the system, tetrasilane and stannic chloride, are both liquids at standard conditions. Liquid precursors present an interesting challenge as to their delivery to the CVD reaction chamber. The two avenues for delivery to the CVD system that are typically used are a bubbler system with a carrier gas and a vapor/ evaporation source.

Previous work on the higher order silane, neo-pentasilane, by Keith Chung at Princeton [33] utilized a bubbler method that bubbled H_2 gas through the pentasilane and relied on the neo-pentasilane vapor saturating the H_2 gas. The problems that were encountered included unsure amounts of saturation in the carrier gas, changing

saturation during a single run, and micro-droplets of neo-pentasilane traveling in the carrier gas clogging the mass flow controllers.

In this work, an evaporation/ vapor source was chosen that relies on exposing the liquid precursor to the high vacuum of the CVD system and essentially causing the precursor to boil off. The vapor source method can be used because the vapor pressures at 20 ^{o}C of tetrasilane and stannic chloride are 27 torr and 18 torr respectively, much higher than the CVD operating pressure which is on the order of 10^{-4} to 10^{-3} torr. The vapor pressure will increase with temperature for tetrasilane and other silanes as shown in Figure 2.4, providing a method of increasing the maximum flow rate by heating the liquid source. Heating was not generally used however, as the flow rate from the sources at room temperature was found to be adequate for the low flow rates required in UHV-CVD.

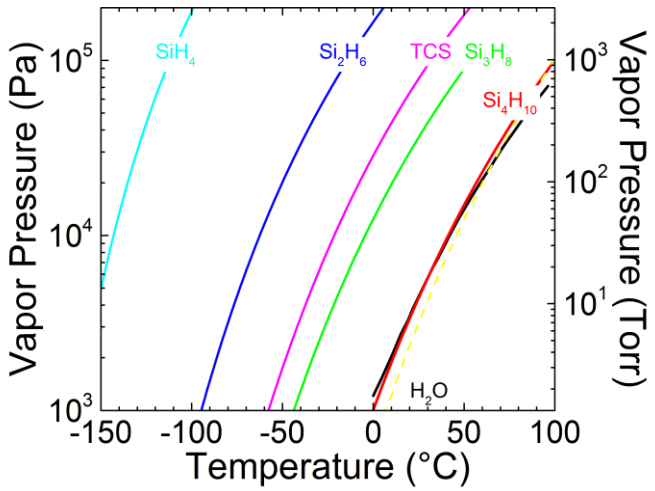

Figure 2.4: The vapor pressure of various silanes [34], [35]. The vapor pressure of tetrasilane at 20°C is 27 torr and increases roughly exponentially with temperature. The next lower order silane precursor is trisilane, which is a gas at room temperature and has a vapor pressure of 95.5 torr. The vapor pressure of water is shown for comparison.

A few problems presented themselves in the use of tetrasilane as a vapor source precursor. To begin with, the maximum line pressure when using tetrasilane is 27 torr, which is much lower than can be read on typical gas line pressure systems so capacitance manometers were installed in the gas lines at the regulator and in the CVD gas box manifold. Secondly, it was found to be important to remove particulate filters from the gas line in order to prevent unnecessary pressure drops from the cylinder to the CVD.

The largest problem that occurred in the operation of the tetrasilane vapor source was due to condensation of the vapor in the gas line. When the line is actively being used, the precursor evaporates out of the cylinder, cooling the remaining liquid. Thus, during operation, the cylinder is the coolest point in the line and any re-

condensation will occur there. After operation is ceased the bottle will reach room temperature and might not be the coolest place in the line any longer. Condensation of the precursor into liquid form is possible. The resulting situation can be quite catastrophic: tetrasilane vapor leaked through the MFC and condensed above the last pneumatic valve before the CVD chamber. When the last pneumatic valve opened all the condensed tetrasilane was vented into the chamber. As the liquid is much denser than the gas this was enough to raise the pressure in the CVD chamber to >0.1 torr. Gas phase reactions rapidly occurred and the entire CVD chamber was coated in a fine silicon powder. A photo of the aftermath is shown in Figure 2.5.

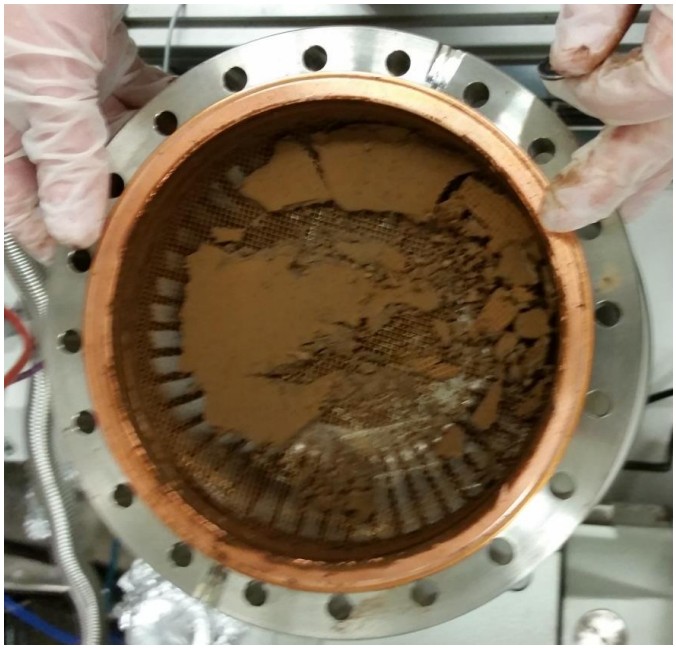

Figure 2.5: A photo of silicon dust on top of the CVD chamber turbo-molecular pump caused by tetrasilane gas phase reactions. The mesh grating above the turbo miraculously stopped any dust from entering the pump itself.

The solution to the problem of condensation was to heat the gas lines. For the tetrasilane line, four different zones were chosen, one at the MFC, one for the overhead gas lines, one for the gas lines inside the gas cabinet, and one for the tetrasilane cylinder. The temperature is measured with thermocouples and increases towards the CVD tool in order to insure that any condensation that occurs, happens away from the tool itself. Temperature uniformity is very important, and so the gas line and the heaters were wrapped with insulation. The $SnCl_4$ line heater design was simplified, in that only one temperature zone was used throughout the entire gas line, and the cylinder itself was left unheated.

Both tetrasilane and tin chloride (the filling of which is covered in the next section) have a gas 'pad', or an overpressure of inert gas in the source cylinder, as supplied by the vendor. The tetrasilane comes with a 5 psi He pad and the tin chloride has a N_2 pad from being filled in a N_2 glove box as described later. The gas pad must be drawn off through the CVD tool before growth can commence with the liquid vapor. Figures 2.6 and 2.7 show pressures and flow rates during the extraction of the He pad on the tetrasilane. This data was taken using the CVD RGA, the MFC, and the Cap. Man. installed on the tetrasilane line regulator.

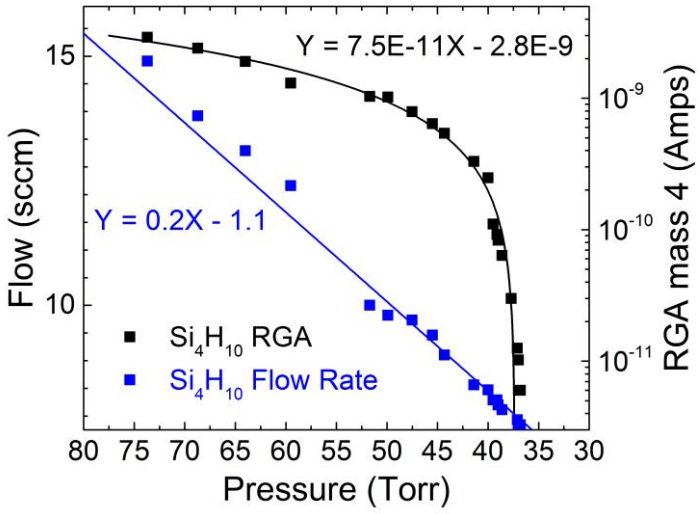

Figure 2.6: He signal on CVD RGA and measured flow rate as a function of the tetrasilane line pressure as the He pad is being removed. The data points have been fit to straight lines with fitting functions shown in respective colors. The RGA fit extrapolates to zero for a line pressure of 37.3 Torr and a corresponding flow rate of 7.5 sccm.

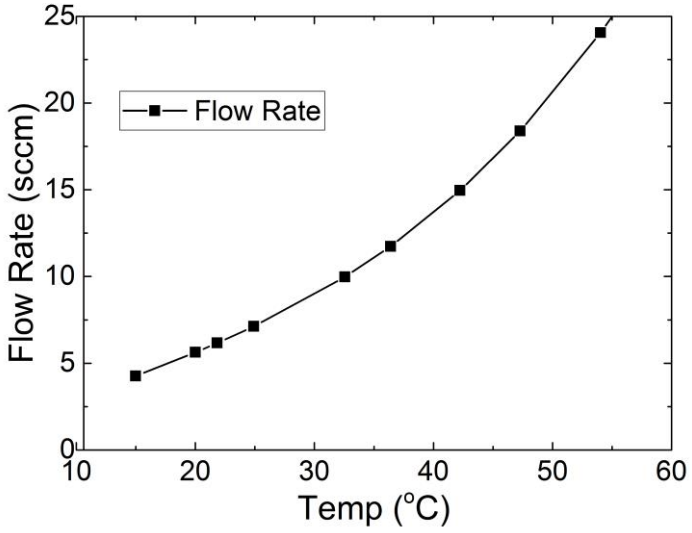

Figure 2.7: Combining the tetrasilane flow rate and the tetrasilane vapor pressure, Figure 2.4, yields this theoretical plot of maximum tetrasilane flow rate versus bottle temperature. The calculation is theoretical, based on what flow rates could be achieved by heating the tetrasilane bottle and was never tested as it wasn't deemed necessary to achieve sufficient flow rates.

Tin chloride, presented in Section 2.3.3, presented a scenario similar to the tetrasilane line in that both had an inert gas overpressure. There were two key differences between the two sources: the inert gas on the tin chloride was N_2, which exists in the CVD naturally and so the tin chloride line is harder to trace on the RGA as the N_2 gets removed, and the tin chloride MFC was originally a He calibrated MFC with 50 sccm maximum flow rate. The MFC value was scaled to silicon tetrachloride and a max flow rate of 9.6 sccm $SiCl_4$ was found. The MFC was replaced with a 200 sccm N_2 calibrated regulator to achieve greater flow rates. The MFC replacement was after the N_2 was drawn off the tin line. Figure 2.8 shows the extraction of the N_2 pad on the tin chloride as recorded on the CVD RGA, the MFC, and the Cap. Man. installed on the tin chloride line regulator.

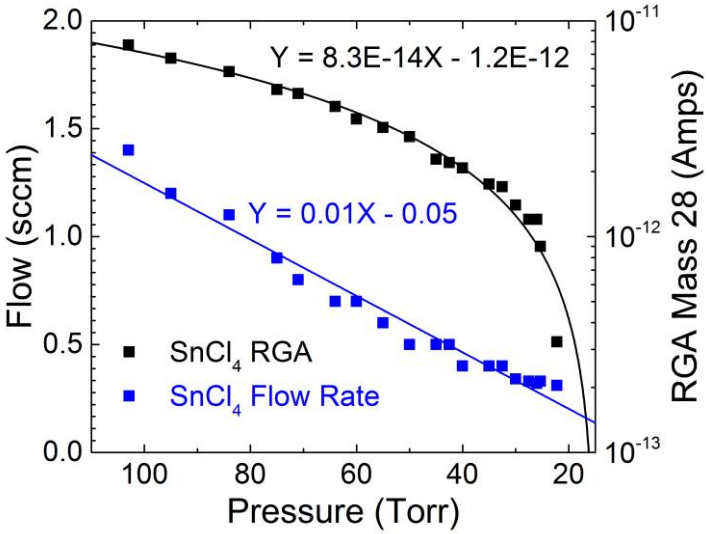

Figure 2.8: N_2 signal on CVD RGA and the flow rate as a function of the tin chloride line pressure as the N_2 pad is being removed. The data points have been fit to straight lines with fitting functions shown in respective colors. The N_2 fit extrapolates to zero for a line pressure of 22.4 Torr and a flow rate of 0.3 sccm.

2.3.3 Stannic chloride as a precursor

Preparation work was done in order to look at growing Sn containing alloys in the UHV-CVD. The initial challenge of this work is to find a suitable Sn containing precursor. The challenges include precursor shelf life, possibility of contamination, and compatibility of the chemical reaction rates. Previous Sn precursors that have been used include Tin-Deuteride (SnD_4) [36] and Tin-Chloride ($SnCl_4$) [37], which are both single Sn atoms bonded tetrahedrally to Deuterium atoms or Chlorine atoms respectively. Tin- Hydride (SnH_4) is not a possible Sn precursor due to its extremely short shelf life of approximately one week. In addition, SnD_4 was initially planned for the tin precursor at the University at Delaware, however this precursor also presents shelf stability problems. Replacing the hydrogen with heavier deuterium atoms in tin-

hydride stabilizes the precursor to a couple of weeks, which is still unsuitably short. Chilling the gas bottle with CO_2 "dry" ice, however, leads to an improved shelf life of up to 6 months, at which the precursor will break down in a self-catalyzing fashion.

Tin-Chloride has no shelf stability problems and is a commercially available precursor with other uses in polymer chemistry so is easily purchasable. The primary challenge with the precursor however is due to its chlorine containing nature providing unique challenges as it will etch stainless steel. The incompatibility is due to a reaction pathway with water:

$$SnCl_4 + 2H_2O = 4HCl + Sn + O_2 \quad (2.1)$$

The HCl, will dissolve in water to create hydrochloric acid which can attack stainless steel. Thus, the elimination of moisture in the system it of tantamount concern as it relieves any adverse effects from the precursor source. The moisture must be eliminated not only from the gas line, but also the cylinder itself. In order to ensure no moisture in the stainless steel bubbler, an N_2 glove box must be used while refilling the $SnCl_4$ precursor. The following procedure was developed in order to fulfill the above requirements. The cylinder used for the $SnCl_4$ was sourced from Strem Chemical, with 150 mL maximum volume, and was 316L stainless steel.

1. Verify/Clean $SnCl_4$ bubbler
    i. Visually inspect $SnCl_4$ bubbler for signs of corrosion.
    ii. Attach $SnCl_4$ bottle, using the CGA 350 connection, to the $SnCl_4$ gas line of the ultra-high vacuum chemical vapor deposition (UHV-CVD) tool in 105 DuPont.
    iii. Perform twenty pump/purge cycles with purge N_2 and the venturi pump in the gas cabinet in accordance with general bottle attachment procedures.
    iv. Begin pump down of the $SnCl_4$ gas line with CVD tool pumps.

v. Pump down is complete when the residual gas analyzer (RGA) on the CVD reads the same signal with the gas line open or closed to the system.

vi. RGA signals of atmosphere include: H_2O (mass 18), O_2 (mass 32), and CO_2 (mass 44)

vii. If RGA signals of atmosphere persist, check for leaks on $SnCl_4$ bottle utilizing He leak checking with the RGA (mass 4).

viii. Replace any gaskets that are faulty.

ix. If line leaks persist or $SnCl_4$ bubbler is found to be at fault, do not continue with installation and replace the faulty equipment.

x. If no leaks are found and the $SnCl_4$ bubbler is found to be leak free, purge $SnCl_4$ line with N_2 using the gas manifold in the cabinet and close the $SnCl_4$ bubbler needle valve.

xi. Evacuate $SnCl_4$ line with CVD pump.

xii. Verify that there are no leaks across $SnCl_4$ needle valve by measuring RGA signal of N_2 (mass 28) with the $SnCl_4$ line open and shut. If there is a leak, there will be additional N_2 signal from the N_2 filled cylinder.

xiii. Open up needle valve on SnCl4 bottle and fully evacuate the bubbler.

xiv. Heat the bubbler and the gas line to 45 ^oC to ensure moisture removal.

xv. Seal needle valve on bubbler.

xvi. Close off gas line valve in the gas cabinet above the cylinder

xvii. Disconnect $SnCl_4$ bubbler at the CGA 350 connection.

2. Fill $SnCl_4$

i. Only proceed when the previous steps “1. verify/clean $SnCl_4$ bubbler” are complete.

ii. Place $SnCl_4$ bubbler, $SnCl_4$ chemical liquid, glass pipette, a replacement stainless steel VCR gasket, and a ¾" wrench in the N_2 glove box feed through compartment.

iii. Pump/ Purge feed through compartment with N_2 three times to ensure inert atmosphere with no moisture contamination.

iv. Use N_2 glove-box gloves to move items into an easily accessible position.

v. Use ¾" wrench to open $SnCl_4$ bubbler at the VCR valve closest to the bubbler body, detaching the needle valve assembly.

vi. Remove old VCR gasket from the needle valve assembly.

vii. Attach new VCR gasket (316 SS) to the needle valve assembly and place to the side.

viii. Open $SnCl_4$ chemical container.

ix. Use glass pipette to move $SnCl_4$ from its glass bottle to the $SnCl_4$ bubbler.

x. Once complete, set aside glass pipette and reseal the $SnCl_4$ chemical glass bottle.

xi. Use the wrench to reattach the $SnCl_4$ bubbler needle valve assembly.

xii. Place materials in N_2 glove-box feed through doorway and proceed with the pump/purge cycle in order to move all materials from the glove-box to the room.

xiii. Triple rinse and dispose of the empty $SnCl_4$ glass bottle and pipette in corrosive chemical waste container.

xiv. Proceed with attaching $SnCl_4$ to CVD system.

2.3.4 Gas flow and pressure calibration

Many of the precursor gasses used in this work are novel and, as a result, not many of their properties are known. One glaring example is that in order to properly calibrate the mass flow controllers for a particular gas you need not only the density of the gas but also the specific heat capacity of the gas, as they measure mass flow by its temperature changes. In order to properly assess the amount of precursor in the chamber, the pressure of the individual gasses vs. flow rates was used. Pressure calibration becomes exceedingly important in the use of mass flow controllers (MFCs) as they drift with time much more than the pressure measurement instruments, and need to be re-zeroed up to a few times per year.

Many companies recommend a hot cathode ion gauge (HCG) for the region of pressure that the CVD is operated at ($<10^{-3}$ torr). The problem with a HCG is that the precursors used in the CVD are inclined to decompose at high temperatures, resulting in a significantly shorter gauge lifetime due to deposition on the gauge itself. Although there is an interlock on the CVD tool software that turns off the ion gauge when gas is flowing, it is still possible to operate the controller manually by turning on the gauge on the CVD control panel.

The problem with using a hot cathode gauge is the same as the problem with the mass flow controller, which is that every gas has an individual gas correction factor (GCF) that depends on the ionization cross section. The ionization cross section is also an unknown for the novel precursors used in this work. Fortunately, there is not only a hot cathode gauge but also a capacitance manometer pressure gauge (MKS brand) on the CVD. The capacitance manometer is used during epitaxy for butterfly valve control and, most importantly, is gas independent. The MKS capacitance

manometer's lower pressure bound is 10^{-4} torr, which is low enough to roughly measure sufficiently high gas flows.

The formula for using the gas correction factor is simple:

$$Real\ Pressure\ = \frac{Ion\ Gauge\ Reading}{Gas\ Correction\ Factor} \tag{2.2}$$

Using the gas correction factors for the hot cathode gauge for hydrogen (from literature = 0.46) resulted in a very close reading to the capacitance manometer gauge under a wide range of high hydrogen flow. For tetrasilane and digermane, the pressure that the MKS capacitance manometer gauge reads is close to the bottom of its range, but can still be measured. At 550 ^{o}C, the gas correction factor for tetrasilane was calculated using the above procedure to be 6.4 while the gas correction factor of digermane 10% in hydrogen, was calculated to be 0.3. If the GCF is corrected for each gas, then both the ion gauge and the capacitance manometer gauges will read the same value over a wide range of pressures and flow rates for different gasses. The MKS measured pressures over different gas flow ranges is shown in Figure 2.9.

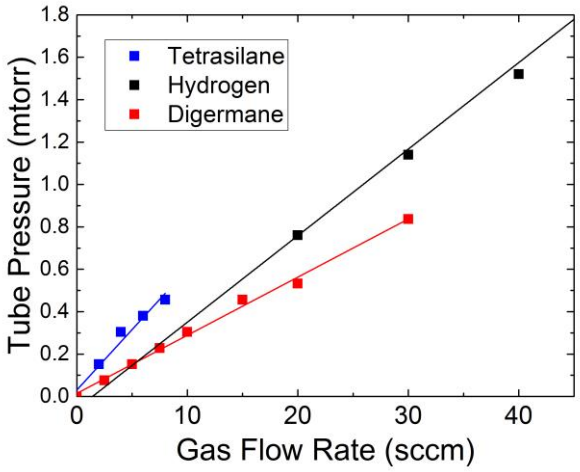

Figure 2.9: Precursor gas flow rates vs. CVD tube pressure measured with an MKS capacitance manometer pressure gauge at a reactor temperature of 550 ^{o}C.

2.3.5 Wafer cleaning and HF passivation

When left in ambient conditions, both silicon and germanium wafers will oxidize with what is referred to as a 'native oxide' layer. In addition to the native oxide, chemical contamination on the surface of the wafer from both organic (including photoresist) and metallic compounds can accumulate as well. For quality epitaxy to proceed, the wafer must be free of oxide and contamination.

There are many techniques to cleaning wafers. The wafer cleaning procedure developed at the University of Delaware for epitaxy on silicon wafers is a modified version of a chemical solution exposure developed at the Radio Corporation of America (called the RCA clean, or standard clean/ SC) [38]. The RCA clean traditionally involves three different chemical baths, with the third being a strip of the native oxide. In this work, the modification to the RCA method is an insertion of an additional oxide strip between the first two chemical baths. Between each chemical

bath, the wafer is placed in deionized water to remove and dilute any previous chemicals that could remain.

Wafers with heavy organic contamination, such as those previously patterned by photoresist, were subjected to an additional cleaning step prior to the RCA clean: a 'Piranha' acid etching step that was a 2:1 mixture of sulfuric acid (H_2SO_4) and hydrogen peroxide (H_2O_2). The Piranha clean aggressively etches organic compounds while leaving the silicon surface unaffected. For example, a ten-minute exposure to this etch will completely dissolve a 5um SU-8 photoresist layer.

For wafers that were not patterned with photoresist and that arrive from the manufacturer "epi-ready", the RCA clean was still found to be necessary for achieving quality epitaxy. The first chemical solution in the RCA sequence, colloquially called RCA-1, is a (1:1:5) mixture of ammonium hydroxide (NH_4OH), hydrogen peroxide (H_2O_2), and deionized water (DI-H_2O) respectively. RCA-1 is for removing particulates and organics on the semiconductor surface. Typically, this clean lasts for 10 minutes on a hot plate heated to 75 ^oC. The next step is traditionally RCA-2, but our modified recipe is to introduce an additional oxide strip between RCA-1 and RCA-2. The middle oxide strip uses a (1:50) mixture of hydrofluoric acid (HF) and deionized water (DI-H_2O) respectively, for 30 seconds. The third step, RCA-2, is a (1:1:6) mixture of hydrochloric acid (HCl), hydrogen peroxide (H_2O_2), and deionized water (DI-H_2O) for 10 minutes. RCA-2 effectively removes metallic and alkaline contaminants and leaves the silicon surface oxidized due to the addition of hydrogen peroxide.

The last, or fourth, step in the RCA procedure is another HF dip to remove the oxide formed in RCA-2, and to leave the surface hydrogen terminated. The last HF

step is the most critical step for epitaxy and, as it is the last solution that the wafer is exposed to before entering the epitaxial tool, has the largest effect on the resulting film/substrate interface contamination.

Many studies have been done on the effect of interfacial contamination on the quality of epitaxial grown wafers, and most have found that even after oxide removal, there exists a sub-monolayer of oxide on the semiconductor surface that can have profound effects on epitaxy and resulting devices. For a great example, the paper by Bedell et al. [39] measured the effect of interfacial oxide contamination on the resulting defect counts of epitaxial growth. This work reported the presence of exponentially more crystalline defects with an increase in interfacial oxide contamination, which was measured by Secondary Ion Mass Spectroscopy (SIMS). For example, a sample with an interface contamination of 10^{13} O/cm^2 had a measured defect count of 10^3 defects/cm^2, while a sample with an interface contamination of 10^{14} O/cm^2 had a measured defect count 3 orders of magnitude higher at 10^6 defects/cm^2.

A good description of silicon wafer oxide stripping methods that reports two procedures for removing the oxide from silicon: an ex-situ HF acid dip and an in-situ high temperature/low pressure bake in hydrogen ambient, is the paper by Brabant [40]. Without a doubt, an in-situ high temperature hydrogen bake is the best form of oxide removal, and results in the lowest residual oxide contamination at the growth interface ($<10^{13}$ O/cm^2). Unfortunately this high temperature bake out which requires minimum temperatures of 700 ^{o}C is not always possible due to CVD process and system limitations [41]. For a given device structure, these high temperatures result in a very high thermal load, shrinking or exceeding the thermal budget considerably, and are not

always possible. In addition, some epitaxy tools, for example the UHV-CVD used in this work, are not capable of such high temperature bake-outs. The UHV-CVD used in this work has a hard temperature limit of 650 ^{o}C and a safe temperature ramp-rate of 0.5 ^{o}C/min, completely ruling out the application of an in-situ high temperature process in a reasonable amount of time.

The method used in this work for removing oxide from silicon is the ex-situ HF acid dip. The last-HF dip results in the stripping of bonded oxygen atoms from the silicon surface and replacing them with hydrogen atoms, resulting in a mono-layer of hydrogen on the silicon surface that inhibits oxygen and other contaminants from reattaching. Typical residual O doses measured by SIMS after an ex-situ HF dip are around 10^{13}-10^{14} O/cm^2. The resulting interface contamination is a function of acid/ water ratios, dip exposure times, dissolved oxygen contents of the acid solution and even the water rinse step after the acid exposure; these variables are explored well in ref [40]. In summary, a successful ex-situ rinse has dilute HF in *de-oxygenated* DI water that ends with a water displacement rinse that slowly dilutes the mixture until the wafer is eventually removed.

At the University of Delaware, a system was designed to perform just such a procedure and was installed in the fume hood in 105 DuPont Hall. The ‘dip tank’ is a 2.5 L Teflon box with a removable lid, with an electronically switched water inlet and drain, as well as a water inlet and an overflow spout that drains into a calcium carbonate container for neutralizing HF acid. The typical last step in this dip tank apparatus is a five-minute dip in a (1:100) mixture of hydrofluoric acid (HF) to deionized water (DI-H_2O), followed by a twenty-minute dilution with DI water

flowing at 1L/min. The pH of the dip tank is shown in Figure 2.10. After the dilution rinse, the wafer is loaded into the CVD intro chamber for evacuation immediately.

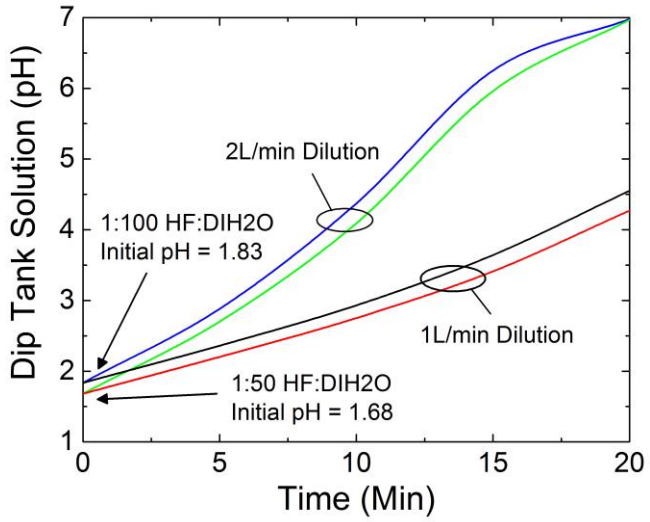

Figure 2.10: Calculated HF dilution as a function of DI-water dilution rate over 20 minutes. Two initial conditions are given, 1:100 HF mix and 1:50 HF mix. The standard operating procedure for last-HF dip for the CVD is five-minutes exposure to 1:100 HF and then a twenty-minute dilution at 1L/min, this corresponds to the dashed black line on the above graph.

Shown in Figure 2.11 is measured SIMS data on a growth of pure Si at 500ºC by UHV CVD. An O-dose of $7.8*10^{13}$ atoms/ cm^2 was measured in this sample, which is a typical O-dose from the HF dip-tank recipe outlined above. Similar O-doses were found for different growth temperatures and different epitaxial layer contents. The O-dose measured is similar to that measured in other reports for SiGe epitaxy [39].

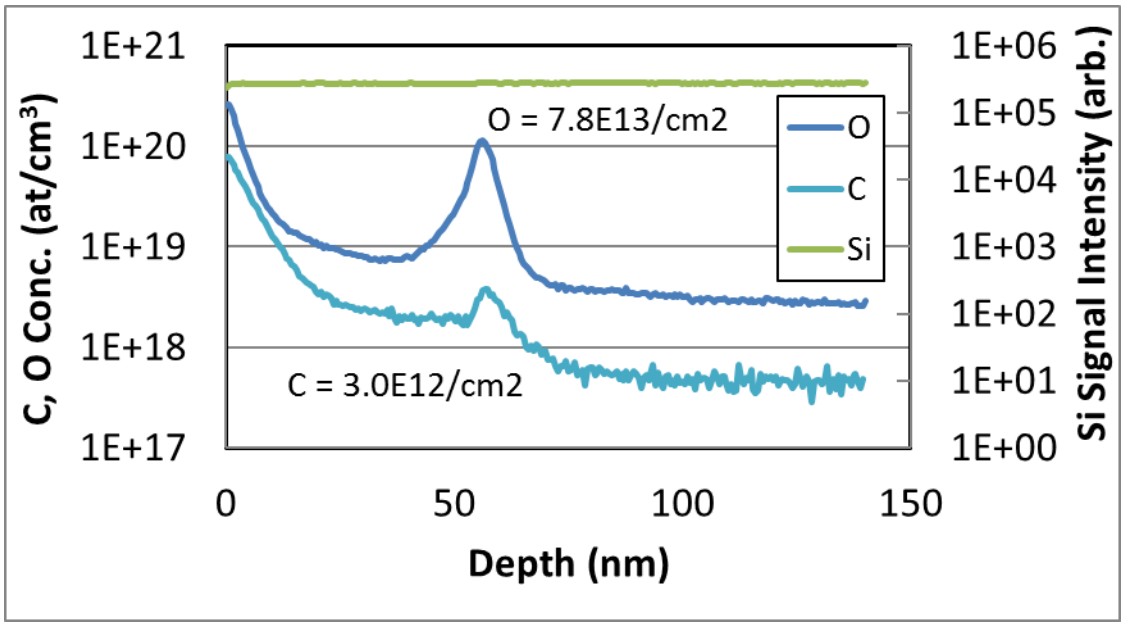

Figure 2.11: SIMS data on SGT104, a sample grown at 500°C with tetrasilane. The interfacial oxygen dose was $7.8*10^{13}$ cm^{-2} and the carbon dose was $3*10^{12}$ cm^{-2}.

2.4 Conclusions: advantages and disadvantages of UHV-CVD

UHV-CVD is an adaptable method that is capable of the epitaxial growth of materials that are important to the next generation of semiconductor devices at commercial production levels. Nonetheless, it is instructive to compare UHV-CVD to its rivals, as it provides many advantages and disadvantages over its two main technological competitors, namely molecular beam epitaxy (MBE) and reduced pressure chemical vapor deposition (RP-CVD). MBE is a well-regarded epitaxial technique that has produced the best quality devices in numerous instances. At its heart, MBE is basically a heated wafer under ultra-high vacuum conditions that has a flux of some source material on its surface. Growth rates for MBE are typically on the order of 1-10 nm/min, not substantially different from UHV-CVD. MBE precursors are often solid sources of the constituent elements of the desired alloys, but often gas

sources are used as well. The advantages of MBE are often a cleaner UHV environment with lower background levels of impurities. Unlike CVD, MBE is not a chemical-reaction driven process and it allows for a finer control of deposition parameters. With MBE, the material flux rate controls both the deposition rate and the material composition and these are separate to a large degree from the substrate temperature. CVD does not have this advantage but for the most part the alloy composition and growth rate unknowns of CVD are easily overcome by calibration of deposition rates and temperatures, see Chapter 3 and 3.1 for examples. CVD presents one other problem with respect to hydrogen coverage on the surface of the material. A hydrogen covered surface is both an advantage and a disadvantage, and both aspects will be discussed in more detail in Chapter 3 and 3.1. While MBE might present a more agile platform, CVD clearly wins in the manufacturability aspect. While the growth rates from the two techniques are within an order of magnitude, CVD is capable of uniform deposition on much larger wafers and multiple wafer batches, while MBE is typically limited to smaller single wafers to preserve uniformity. For example, while the MBE at the University of Delaware deposits on single 3" wafers during growth, the UHV-CVD is capable of deposition on up to twenty-five 8" wafers simultaneously. In most circumstances the higher throughput leads to the use of CVD in most commercial operations.

The difference between UHV-CVD and RP-CVD is subtler. RP-CVD maintains its low H_2O content through use of point-of-use gas chemical purifiers rather than ultra-high vacuum conditions. The pressures in RP-CVD are on the order of 10 torr, and thus gas phase interactions and flow dynamics are more relevant. In order to deal with flow uniformity, RP-CVD tools are single wafer tools. Unlike MBE,

however, the growth rate of RP-CVD tools is often much higher, on the order of 50 nm/min, due to the higher growth pressure and thus higher presence of precursor molecules, allowing higher growth rates. The higher growth rates can be a downside, however, as a faster growth rate inherently means a less precise layer thickness and dopant control. Gas-gas (gas phase) reactions have presented a problem in RP-CVD, especially for highly reactive precursors at higher pressures, which is not a problem in UHV-CVD as the pressure is so low that the mean free path of particles (10s of cm) is larger than the reaction chamber dimensions so that gas phase reactions can be safely ignored.

The biggest advantage that both MBE and RP-CVD have over UHV-CVD (specifically the hot-wall version employed here) is the ability to rapidly change temperatures, which specifically comes into play in a pre-epi bake as discussed in section 2.3.5. Another advantage of rapid temperature change is the ability to grow different films at different temperatures in a single growth. Growing films at lower temperatures becomes especially relevant for metastable and highly strained materials, which often times require optimal growth at different temperatures.

Chapter 3

MORPHOLOGICAL STABILITY OF SILICON-GERMANIUM ALLOYS FOR HETEROJUNCTION BIPOLAR TRANSISTORS

3.1 Introduction

New generations of SiGe technology require higher frequency response to meet demands in the marketplace [42]. Reducing the base transit time of a hetero-junction bipolar transistor (HBT) is an important way to reach ever higher cutoff frequency (Fmax and Ft) goals [43]. Reducing the base transit time in a SiGe HBT can be achieved by either thinning the base or increasing the ΔEg, the total variation of band gap energy across the base [44]. Thinning the base region can have adverse effects due to boron diffusion, thus the other path forward for new technologies would be increasing the peak germanium concentration. One requirement for the active layer in SiGe HBTs is that the SiGe layer be grown pseudomorphic, or strained, on a Si substrate. Two problems exist at higher germanium concentrations due to strain. Relaxation of the layer can occur through misfit dislocations in which the strained layer relaxes due to defects in the crystal lattice [21], [39]. In the absence of misfits, relaxation can still occur through a changing of the surface morphology of the growth, a switching of growth modes from planar to three-dimensional (3D). Non-planar growth has been observed numerous times in SiGe epitaxy [45]–[47] and is well understood for strained alloy growths through the model of Spencer, Voorhees, and Tersoff [48].

From Spencer [48] Equation 5.12, the growth of the surface perturbations, $\hat{h}$, can be written as,

$$\hat{h} = \hat{h}_o Exp\left(\frac{\sigma\bar{h}}{\nu}\right) \tag{3.1}$$

Where $\hat{h}_o$ is the initial amplitude of the perturbation. The σ, $\bar{h}$, and ν variables are non-dimensional variables introduced in the work of Spencer: σ is proportional to growth rate of the most prominent mode, $\bar{h}$ is proportional to the thickness of the film, and ν is proportional to the growth rate of the film. Equation 3.1 expresses the competing mechanisms of strain in the layer and surface free energy expressed by σ, while also capturing the effect of incoming material flux that serves to stabilize the surface by homogeneous material deposition, expressed by ν. As the layer grows thicker, the increasing strain will increase the growth rate of the surface perturbations. Eventually, the stabilizing effect of the homogeneous influx of material will be overcome by the growth of these perturbations, and the change in surface morphology will be evident. The film thickness where the height of the perturbations rises above the background roughness of the growth is called the kinetic critical thickness. The kinetic critical thickness can be expressed in terms of the variables in Equation 3.1, as presented in Spencer Equation 5.14,

$$h_c \propto \frac{\nu}{\sigma} \tag{3.2}$$

The kinetic critical thickness is different from, but has similarities to, the classical critical thickness for misfit dislocation. The idea of a kinetic critical thickness was introduced by [49] and continued in work by [46] and Spencer et. al. in [48]. While the kinetic critical thickness has been experimentally measured with respect to alloy composition [46], little experimental work has been done with respect to the new theoretical models to characterize the growth rate of the perturbations with respect to

growth parameters, specifically on how the growth temperature and the growth rate of the film affect the kinetic critical thickness, which we will do here.

3.2 UHV-CVD for the growth of SiGe HBTs

SiGe samples in this study were grown in an Oerlikon/Leybold Sirius 600 hot-wall ultra-high vacuum chemical vapor deposition (UHV-CVD) tool installed in the IC fabrication line at IBM in Burlington, VT and described in more detail in Chapter 2. Wafers are loaded thirty-five at a time, and for this study the center wafer was chosen for analysis. The temperature across the growth chamber is monitored with thermocouples, and regularly calibrated so that the silicon growth rate is equalized across the boat. Due to the nature of construction of a hot-walled chamber, deposition occurs on the quartz chamber walls throughout the growth, and this buildup is not cleaned in-situ for these machines. Rapid temperature changes would cause problems as the thermal expansion mismatch between the quartz and the deposited material can lead to cracking of the quartz wall and loss of vacuum. Therefore, the entire growth must be done at the same temperature.

The CVD tool is equipped with silane and germane for alloy growth as well as other gasses for doping. The chamber pressure during growths is not controlled automatically in the tool; rather the different gas flows are controlled by mass flow controllers, and have different partial pressures depending on the turbo-pump speed. Gas constituents are monitored by an in-situ residual gas analyzer (RGA). Prior to these experiments, the growth rates and germanium compositions were calibrated by x-ray diffraction (XRD) using omega-2theta scans and Bede RADS simulation software. Germanium concentrations were corroborated with Rutherford back scattering (RBS) measurements, while layer thicknesses and doping concentrations

were corroborated with a combination of secondary-ion mass spectroscopy (SIMS) and stylus profilometry.

Figure 3.1 is an Arrhenius plot of the growth rates for different SiGe compositions at different temperatures. The silane flow rates for all films were held constant, and the germane flows were varied between samples to change alloy composition. For silicon layers, as well as lower composition silicon-germanium alloys, the growth rate is exponentially dependent on temperature with an activation energy of 2.1eV, similar to what is seen elsewhere for temperature dependent, reaction rate limited growth of silicon [50]. As the germanium composition increases, the growth rate transitions from reaction-rate to mass flow limited growth in this temperature range of Figure 3.1, in which the growth rate is negligibly dependent on temperature. A transition between these two growth regions can be seen for compositions just above 10% Ge. The growths of all layers in this work were targeted at 32% Ge, and were done in the mass transport limited growth regime. Thus the growth rate for a given germanium composition was not dependent on temperature, but only on total precursor flow rates.

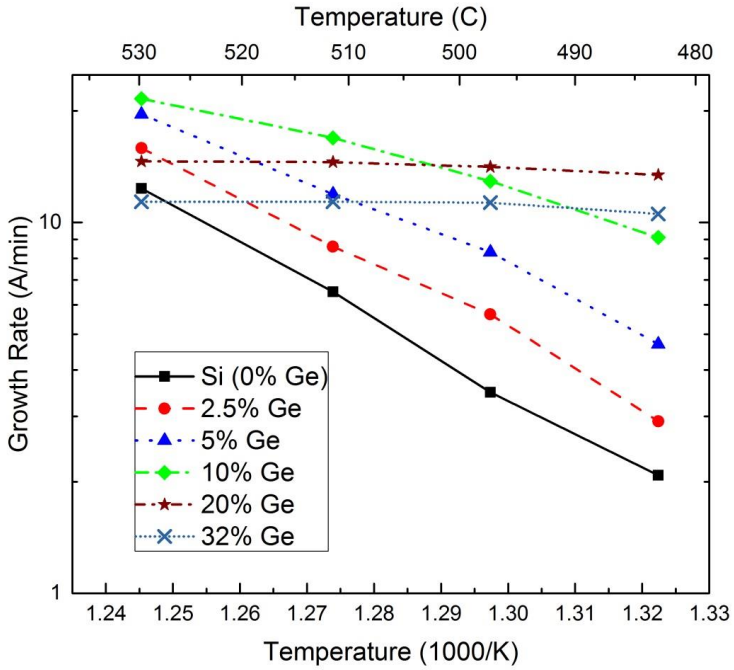

Figure 3.1: Arrhenius plot showing the dependence of growth rate on reciprocal temperature for different SiGe alloys grown by UHV-CVD. A transition from the temperature dependent, reaction rate limited growth regime at low germanium composition to a temperature independent mass flow limited regime for high germanium composition can be seen above 10 % Ge. Thickness data was collected using XRD and Bede RADS simulation software.

A typical growth procedure began with a dilute HF acid last pre-clean followed by insertion into the load lock then a pump down to UHV. Upon entering the growth chamber an initial silicon buffer layer was grown with a thickness of 200 Å before starting SiGe growth, in order to avoid any effects of growth delay and nucleation on the SiGe growth. The silane and germane flow rates were then changed to the desired flow rates without ramping. An immediate response was seen in the silane and germane peaks on the in-situ RGA, confirming the sharp transitions in gas flow. No

doping was used in these test layers. After the SiGe, a thin 40 Å Si cap was grown on top of the SiGe layer completing a typical SiGe HBT replica profile of a SiGe layer sandwiched between Si. The structures grown here do not have a ramp in germanium composition as a typical SiGe HBT would be expected to have. However, these test structures are of typical germanium concentrations and thicknesses to SiGe HBTs profiles of interest. Step profiles were grown instead of ramp profiles in order to better compare the results with both theory and results from the literature.

3.3 Morphology Characterization

Using atomic force microscopy (AFM), both the magnitude and the periodicity of the surface perturbations of the SiGe layers were measured. Samples used in this AFM experiment were all targeted at 32% Ge. The 3D growth that was observed consisted of both individual hill-like structures as well as elongated structures. The elongated structures were observed to align along orthogonal <100> and <010> directions as noted previously in literature [45], and seen in Figure 3.2a. A linear height profile was drawn along the <100> axis (diagonal of Figure 3.2a), and a perturbation periodicity (wavelength) of 240 nm was measured. A representative lateral profile over 1 μm is shown in Figure 3.2b. The wavelength of an average perturbation is in-line with predictions [48] and similar to other reports [45], [47]. For a sinusoidal amplitude wave, the root-mean square (RMS) roughness is proportional to the amplitude of the wave. As a way to compare the growth magnitude, or height, over relatively large areas and between different samples, the RMS values from AFM scans over 10 μm x 10 μm area were used.

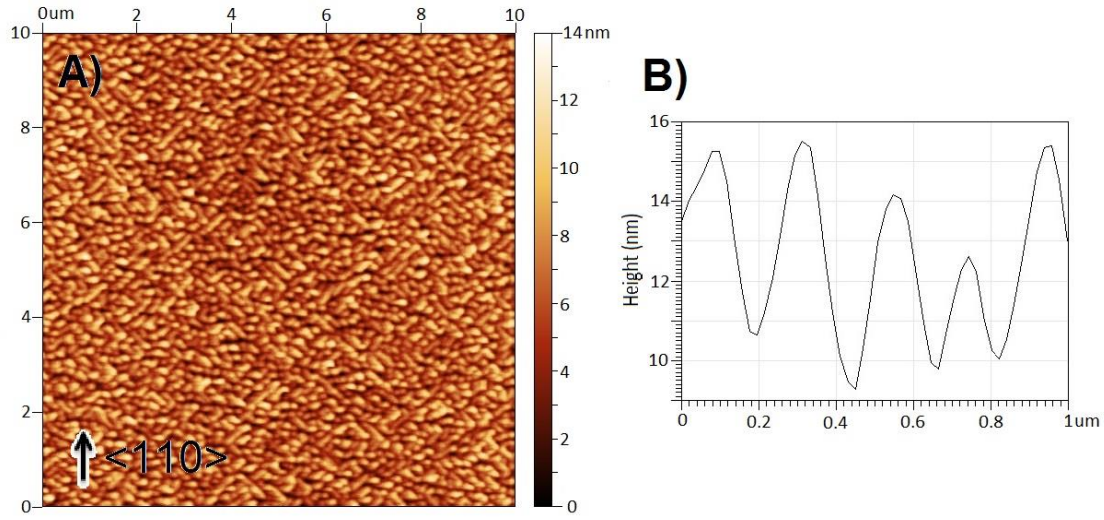

Figure 3.2: A) A typical AFM amplitude plot for growths in this study. Shown here is a 10 um x 10 um scan of a 32% Ge sample grown at 530 ºC with a target thickness of 400 Å and a growth rate of 12.7 Å /min. The vertical height scale is in nm, and the sides of the figure are aligned to the <110> directions. B) AFM height profile along the <100> direction, showing the periodicity and height distribution of the perturbations.

Once growth progresses, the atoms that get buried are essentially bulk and no significant diffusion of atoms is expected to take place at these growth temperatures. A silicon capping layer has been seen to have a smoothing effect on the surface morphology in literature [45], which is due to the silicon migrating to the wave troughs as it is deposited. For comparison, we did another growth at 530ºC with a target thickness of 400 Å, similar to the roughest sample shown in Figure 3.4 but without a silicon cap. With a silicon cap the RMS roughness was 28.9 Å, while without the silicon cap the roughness rose to 37.6 Å confirming the smoothing effect of silicon capping. A further example of the effects of capping can be seen in the

micrograph of Figure 3.3, where the morphology of the top silicon cap is flatter than the underlying SiGe layer.

In order to better observe the effect a 3D growth mode would have on a HBT structure, a sample was grown with a trapezoid-like germanium composition with 35% germanium at the peak. The film was grown on a substrate patterned with Poly-Si on SiO_2. The film was grown on a patterned substrate in order to simulate strain fields that exist in a structure more closely approximating actual HBT device architecture with a sloped germanium profile. Shown in Figure 3.3 is a TEM micrograph, in which surface perturbations can be seen. A slight waviness in the bulk of the layer can be seen but the predominant feature of the image is a distinct pileup, and then a corresponding thinning, of SiGe at the edge of the pattern where the crystalline layer meets the polycrystalline pattern. The exaggerated thickness feature was seen in all films that exhibited waviness, including some films that otherwise appeared smooth. A likely explanation for this is that there are additional stress fields due to the patterning that affect the growth of the film [51].

Compositional analysis using energy dispersive x-ray spectroscopy (EDX) was done on the thicker and thinner parts of the perturbations to confirm if any germanium segregation occurred. At the thicker part of the perturbation, marked A) in Figure 3.3, a peak count rate of 800 counts/sec was measured for Ge and the corresponding rate for Si at this point was 300 counts/sec. At the thinner part, marked B), a peak count rate of 700 counts/sec was observed and the corresponding rate for Si was 350 counts/sec. The differences in composition seem to indicate Ge segregation to the thicker region of the film, in agreement with the theory of Spencer et. al. that mobile Ge atoms are responsible for the surface morphology change.

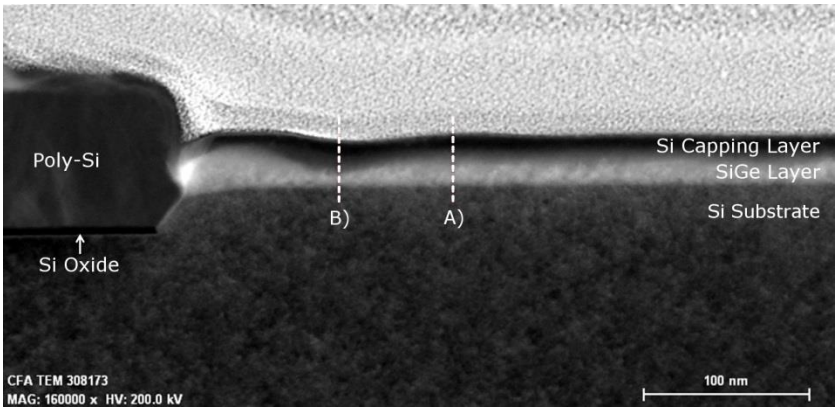

Figure 3.3: TEM image of a 35% target peak Ge composition SiGe layer sandwiched between two Si layers. The wafer was patterned with a thin silicon oxide and a thicker poly-silicon layer. Two vertical compositional scans were performed, the position of which are shown as A) and B) in the TEM photo, see text for details.

3.4 3D SiGe, Process Conditions and Modeling

Layers of varying thicknesses at varying temperatures were grown using the experimental procedure outlined above, the RMS roughness was measured and shown in Figure 3.4. As the growths were all done in the mass flow limited regime, there was no change in precursor flow or growth rate between samples, only growth duration and substrate temperature. In all samples the SiGe layer, as well as the silicon buffer and silicon cap, were grown at the same temperature for each sample run.

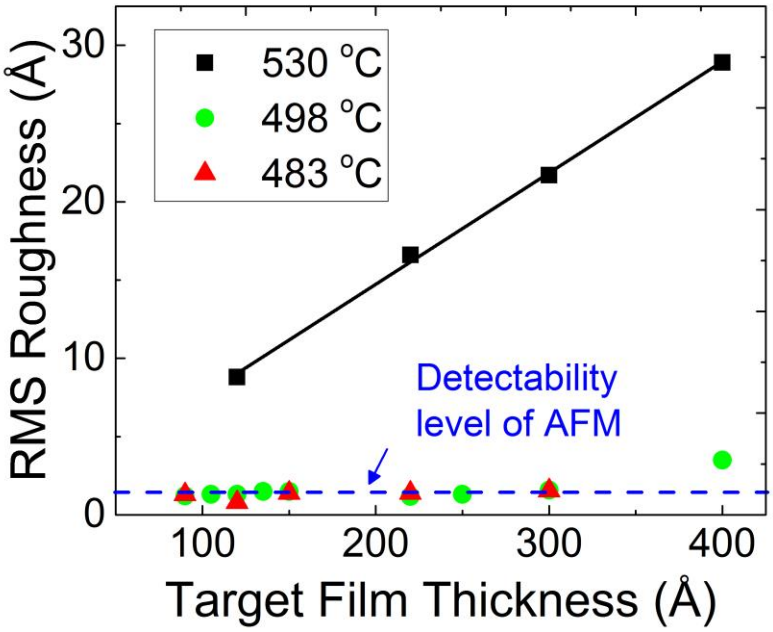

Figure 3.4: RMS roughness of SiGe box profiles with 32% Ge as a function of temperature and target film thickness. Film growth rate for all layers was 12.7 Å/min. A line has been drawn through the data at 530 °C to guide the eye. The detectability level (~1.5 Å) of the AFM height variation is shown as a horizontal dashed line, and is based on the average roughness measured by AFM for layers grown under similar conditions that showed no evidence of 3D growth.

Temperature affects many of the parameters important to the growth of these perturbations. The surface diffusion of atoms is dictated by an Arrhenius equation and is thus exponentially dependent on the temperature. The strain of the film is also dependent on temperature, a SiGe film at 530 °C is more strained than a SiGe film at 500 °C due to germaniums larger thermal expansion coefficient. Both of these effects would lead to a smaller growth rate of the perturbations at lower temperatures. The decrease in temperature clearly reduces the roughness in this study, with roughness values from films grown at 498 °C and 483 °C showing roughness values comparable

to the AFM background noise level. One data point, 400 Å at 498 ºC, shows a small increase in roughness; perhaps had thicker films been grown a continued rise in roughness would have been seen. For films grown at 498 ºC, an approximate value for the kinetic critical thickness is somewhere between 300 Å and 400 Å. From Equation 3.1, the growth of the surface perturbation grows exponentially with the thickness of the film if the growth rate of the film remains constant, $\hat{h} \propto Exp(\bar{h})$. However, the data at 530 ºC turned out to fit well to a straight line. It might be more appropriate then, using the same variables as Equation 3.1, to rewrite the 3D growth equation in a similar manner,

$$\hat{h} = \hat{h}_o + \sigma t = \hat{h}_o + \frac{\sigma \bar{h}}{\nu} \tag{3.3}$$

Or the roughness of the film is linearly proportional to some initial perturbation plus the growth rate of the perturbation multiplied by growth time. The time, is of course equal to the thickness of the film divided by the growth rate of the film. The kinetic critical thickness equation becomes,

$$h_c = \frac{\nu}{\sigma}(\hat{h} - \hat{h}_o) \tag{3.4}$$

It is worth emphasizing that σ, the growth rate of the perturbations, is the only temperature dependent variable in the equation. Fitting Equation 3.3 to the roughness data at 530 ºC in Figure 3.4, with the AFM background noise level (~1.5 Å), leads to a thickness of 3D growth of 14.1 Å (not shown in Figure 3.4) for the kinetic critical thickness. A drop in temperature of 30 ºC from 530 ºC to 498 ºC increased the kinetic critical thickness by approximately 20x from 14.1 Å to around 400 Å.

According to Equation 3.4, at an identical substrate temperature and film thickness, the roughness of the film should scale as 1/ν, or the reciprocal of the film growth rate. Figure 3.5 shows the RMS roughness versus reciprocal growth rate of

SiGe layers grown at 530 ºC with 300 Å target thickness and 32% Ge. To achieve different growth rates while maintaining the same alloy composition the total precursor flow rate of silane and germane was increased while the ratio between the two stayed the same. A linear fit was performed and an r^2 value of 0.988 was obtained, showing a relatively good fit to Equation 3.4, although more data points would likely improve the fit. If the fitted line was extrapolated out to arbitrarily large film growth rates (the y-axis intercept of fitted line) the film would be smoother, although to a minimum RMS of ~3.3 Å, which is above the AFM background level defined in Figure 3.4 and thus above the kinetic critical thickness. Thus, at 530 ºC, no matter how fast the growth rate is, at 300 Å the film will be rough.

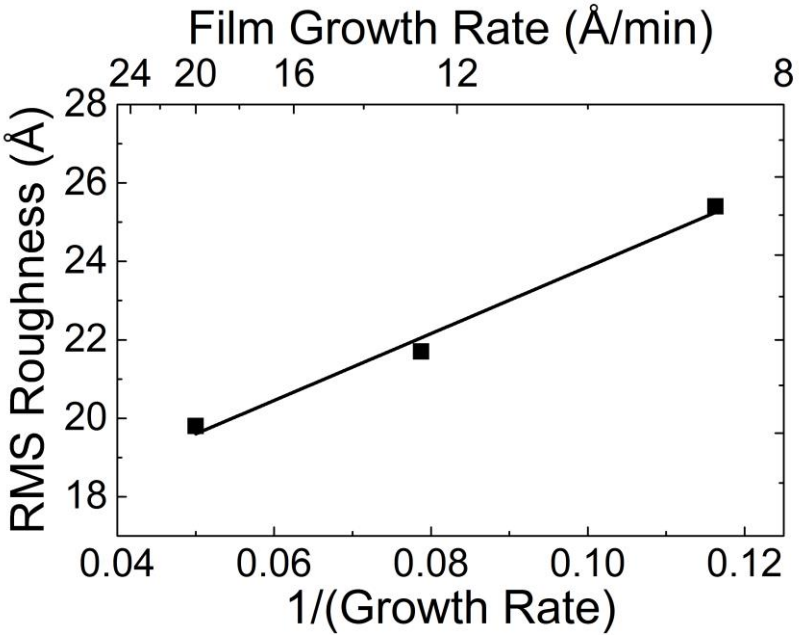

Figure 3.5: The dependence of RMS roughness of SiGe box profiles with 32% Ge on the growth rate. Note that the RMS roughness axis is a log scale. Growths were at 530 ºC, growth rate change was accomplished by changing total precursor flow rate. Layer thickness of all three layers was targeted at 300 Å.

3.5 Conclusion

The goal of this section was to measure the effect that increasing the growth temperature and decreasing the growth rate of the film will have on increasing the growth rate of the 3D growth. As previously noted, temperature changes during growth on the Oerlikon/Leybold Sirius UHV-CVD reactor are not possible in a production environment, and tradeoffs exist with lowering the growth temperature for an entire run. On the one hand, lowering the temperature will help improve smoothness, but on the other hand it causes the manufacturing throughput to fall off due to silicon buffer layers grown at a much lower growth rate. Based on these CVD growth studies it was found that increasing the growth rate of the silicon germanium deposition will reduce the surface roughness but not as much as lowering the growth temperature.

The growth of 3D islands has generated much interest lately in the application towards quantum dots which are interesting for their electronic [52] and optoelectronic [53] possibilities. Increasing the growth rate of SiGe surface perturbations could be desirable for the growth of SiGe quantum dots. In this application it would be more advantageous to grow at lower growth rates and higher temperatures in order to encourage 3D growth. However, Ge segregation, as shown in Figure 3.3, could present an issue.

Chapter 4

TETRASILANE AND DIGERMANE FOR THE ULTRA-HIGH VACUUM CHEMICAL VAPOR DEPOSITION OF SIGE ALLOYS

4.1 Introduction

Silicon germanium is an important material system for many devices; as mentioned in Chapter 3 it is the foundation of heterojunction bipolar complimentary metal- oxide semiconductor (BiCMOS) devices, it is also used as stressors for Si channels in CMOS integrated circuits [54]. These technologies require high quality strained crystals with smooth surfaces. The growth temperature during silicon germanium epitaxy is an important variable for many reasons, including controlling dopant diffusion, growth morphology, alloy gradients, and strain. Lowering the deposition temperatures, however, presents a problem with a reduced epitaxial growth rate during chemical vapor deposition (CVD), due to CVD epitaxy being a thermally activated chemical reaction. The hydride gas sources typically used in industry for SiGe epitaxy are silane (SiH_4) and germane (GeH_4), for which the decomposition reaction transitions to mass flow limited growth rate regimes at >670 ^oC and >350 ^oC, respectively [55], [56]. Higher order precursors are an important avenue of current research because increasing the order, n, of the precursors, for example Si_nH_{2n+2} where n>1, has been found to give a higher epitaxial growth rate at a given growth temperature. The reason for this increase is thought to be caused by the lower bond strength between the Group IV-IV bonds compared to the IV-H bonds with hydrogen. For example, in silicon, the bond between Si-Si atoms is $E_{Si\text{-}Si}$= 226 kJ/mol, which is

lower than Si-H E_{Si-H}= 318 kJ/mol. The lower bond strength allows for not only higher growth rates but also the capability to move to lower temperatures while maintaining growth rate and process throughput, which is believed to be from a deposition pathway through the hydrogen terminated Si surface conditions during growth at low temperature [57]. Two such higher order molecules relevant to silicon germanium epitaxy are tetrasilane (Si_4H_{10}) and digermane (Ge_2H_6). In addition to the higher growth rates, there has been interest in utilizing these two sources along with a Sn source to produce SiGeSn alloy films [58], a material with much interest for stressed CMOS [59], solar cells [60], and lasers [61]. To prevent Sn precipitation, relatively low temperatures are needed for SiGeSn epitaxy, and these low temperatures are incompatible with typical lower order precursors due to the above mentioned reaction rate limitation; hence the emphasis on higher order precursors. There has been little work, however, on the kinetic decomposition of higher order precursors for SiGe alloy growth. In order to properly utilize these molecules for industrial applications, a further understanding of the deposition characteristics of tetrasilane and digermane is warranted.

4.2 Details of UHV-CVD Epitaxial Growth

The epitaxy tool is an Oerlikon/Leybold Sirius CVD-300 ultra-high vacuum (UHV) CVD [32], as described in detail in Chapter 2. For this experiment, the Si wafer substrates were lightly boron doped (10-50 Ohm cm) <100> orientation, 125 mm in diameter. Only one target wafer was used at a time in this work and four dummy wafers on either side of it were placed immediately adjacent. Before epitaxy, the wafers were prepared with a standard RCA clean [38] that ended with a 1:100 hydrofluoric acid (HF) / deionized water solution dip for 5 minutes before the solution

was continuously diluted with 1 L/min of deionized water for 20 minutes in the dip tank outlined in Section 2.3.5. After preparation, the wafers were hydrophobic and hydrogen passivated [40], and were taken out of the DI water solution and immediately loaded into the CVD intro chamber within two minutes. No pre-bake of the wafers was used. The low temperature processing is in line with maintaining a low temperature budget for the entire epitaxial process. A typical interface oxygen contamination dose (O-dose) for this cleaning procedure was $7*10^{13}$ atoms/cm^2, measured by secondary ion mass spectroscopy (SIMS), close to that reported in [40] for a similar pre-epitaxial clean.

Process gases were not mixed with additional carrier gases and the total growth pressure during epitaxy was <0.1 Pa. The digermane and tetrasilane precursors were provided by Voltaix/ Air Liquide Advanced Materials. The germanium precursor is a 10% by volume digermane mix in H_2 gas, with a manufacturer specified moisture and oxygen level less than 0.1 ppm. The partial pressures noted in this work were individually measured at the growth temperatures using the method described in Section 2.3.4. The total pressure in the chamber was established by the turbo-molecular pumping speed and the gas flow into the chamber; the butterfly throttle valve was kept fully open, and there was no adaptive pressure control.

4.3 Film Analysis Techniques

A series of characterization techniques were used to observe the properties of the deposited Si and SiGe films, and to understand the relation between growth parameters and sample quality and crystallinity. X-Ray diffraction (XRD) and reflectivity measurements were performed using a Philips/Panalytical X'Pert MRD equipped with a high-resolution goniometer and a CuKα1 x-ray source (λ = .154056

nm). For diffraction measurements (XRD), a Bartels Ge (2 2 0) monochromator was inserted in the incident beam path (12 arc/s divergence), while a three-bounce Ge (2 2 0) analyzer was inserted in the diffracted beam path.

Film thicknesses, alloy composition, and crystallinity of the layers were also determined by variable angle spectroscopic ellipsometry (VASE) data. Spectra were acquired using a J.A. Woollam VASE with a computer controlled Berek waveplate compensator. For SiGe layers, the ellipsometric angles were fitted using a three-layer model consisting of the Si substrate, the SiGe layer, and native SiO_2. The optical constants for all layers were taken from the literature [62], and the SiGe and SiO_2 thicknesses as well as the Ge concentration were fitting parameters. For Si layers that were amorphous on a Si substrate, the ellipsometric angles were fitted using a three-layer model consisting of the Si substrate, the amorphous Si layer, and native/surface SiO_2. The optical constants for all layers were taken from the literature [63] and the a-Si and SiO_2 thicknesses were the only two fitting parameters.

Atomic Force Microscopy (AFM) was performed to evaluate the surface roughness and morphology of epitaxial films, using a Veeco/Bruker Dimension 3100 operating in tapping mode and captured with the Nanoscope V interface and software. AFM image handling was performed using Gwyddion AFM software [64].

To get a sense of crystal quality on an atomic scale, cross sections of epitaxy samples for transmission electron microscopy (TEM) studies were prepared using a Zeiss Auriga 60 SEM/FIB (scanning electron microscope with focused ion beam), with accelerating voltage of 30 keV for imaging, and Ga ion beam current of from 4 nA for milling down to 120 pA for polishing. Milled samples were mounted on a copper TEM grid using sputtered platinum handles. TEM imaging was performed

using a JEOL-brand JEM-2010F TEM instrument with an accelerating electron voltage of 200 keV using a zirconated tungsten emission source. The TEM system was also equipped with an EDAX-brand energy dispersive x-ray spectroscopy (XEDS) module for material identification.

4.4 Deposition Kinetics

The following two sections discuss the deposition characteristics of first amorphous and crystalline Si from tetrasilane, and followed by crystalline SiGe alloy films deposited by a co-flow of tetrasilane and digermane.

4.4.1 Tetrasilane Deposition Kinetics

Shown in Figure 4.1 is an Arrhenius plot of the growth rate of Si under varying conditions. The main thrust of this work is the deposition of crystalline Si by tetrasilane, shown as the solid black squares in Figure 4.1. For crystalline Si, above about 500 ^{o}C, there is a weak dependence on temperature, which is a hallmark of the mass flow limited regime, in which the precursor molecule reacts as soon as contact is made with the wafer and the growth rate in this region is highly dependent on precursor flux. The pressure dependence is shown by the solid red data point at 500^{o}C, which is crystalline Si grown at a higher pressure, 15 µbar, showing a slightly higher growth rate. The deposition rate with pressure is also shown in Figure 4.2, where, as the pressure is increased, the growth rate increases at a reaction temperature of 550 ^{o}C.

At temperatures below 500 ^{o}C for Si, the growth rate was strongly dependent on temperature with an activation energy of around 1.4 eV, which is similar to the activation energies reported in the literature for silicon films: 2.1 eV for silane in an identical hot wall UHVCVD [27], and 1.86 eV for trisilane in a reduced pressure CVD

(RPCVD) [65], as well as an activation energy of 1.3 eV for germanium films grown with digermane in H_2 ambient by RPCVD [66], and 1.56 eV for Ge grown by gas source molecular beam epitaxy (GSMBE) [67]. At low temperatures, the reaction rate limited regime is probably a surface hydrogen limited regime, in which the precursor molecule is inhibited from reacting with surface sites that are filled and passivated with hydrogen. Deposition is limited by hydrogen desorption in this regime [68]. The solid red data point at 450 ^{o}C is crystalline Si grown at a higher pressure, showing only a very small increase in growth rate. The deposition rate with pressure is also shown in Figure 4.2, where, as the pressure is increased, the growth rate increases negligibly at a reaction temperature of 450 ^{o}C.

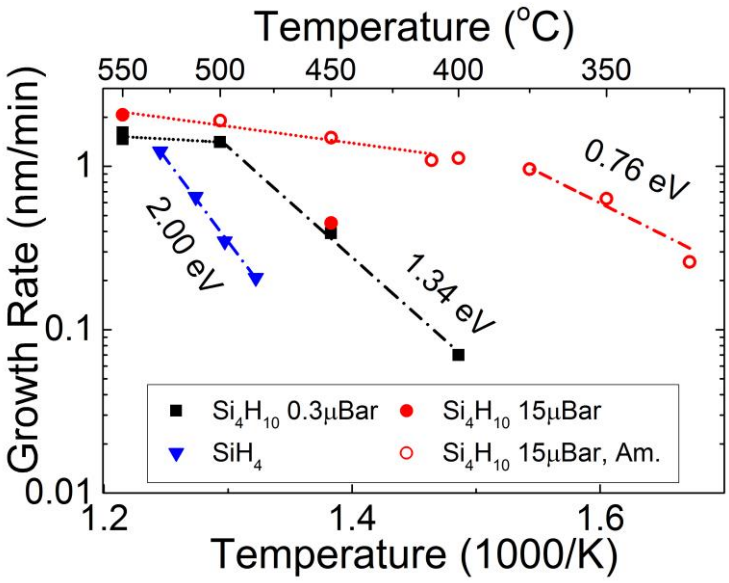

Figure 4.1: Arrhenius plot of the growth rate of Si and amorphous silicon (a-Si) from tetrasilane and silane. Two growth regimes are evident. A reaction rate limited regime at lower T, and a mass-flow limited regime at higher T, which has less T dependence.

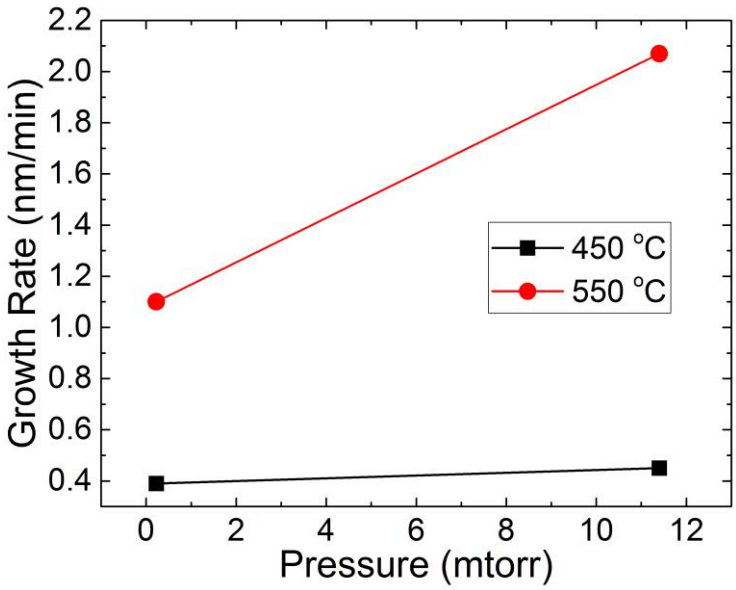

Figure 4.2: The growth rate of crystalline Si by tetrasilane as a function of growth chamber pressure for two different substrate temperatures. This graph shows the difference that pressure makes in the mass flow limited regime (550°C) and the reaction rate (hydrogen desorption) limited regime (450°C).

All growth rates measured for tetrasilane were higher than that measured for SiH_4 at IBM, which are shown as the blue inverted triangles in Figure 4.1. As the temperature decreased, the discrepancy between the higher growth rate of tetrasilane and the lower growth rate of monosilane increased. At 500 °C, the growth rate for tetrasilane is almost an order of magnitude higher, proving the worth of the higher order precursor for low temperature deposition.

Amorphous Si was also grown with tetrasilane. The amorphous nature of these samples was measured by VASE, which showed broad reflection peaks, being a hallmark of amorphous material, and by XRR which showed a measureable density difference between the deposited layer and the crystalline Si substrate. For the initial

growths in the CVD, the pre-epi clean was not as good as is needed to be to insure low O-dose at the epitaxy interface. An example of a high O-dose SIMS for a sample that was amorphous can be seen in Figure 4.3. A few high O-dose samples were measured on SIMS, showing interfacial O-doses between $1.2*10^{14}$ cm^{-2} and $2.5*10^{15}$ cm^{-2}. It is thought that these high O-doses lead to amorphous Si films.

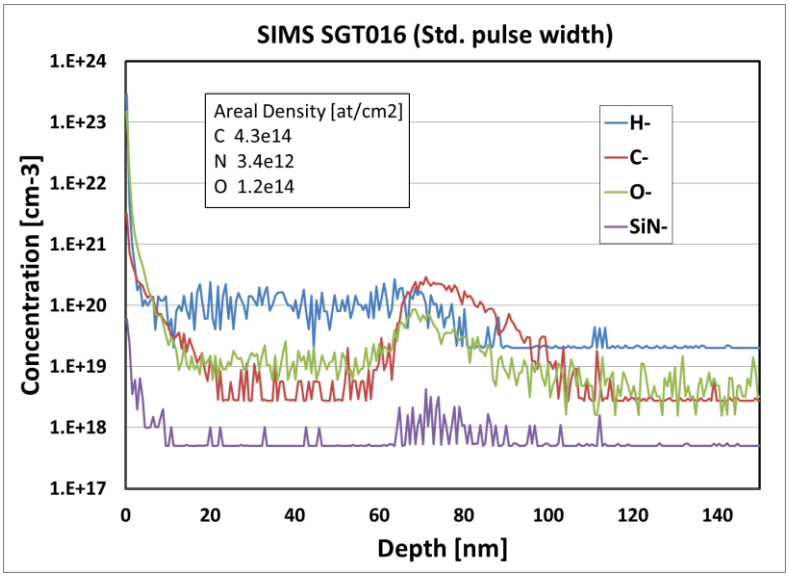

Figure 4.3: SIMS of SGT016 showing a high O-dose attributed to a deficient pre-epitaxy clean. The epitaxy interface can be seen by noticing the appearance of O and C contamination. The inset shows the calculated interfacial contamination doses, with a high O-dose of $1*10^{14}$ cm^{-2}.

As shown in Figure 4.2, at low temperatures in the reaction rate limited regime, the growth rate of Si varies only slightly pressure, and in Figure 4.1 the growth rate is shown to be decreasing with T with an activation energy of 1.34 eV. Typically, in CVD, the activation energy is ascribed to the termination of the Si surface by hydrogen inhibiting further deposition [68]. The open red circles in Figure

4.1 show that amorphous Si can deposit at very low temperatures, however, and the deposition rate does not begin to decrease until about 400 ^{o}C, at which point the activation energy is only 0.76 eV. The additional deposition rate is most likely due to a weaker hydrogen bond on an amorphous Si surface than that of the crystalline Si surface. The exact mechanism for the weaker bond remains unknown, but the important conclusion to draw from the amorphous Si deposition rate is that tetrasilane is still reactive at the low temperatures, exhibited by the molecule breaking down and depositing, which encourages the direction of using this precursor for lower temperature material growths including alloys of SiGeSn.

4.4.2 SiGe Alloy Deposition Kinetics

In order to assess the SiGe growth kinetics, the tetrasilane flow rate was held constant at a SiH_4-calibrated mass flow controller reading of 7 sccm (calibration discussed in Section 2.3.4), the tube pressure was measured to be 0.06 Pa with no other gasses flowing. The digermane flow was varied from a nitrogen-calibrated mass flow controller reading of 0-25 sccm (calibration discussed in Section 2.3.4) to generate different alloy compositions. Symmetric (004) ω-2θ XRD curves were used to measure the alloy composition and film thickness. As the digermane gas pressure increased, the germanium film composition increased, as shown in Figure 4.4a for different growth temperatures. The relationship between gas composition and alloy composition is roughly linear with a higher slope for higher substrate temperatures. As the temperature of the substrate was increased from 400 ^{o}C to 550 ^{o}C, proportionally less digermane gas was needed to achieve the same germanium concentration in the film. Growths with trisilane and monogermane exhibit the same trend [65], whereas mono-silane chemistry exhibits the opposite trend, namely an increase in germanium

concentration in the film with decreasing temperature [69]. Figure 4.4b shows the growth rates of alloys from Figure 4.4a. For the alloy compositions grown, the measured peak growth rate temperature is 525°C for alloys with germanium content <8% and 500°C for larger germanium contents.

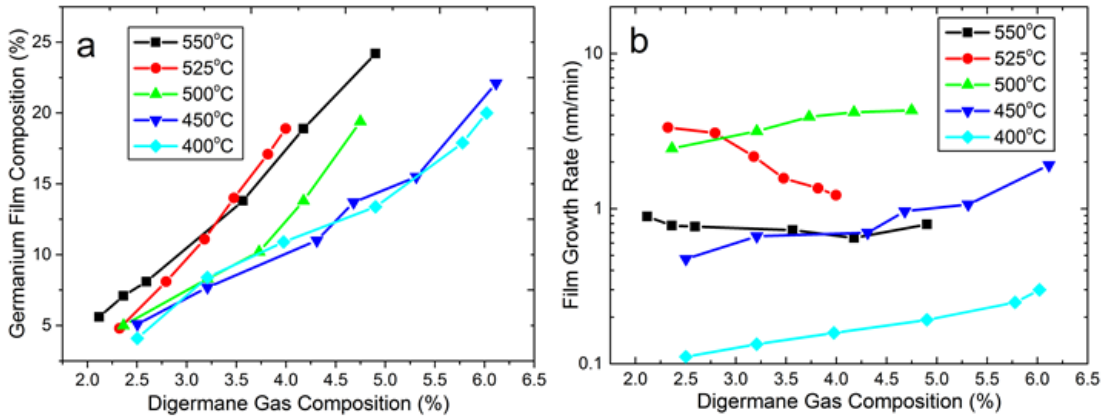

Figure 4.4: (a) The germanium film composition plotted against the digermane gas composition for different temperatures of growth. The digermane gas composition was calculated from partial pressures by the formula $Ge_2H_6/(Ge_2H_6+Si_4H_{10}+H_2)$ where the hydrogen came from the digermane gas mixture. (b) The growth rate of silicon germanium alloy films as a function of digermane gas composition for different temperatures of growth.

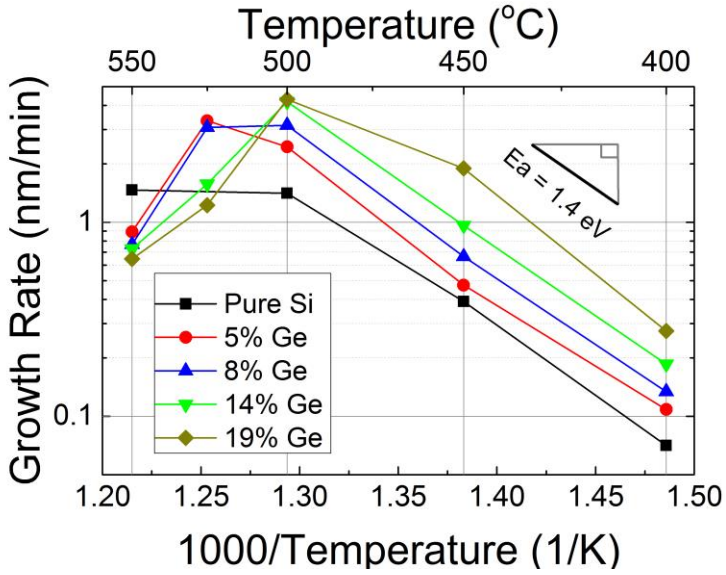

Figure 4.5: Arrhenius plot of growth rates vs deposition temperatures for films grown by a combination of tetrasilane and digermane for alloy compositions up to 19% germanium. A slope of 1.4 eV is shown in the upper right of the graph, corresponding to the activation energy of the reaction rate, temperature limited regime.

The data from Figure 4.4 is separated by alloy composition and shown as an Arrhenius plot in Figure 4.5. The deposition rate for Si is shown as the black squares and was discussed in the previous section. For growths at 550°C, The growth rate of silicon-germanium alloys *decreases* as the Ge concentration *increases*, which is typical for the mass flow limited regime in CVD for silicon germanium and is seen in many reports for CVD of SiGe by different precursors [27], [56], [70]. The peak in growth rate around 500°C will be discussed in further detail in Section 4.6.

The SiGe alloy films grown here show a similar, low temperature, reaction rate limited regime growth rate dependence as the Si films. Hydrogen desorbs from the germanium surface at a much lower temperature than silicon, leading to a higher amount of available sites on the SiGe alloy surface compared to a pure Si surface and

thus a higher deposition rate for higher Ge content alloy films at the lower temperatures [71]. In this work, for the SiGe alloys (<19% Ge), the temperature dependence of the deposition rate in the reaction rate limited region is approximately 1.4 eV, which is the same as for pure Si.

It is interesting to compare the growth rates for alloys from tetrasilane and digermane precursors to the growth rates from the traditional precursors silane and germane in a similar hot wall UHV-CVD tool. In order to do this, the data from Figures 3.1 and 4.5 are combined in Figure 4.6. At the higher temperatures explored here, the growth rates from tetrasilane and digermane are of the same order of magnitude as that of the traditional precursors [27], perhaps lower growth rate for 550^{o}C. For temperatures less than 500^{o}C the growth rates of all alloy compositions grown with tetrasilane and digermane are 2-3x that of silane and germane, which confirms the expectation that higher order precursors provide increased growth rates at lower temperatures than traditional precursors.

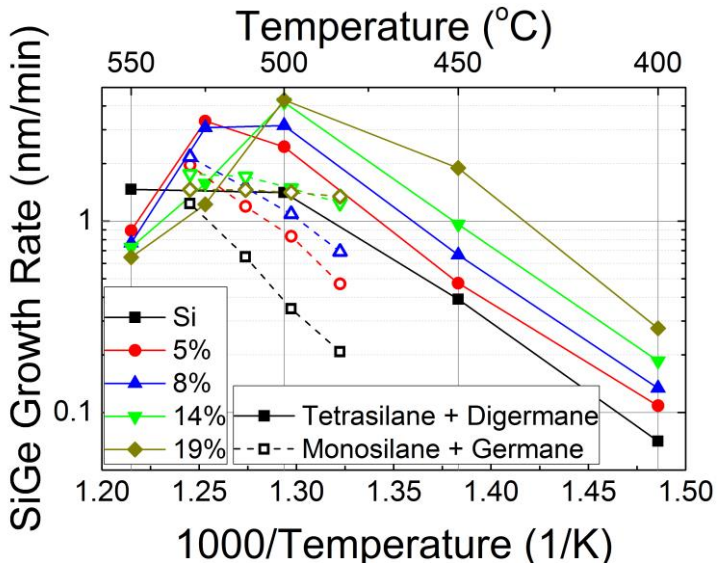

Figure 4.6: A growth rate comparison between monosilane and monogermane (hollow points) and tetrasilane and digermane (solid points).

A peak can be seen in the growth rate at 500°C – 525°C for all alloy compositions, excluding pure Si. The peak in growth rate becomes more exaggerated with increasing germanium composition, with almost an order of magnitude increase in deposition rate than the rate at 550°C. The peak deposition rate shifts to lower temperatures with increasing germanium composition, following the changing transition temperatures from the reaction rate limited to the mass flow limited regimes. Further discussion on the growth rate peak is in Section 4.6.

4.5 Film Characterization

4.5.1 Si/ a-Si Film Characterization

The Si grown by tetrasilane in the UHVCVD was analyzed by various techniques to assess its quality. The growth rate and crystallinity of the films was

measured by VASE, with representative data shown in Figures 4.7 and 4.8. Figure 4.7 shows a crystalline Si sample, grown with tetrasilane at a reactor temperature of 550 ^{o}C. The crystalline nature can be deduced by the sharp peaks present just above 3 eV and 4 eV in the imaginary part of the complex dielectric function, attributable to absorption between the higher bands of the Si energy band structure. Sharp peaks mean a well-defined band structure and thus long range crystal order. The VASE data in Figure 4.7 is identical to that of bulk Si, showing that tetrasilane films exhibit bulk-like qualities.

The crystalline nature of Figure 4.7 can be contrasted with the sample shown in Figure 4.8, an amorphous Si sample grown with tetrasilane at 450^{o}C, which shows one very broad peak in <e2> located just above 3 eV. The film thickness was inferred from interference fringes in VASE, thus the growth rate could be extracted for amorphous Si films. The interference arises because an amorphous Si film has a different index of refraction than crystalline Si. An example of this fringing can be seen in Figure 4.8 around 2 eV in both the real part and the imaginary part of the dielectric function.

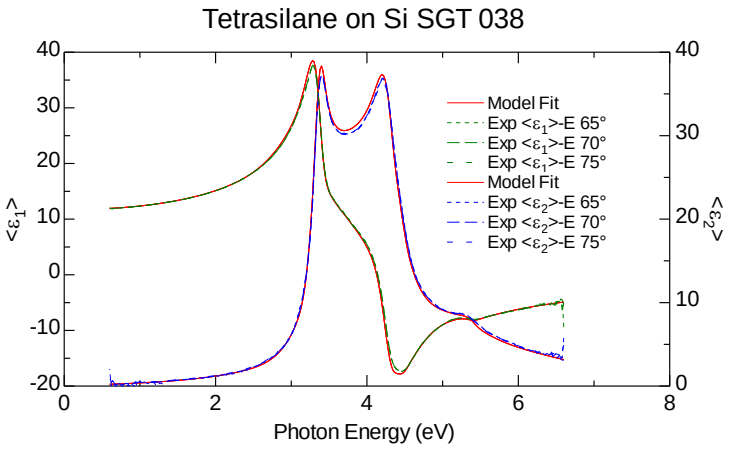

Figure 4.7: VASE dielectric function of SGT038, a crystalline Si sample grown with tetrasilane at 550 ºC. The data shows two curves, the orange is the real part of the complex dielectric function and the purple curve is the imaginary part of the complex dielectric function.

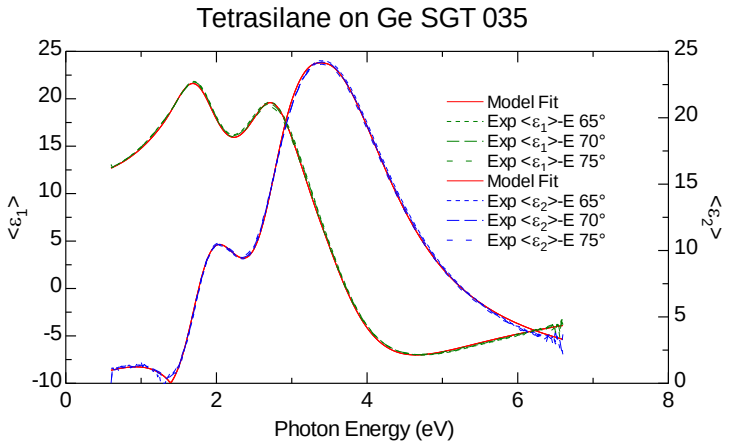

Figure 4.8: VASE dielectric function of SGT035, an amorphous Si sample grown with tetrasilane at 450 ºC. The data shows two curves, the orange is the real part of the complex dielectric function and the purple curve is the imaginary part of the complex dielectric function.

The film thickness and the growth rate for crystalline Si grown on Si substrates are not able to be measured by VASE because there is no contrast between the film

and the substrate. To overcome this difficulty, a SiGe marker layer was inserted between the Si substrate and the pure Si layer. The marker layer makes finding the thickness of both layers possible using (004) ω-2θ scans, then modeling the data using XRD software. An example of an (004) ω-2θ scan is shown in Figure 4.9. The peak associated with diffraction from the Si substrate is the large peak at around 34.6º, the peak associated with the SiGe layer is the large peak around 34.3º, and the series of small peaks are Pendellösung, or thickness, fringes. The appearance of a multitude of thickness fringes indicates a strained and coherent layer stack, and points toward a high quality growth.

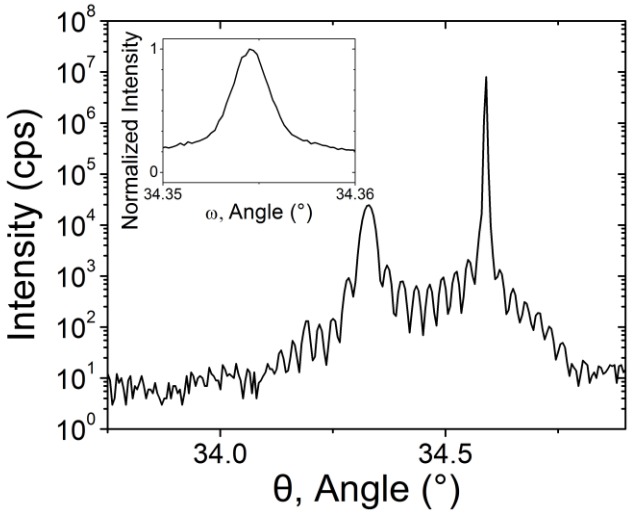

Figure 4.9: X-ray Symmetric (004) ω-2θ measurement showing diffracted intensity versus Bragg angle of a 10.2% Ge, 176nm thick SiGe layer capped with 26.5nm of Si. Inset: ω rocking curve around the SiGe layer peak.

In order to assess the roughness of samples grown with tetrasilane, AFM was performed, and a representative sample is shown in Figure 4.10. Samples grown with

tetrasilane were smooth, with RMS roughness values <0.5 nm. Comparable roughness was measured for bare Si wafers on the same AFM tool.

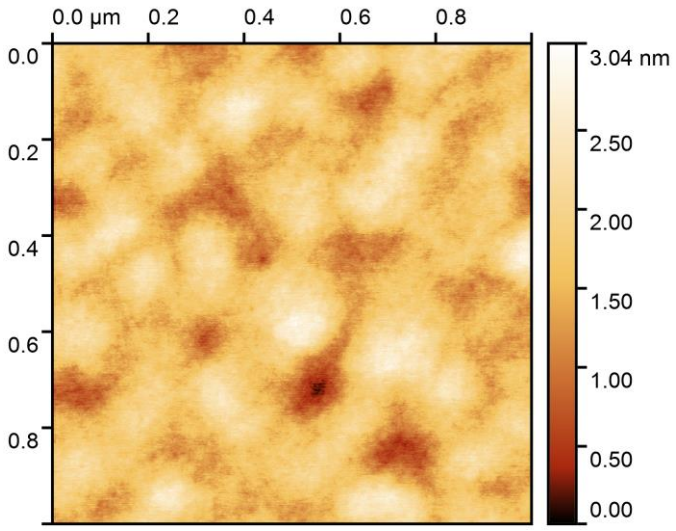

Figure 4.10: 1um x 1um AFM area measurement of sample SGT098; a 62 nm crystalline Si layer, grown from tetrasilane at 550 °C. The rms surface roughness is R_{rms}= 0.38 nm, and the peak-to-peak roughness is R_{max}=3.04 nm.

Cross sections imaged via HR-TEM showed a crystalline Si epitaxial layer with no clear defects or inhomogeneity, as in Figure 4.11, with no clear interfacial defects at the substrate epitaxy interface. Additionally, electron diffraction patterns as in the Figure 4.11 inset, were fully symmetric and sharp with minimal haze, indicating high quality single crystal material.

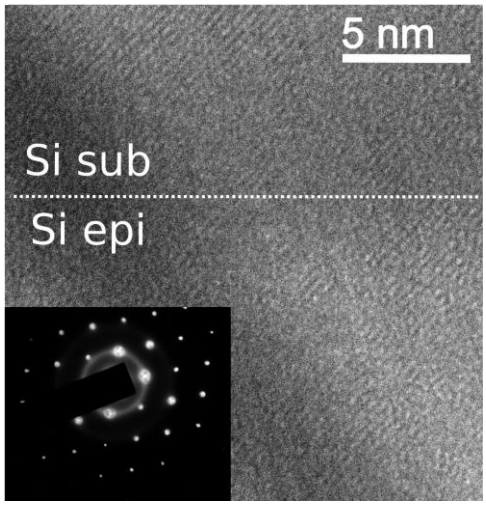

Figure 4.11: HRTEM micrograph of a 90nm Si on Si <100> substrate, grown at 500°C taken at the substrate-epi interface. The horizontal line denotes the position of the interface with the substrate indicated as the *top* half of the image. Inset: transmission electron diffraction pattern of the crystalline Si epi-layer, showing a highly ordered single crystal.

Crystalline tetrasilane was found to deposit layers with bulk like VASE results, XRD indicating high quality strained SiGe layers, AFM roughness < 0.5 nm RMS, and a well ordered crystal diffraction pattern in TEM with no defects or other distortions apparent. These measurement techniques indicated that the Si and epitaxial layers grown with TS were high quality and comparable to layers grown with mono-silane.

4.5.2 SiGe Alloy Film Characterization

In order to assess the quality of SiGe thin films grown with tetrasilane and digermane, a representative set of three similar layers grown at three different temperatures were characterized in a growth temperature analysis study: Sample A at the lowest growth temperature of 450 ^{o}C, sample B at an intermediate growth

temperature of 515^{o}C meant to correspond to the growth rate peak, and sample C at a higher temperature of 550^{o}C. A summation of the data presented in this growth temperature study is shown in Table 4.1.

The growth rate and composition of the films were measured using symmetric (004) ω-2θ XRD scans in the Panalytical X'Pert system described in Section 4.3, and modeled using Panalytical Epitaxy software. The ω-2θ XRD curves show a clear layer peak and fringing, shown in Figure 4.12, indicative of high crystalline quality. Slight variations in the peak width and fringe separation between samples were attributed to variations in the film thickness and composition rather than being characteristic of the growth temperature. The ω- full width at half maximum (FWHM) for the SiGe layers was found to be similar to that of the underlying Si substrate, showing no detectable broadening, which indicates there was no significant contribution to the layer peak due to dislocations, tilt, or twist relative to the substrate.

Further analysis of the epilayers by direct counts of etch pit defects using a dilute Secco etch [72] yielded Threading Defect Densities (TDD) on the order of 10^5 /cm^2 . For 21% germanium SiGe alloy layers grown by a combination of di-silane and digermane, a relationship was measured between the SIMS interface doses of oxygen and the TDD [39], in which dislocation densities of 10^6 cm^{-2} were measured for SIMS O-dose greater than $3*10^{13}$ O atoms/cm^2. Similar numbers for TDD ($3*10^5$ cm^{-2}) and SIMS O-dose ($7*10^{13}$ atoms/cm^2) were measured in this work, indicating that the material grown by tetrasilane and digermane is no more defective than material grown by industry standard disilane and germane.

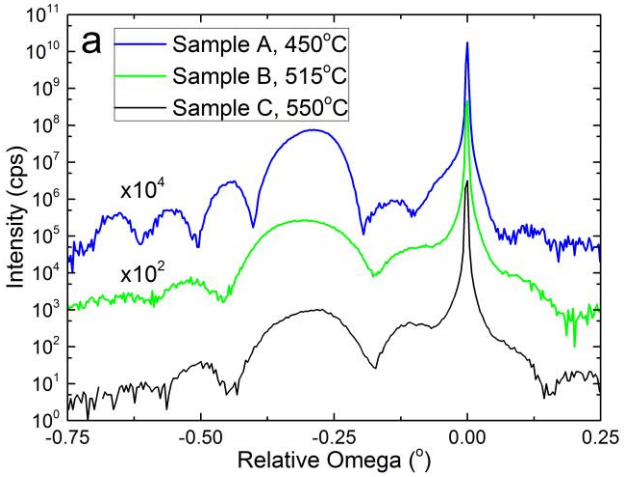

Figure 4.12: ω-2θ rocking curves of the three samples mentioned in the text. Very similar curves are measured between samples, with more fringes visible for Sample A than either of the others.

The surfaces of films grown for commercial devices typically require root mean square (RMS) roughness < 1 nm in order to maintain a planar structure during device manufacture, and thus it is important to consider the surface morphology aspects of growth. In order to assess the roughness of samples grown with tetrasilane and digermane, AFM was performed, and shown in Figure 4.13 for the samples of Figure 4.12. Sample A, grown at the lowest temperature of 450°C, is the smoothest sample with an RMS roughness of 0.1nm. An RMS roughness of 0.1 nm was also measured for a clean Si wafer, not shown here, implying that the roughness measured for Sample A is at the capability of the AFM system setup and/or that its roughness is as smooth as an epi-ready wafer. The roughness of the SiGe samples in Figure 4.13 increased with higher temperatures. Sample B, grown at 515°C, showed a roughness value higher than what was measured at temperatures both above and below. The increase in roughness was small, roughly 0.8 nm RMS which corresponds to an

increase in the maximum height differential, Rmax, of ≈7 nm. A similar roughness vs. temperature trend was observed for all alloy concentrations, with the lower temperature growth of films resulting in smoother layers, and with higher temperature growths resulting in rougher layers, and growths at intermediate temperatures corresponding to the growth rate peak resulting in the largest roughness values. The surface for sample B seemed to exhibit small hills of material across the surface with no apparent orientation of the hill pattern. The hills were approximately 100 nm wide with a height of 3-6 nm, or up to 10% of the film thickness.

There have been reports on the increased likelihood that higher order precursors have gas phase reactions which could deposit observable particles on the wafer surface. Gas phase reactions are not expected at the low pressures maintained in these experiments (<0.1 Pa total) due to the large mean free path at that pressure, which would tend to preclude them. In addition, the roughness seen here was small, regular, and did not resemble the sparse, point-like roughness of gas phase particles observed in other work [73].

The same set of three samples were also analyzed with VASE, data not shown here, with the system as described in Section 4.3. Excellent agreement between data and model were found, as well as agreement with other measurements, as seen in Table 4.1.

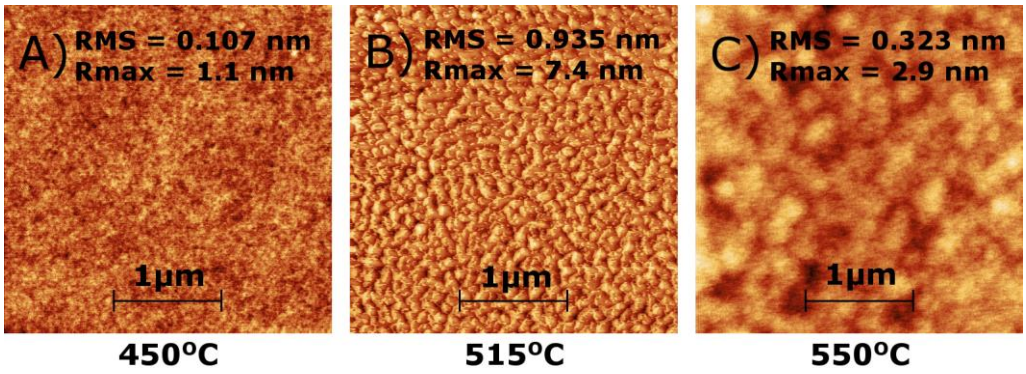

Figure 4.13: 3 µm x 3 µm AFM image series of 11% germanium samples 50 nm thick comparing the surface roughness vs. growth temperature throughout the growth rate peak region. Indicated are the RMS values of surface roughness and the maximum peak to peak roughness Rmax.

Table 4.1: Summary of XRD, VASE, and AFM characterization results presented in this growth temperature analysis study.

	XRD		VASE			AFM
Growth Temp	Ge %	Thickness (nm)	Ge %	Thickness (nm)	SiO2 Thickness (nm)	Roughness (nm)
450oC	11.6%	51.4	11.7%	49.5	4.6	0.107
515oC	12.2%	37.4	11%	34.4	2.3	0.935
550oC	11.8%	40.7	11.8%	39.3	3.9	0.323

4.6 Discussion of SiGe Growth Rate Peak

An unanticipated result of this work was the sharp growth rate peak observed near 500 °C in Figure 4.5. A peak in growth rate from the deposition of germanium films from digermane alone has been shown in only two previous reports; films grown by RPCVD [66] and by GSMBE [67] on both Si and Ge substrates. There was also a small increase in growth rate for the transition temperature region (between the mass-flow and the reaction-rate limits) at T ≈ 700°C in the growth rate data reported by

Greene et al. [70] utilizing disilane and digermane for 20% Ge layers by GSMBE, but this peak in growth rate was not discussed by the authors. For similar SiGe alloys grown by CVD, however, we found that the growth rate increased by almost an order of magnitude from the mass transport (high temperature) region to the growth rate peak temperature, as in Figure 4.5. It is worth noting that all observations of such a growth rate peak, both here and in literature, are in reactions of higher order precursor molecules, specifically digermane.

The peak growth rate occurred at approximately 525 ^{o}C for 5% Ge, at 500-525 ^{o}C for 8% Ge, at 500 ^{o}C for 14% Ge, and somewhere between 450 and 500 ^{o}C for 19% Ge; as can be seen in both Figures 4.4b and 4.5. The temperature of the growth rate peak appears to follow the transition temperature from rate limited to mass flow limited, and thus shifts with alloy composition, rather than happening at a particular fixed temperature. The shift of the growth rate peak in temperature, as the Ge composition is changed, leads credence to the idea that the growth rate peak is a phenomenon associated with the growth of the alloy itself and not gas phase phenomena, because the temperature at which the precursor gasses decompose would be fixed for a given molecule. With the longer mean free path, gas phase reactions are also not expected to have a large contribution in UHV-CVD. Bramblett et al. [67] observed a peak in growth rate for the growth of germanium on both silicon and germanium substrates using digermane, and linked it to an increased film roughness at the growth rate peak temperature. The roughness shown in sample B, Figure 4.13, grown at the growth rate peak, however, is much different than the sharp (133) facet profile seen in [67]. The roughness observed in the Bramblett work had a periodicity of ≈ 1 μm and a height of roughly 30% of the total film thickness whereas the lateral

hill size observed in this work was on the order of ≈100 nm with a height of roughly 10% of the film, exhibiting much different scales. As the morphological characteristics of Ge films grown in [67] and the SiGe films shown in this work are different, it cannot be determined if the features are the result of the same phenomena.

In strained SiGe alloy layers, it is possible to have an energetically favorable rough or 3D surface, in a very similar way to Ge growth on Si, as the strain due to pseudomorphic growth can be relieved through surface corrugations [45]. No reason was given in [67] as to a cause for the reported 3D growth in germanium on germanium growths, and there is no strain in this system. Hydrogen is known to provide an advantage to germanium growth on silicon as it acts as a surfactant in the epitaxial growth process, smoothing films that would otherwise relax by forming 3D surface morphology due to strain buildup [74]. The smoothness of SiGe films grown in the low growth temperature, hydrogen limited regime, such as Sample A above, supports the hypothesis that hydrogen has a smoothing effect on SiGe alloy films. The smoothing of SiGe samples with reduced growth temperature has been reported before for the traditional precursors silane and germane as well [27], [45]. It is possible that the roughness appearing at 515^{o}C in Figure 4.13 as the growth temperature increased past the hydrogen limited regime was simply due to the decrease of the amount of hydrogen on the surface of the film and the subsequent reduction of the surfactant effect, resulting in strain-induced roughening.

The growth rate peak was observed to shift with alloy concentration following the transition from mass-flow limited to hydrogen desorption limited temperature regimes, which happens at lower temperatures for increasing Ge concentration. In addition, the onset of 3D growth also decreases in temperature with increasing

germanium concentration. The appearance of 3D surface morphology and the growth rate peak both correspond to the intermediate temperature region. Since this is also the temperature where H-termination is no longer governing the deposition kinetics, it is possible the phenomena of H desorption and 3D growth are interlinked. While the tendency of SiGe films to roughen with increasing growth temperatures is not unique to higher order precursor molecules, the decrease in film growth rate as the temperature is further increased does appear unique to higher order precursors.

4.7 $SnCl_4$ for UHV-CVD

Some initial experiments were performed with Tin-Chloride and Digermane in the UHV-CVD to test its compatibility. The choice of, and issues with, Tin-Chloride was outlined in Section 2.3.3. The growth profile chosen was to first flow Digermane into the chamber onto a Si wafer, and only activate the $SnCl_4$ flow after a thin layer of germanium had been deposited. This method was chosen so that any unforeseen issues with growth incubation times or wafer heating could be avoided. A time-of-flight secondary ion mass spectroscopy (TOF-SIMS) measurement of such a growth is presented in Figure 4.14, for a Sn to Ge mass flow ratio ($SnCl_4/Ge_2H_6$*0.1) of 66% and a growth temperature of 285^{o}C. The layer can be seen to start at the point in depth at which the signal from the Si substrate stops and the Ge signal increases. There is a tail on the Ge signal that extends into the Si substrate that is presumably due to drive-in effects from the etching. The point at which the Sn precursor is turned on is shown, however the Sn intensity is not seen to increase. This would imply that no Sn is incorporated above the detection limit of the TOF-SIMS tool, which was not measured but is typically less than 0.1 atomic %, implying that Sn was not incorporated even to the solubility limit as shown in 1.3.

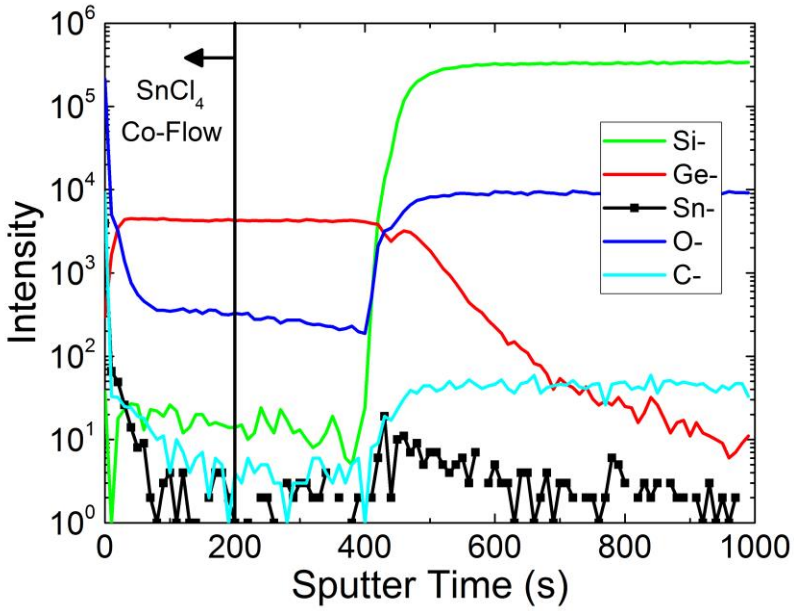

Figure 4.14: TOF-SIMS of a sample grown with a co-flow of $SnCl_4$ and Ge_2H_6. Elemental intensity is plotted as a function of increasing sputter time or, if the etch rate were known, increasing depth. The time in the growth at which the $SnCl_4$ source was opened is shown.

Sn was not able to be successfully incorporated into Ge films in the UHV-CVD environment at 285^{o}C. At lower $SnCl_4$ flow rates the Sn was not seen to incorporate, while at higher flow rates etching of the film was observed, as seen in Figure 4.15. It is important to reiterate that, due to the film stack grown here, the etch rate here is the etch rate of germanium films. The Ge film roughness was also observed to decrease with the increase in $SnCl_4$ flow rate. $SnCl_4$ has previously been seen to provide some etching in RP-CVD [75]. It could be that due to the much lower pressures employed here the Cl atoms provided additional etching, further experiments are being conducted on the UHV-CVD to test if this hypothesis is true with the use of the butterfly valve mentioned in Section 2.2.

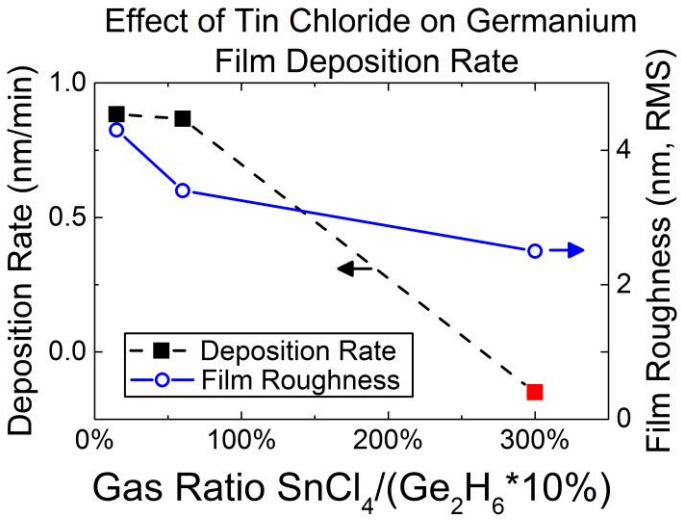

Figure 4.15: Effect on the film of co-flowing $SnCl_4$ with Ge_2H_6 at 285°C. At higher $SnCl_4$ concentrations the film is smoother but with decreasing growth rate until the process becomes etching (shown as red square).

4.8 Conclusion

Tetrasilane and digermane precursors produced CVD layers with bulk-like crystalline quality, low surface roughness, with higher growth rates and at lower temperatures than the traditional precursors silane and germane. The samples grown with tetrasilane and digermane at lower temperatures were found to be less defective with smoother surfaces than the samples grown at higher temperatures. A peak in growth rate was observed between the reaction rate (hydrogen limited) low temperature regime and the mass flow limited high temperature regime. The growth rate peak has only been noted in germanium growth by digermane, and has not been previously reported in any alloy growth. The peak growth rate temperature also corresponded to an increase in surface roughness. Tin-Chloride was trialed as a tin-containing, shelf-stable precursor. Although initial experiments show etching with no apparent Sn incorporation, they do show that the precursor is reacting even at low

temperatures. Further work is warranted to explore whether SiGeSn deposition is possible with $SnCl_4$ in a UHV environment.

Chapter 5

MBE GROWTH OF DOPED GERMANIUM TIN ALLOYS WITH HIGH TIN CONTENTS

5.1 Introduction

Described in this chapter are the epitaxy innovations that were made in order to achieve the high Sn content GeSn homojunction photodiodes of Chapter 8. These innovations include the development of novel dopants of GeSn, both p- and n-type, and the exploration of low growth temperatures and high growth rates to achieve high Sn contents crystalline films. The influence of the substrate temperature during growth is investigated, and the process on record (POR) recipe for Ge virtual substrates by MBE is presented.

5.2 Doping

N-type doping is particularly important for Ge based optoelectronic applications because it allows control of the energy band structure. For example, degenerate level n-type doping has been used to saturate the L-valley of Ge with carriers, thereby increasing the amount of carriers in the Γ-valley and the amount of light emission achievable to the point where lasers are possible [76]. Phosphorus doping of Ge with concentrations over 10^{19} cm^{-3} using a GaP decomposition source, similar to that used in this work, has been reported previously [77], but not yet for GeSn by the MBE growth method. Donor concentrations over 10^{20} cm^{-3} using the GaP source have also been reported for Si [78], [79] and SiGe[80]. In addition, P has

been reported to have a sticking coefficient near unity at the low temperatures typically used for growing GeSn (100-200°C) via MBE, which is ideal for having high dopant incorporation [77]. The in-situ phosphorous doping of GeSn alloys has been reported previously for CVD grown films [81], [82], but not yet by MBE.

The p-type doping of GeSn above 10^{20} cm^{-3} is important for uniaxially strained p-type Ge MOSFETs, where a GeSn heteroepitaxial stressor layer would be incorporated into the source and drain regions to strain a Ge channel [83]. In-situ doping of GeSn with Gallium acceptors by MBE has been reported with active concentrations up to $1.2*10^{20}$ cm^{-3} for 8.5% Sn layers, as measured by micro 4-point probe, and by IR spectroscopic ellipsometry [84], and up to $5.5*10^{19}$ cm^{-3} active Ga for 7.8% Sn layers as measured by micro 4-point probe [83].

Other in-situ dopants that have been studied for GeSn alloys include Boron acceptors for p-type doping in both MBE [85] and CVD [81] layers, while antimony (Sb) has been used via MBE for n-type doping [86].

5.3 Sample Preparation

The GeSn alloys were grown using a solid source multi-chamber Molecular Beam Epitaxy system (Veeco/ EPI model 620), equipped with Knudsen effusion cells for both Ge and Sn, as described elsewhere [87]. The growth chamber was pumped by a closed-loop cryo-pump (CTI Cryogenics CT- 8F) and an ion pump (Varian 400l/s) to typical base pressures of $4*10^{-8}$ Pa. The Ge and Sn effusion cells contained triple zone-refined intrinsic polycrystalline Ge, and metallic Sn (of 6-N purity from United Mineral and Chemical Corporation), respectively in pyrolytic boron nitride (pBN) crucibles. The Ga source was high purity Ga (7-N) in a pBN crucible heated in a dual zone effusion cell to help prevent droplet spitting. The P donors were evaporated from

a GaP decomposition source, which relies on a specially designed pBN baffle to trap the Ga, while the P (mainly P_2), which has a much higher vapor pressure, escapes through a small hole in the top of the baffle. The GaP decomposition source produces a fairly pure P_2 beam with a P_2/P_4 ratio of 150 [78]

The substrates were polished 3 in. diameter, un-doped Ge (001) wafers, of nominal 40 Ω cm resistivity, which were measured as discussed below. The Ge wafer pre-cleaning steps are based on a recipe described by Okumura, et. al. [88], and consisted of an initial oxide etch in HF, followed by 3 cycles of growing GeO_2 in concentrated (35%) H_2O_2, followed by etching in an HCl solution. The cleaning recipe is completed by an oxide growth step performed in an ammonium hydroxide/ peroxide solution. Any remaining surface contaminations were subsequently removed from the substrates by ultrahigh vacuum degassing at 250 ^oC for an extended (overnight) period, and then flashing to 850 ^oC for 5 min. The MBE chamber pressure was less than $1*10^{-7}$ Pa throughout the growth.

Prior to the GeSn alloy growth, an initial buffer layer of Ge was grown at 420 ^oC to produce a uniform, flat surface. The subsequent GeSn layers were grown at a reduced temperature of 150 ^oC to avoid Sn segregation. For the doping studies reported here, each sample consisted of three doped GeSn layers separated by un-doped GeSn buffers. The Ge and Sn cell temperatures were held constant during growth, and the GaP and Ga cell temperatures were varied to change the n- and p-type doping concentrations, respectively. Two multilayer samples were used in this study; one with differing levels of Ga doping (sample 1), and the other with differing levels of P doping (sample 2).

5.4 Dopant Measurements

High resolution X-Ray diffraction (HR-XRD) was performed with ω-2θ coupled scans and reciprocal space maps (RSM) using a Philips/Panalytical X'Pert MRD as described elsewhere [87]. The GeSn layer compositions were determined via high resolution reciprocal space maps in a <224> alignment following the procedure of [89], while assuming that the lattice constant and Poisson's ratio of the GeSn layers can be interpolated following Vegard's Law [87]. Both samples shown in this work were found to be fully strained against the Ge substrate, with the relaxation measured by RSM to be ≤1% for all layers. The lack of relaxation was surprising for these GeSn samples with Sn concentrations near 8% and thickness over 300 nm, as this is much greater than the classical critical thickness for GeSn on Ge [22], as shown in Figure 1.4. The GeSn (224) peak height for the P doped sample was about three times higher than for the Ga doped sample, and the peak was sharper as well. The Ga doped sample had a (224) FWHM in the Qx direction 70% wider than the P doped sample, and in the Qy direction it was 30% wider than the P doped sample. As all growth conditions were the same except for the dopant species, this would seem to indicate a slightly worse crystal with Ga doping than P doping.

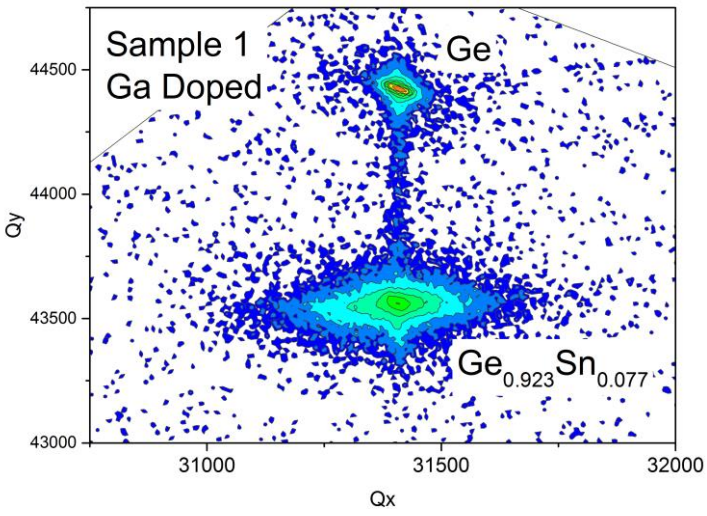

Figure 5.1: XRD RSM of sample 1 with Ga doping. XRD shows a completely strained GeSn layer on a Ge substrate.

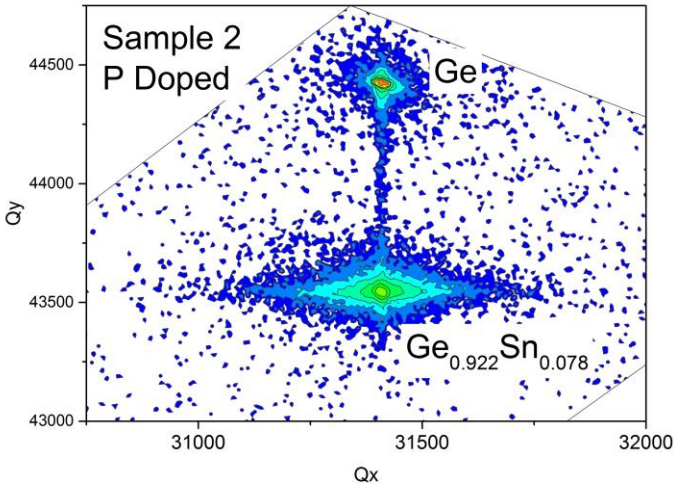

Figure 5.2: XRD RSM of sample 2 with P doping. XRD shows a completely strained GeSn layer on a Ge substrate.

Secondary Ion Mass Spectroscopy (SIMS) measurements of the doping concentrations were performed by Evans Analytical Group [90]. An O_2^+-beam was used for Sample 1 with Ga, and a Cs^+-beam was used for Sample 2 with P. The Sn concentration was calibrated for SIMS by using a GeSn standard calibrated by Rutherford Backscattering Spectrometry (RBS).

Figures 5.3 and 5.5 show the SIMS depth profiles for the Ga doped and P doped samples, respectively. In Figure 5.3, the three Ga cell temperature steps of 650, 675, and 700 ^oC produced Ga concentrations of $1*10^{19}$ cm^{-3}, $3*10^{19}$ cm^{-3} and $7*10^{19}$ cm^{-3}, respectively. The Ga profile exhibited a characteristic doping turn-on effect; the SIMS incorporation was seen to spike upward upon the moment of Ga turn on, then to decrease, and subsequently to increase again before stabilizing at a final value. This transient response has been seen before in the Ga doping of Ge [91], where it was attributed to Ga segregation at an epi interface, which may occur here at the doped/intrinsic epi interface. It could also be a transient due to a heat fluctuation when the shutters are opened or closed. The *turn-off* of the doping, however, was characteristically sharp. The Ga background in the un-doped spacer layers was near $1*10^{18}$ cm^{-3}, which could be in part due to SIMS drive-in effects, in which the etching ion beam contributes signals from the trench sidewalls and masks the true signal from the un-doped regions at the bottom of the etched trench. The SIMS measurement yielded a calibrated Sn concentration of about 7.8%, which agreed well with the XRD RSM result of 7.7%. The Sn content was flat versus depth, except for slight peaks at the GeSn/ Ge interface at a depth around 325nm, and the Ge buffer/ Ge growth interface at around 375nm.

In Figure 5.5, the three GaP cell temperatures steps of 740, 760, and 792ºC yielded P concentrations of $1*10^{19}$ cm^{-3}, $2.1*10^{19}$ cm^{-3}, and $9*10^{19}$ cm^{-3}. Sharp doping turn-on and turn-off was observed in the SIMS profiles of P, corresponding to opening and closing the cell shutter. A slight slope, downward towards the surface, however, can be seen in each of the P doping profiles in Figure 5.5. Sample 2 had a P background concentration between doped layers of around $2*10^{17}$ cm^{-3}, which was lower than the apparent background doping in the Ga doped sample. A small P peak can be seen at the substrate epi interface at 375nm, but there is no corresponding Sn peak at that position, unlike in Figure 5.3. The SIMS measurement of this P-doped sample yielded a Sn concentration of 7.4%, agreeing well with XRD results of 7.8%.

To determine if the dopants were electrically active, Spreading Resistance Profiling (SRP) was performed by Solecon Laboratories with a two-probe measurement system [92]. The sample was first beveled and the spreading resistance was measured across the bevel, which provides a depth profile. The resistivity versus depth is then extracted from the spreading resistance depth profile. Figures 5.4 and 5.6 show the SRP results for the Ga doped and the P doped samples, respectively. Additionally, hot-point probe analysis was done in conjunction with SRP, and yielded p-type conductivity for the substrate, p-type for the Ga doped layers, and n-type for the P doped layers (including spacer layers), as expected. SRP analysis, in general, showed similar, but less abruptly defined profiles than the SIMS, which may be an artifact of the measurement resolution. One noticeable feature is the large resistance peak centered at 325nm in Figure 5.6, at the n-GeSn / Ge interface, which was attributed to the high resistance of the space charge region between the n-type GeSn layers and the nominally p-type Ge substrate.

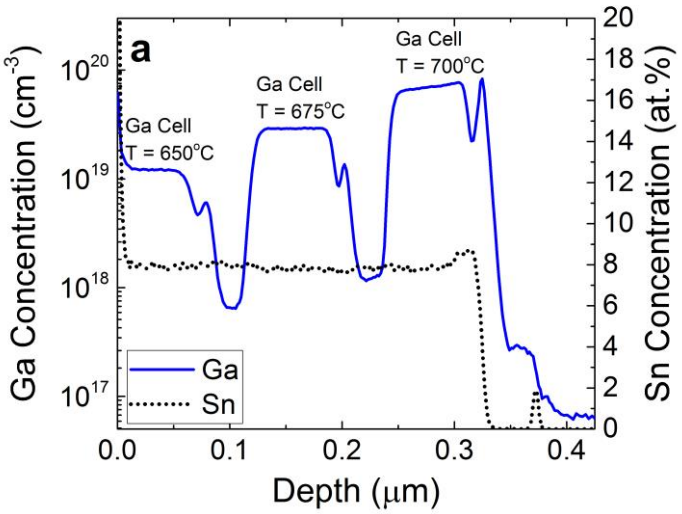

Figure 5.3: SIMS composition profile of GeSn sample 1, a series of Ga doped steps. The temperatures of the Ga cell during growth are noted.

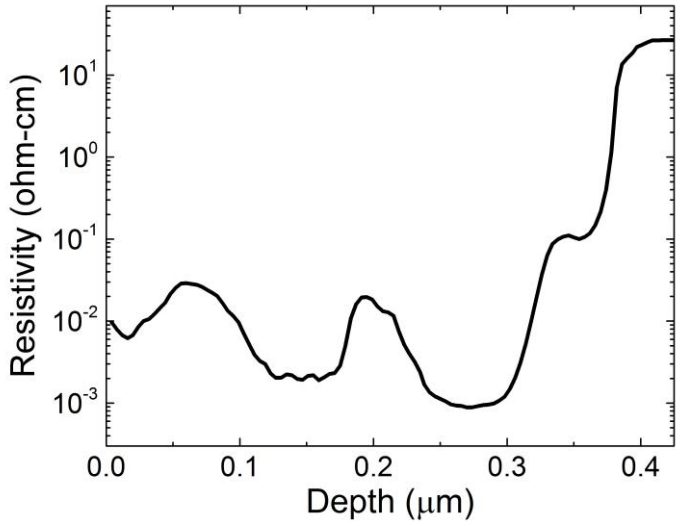

Figure 5.4: Spreading resistance (SRP) analysis of sample 1, showing the resistivity profile of the film.

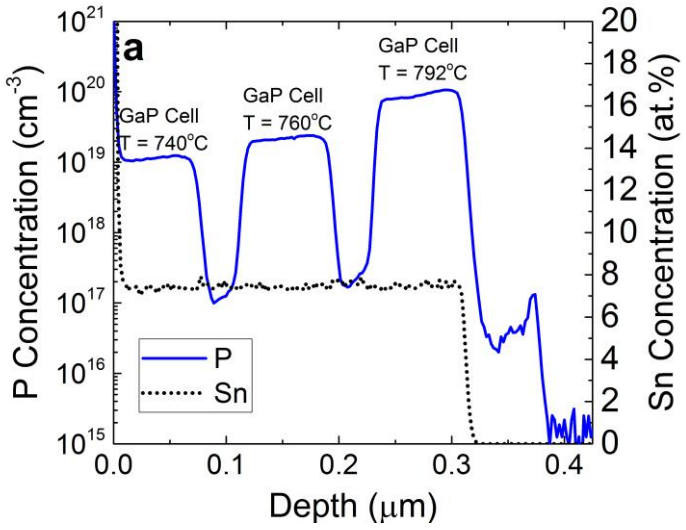

Figure 5.5: SIMS measurement profile of GeSn sample 2, a series of P doped steps. The temperatures of the GaP cell during growth are noted.

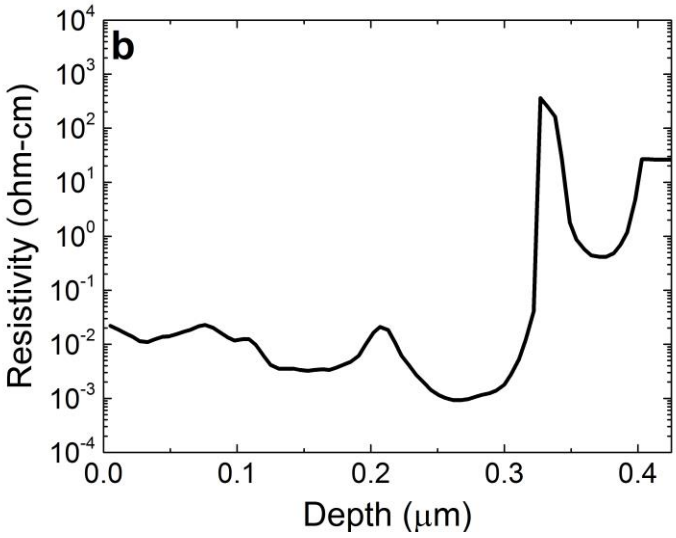

Figure 5.6: Spreading resistance (SRP) analysis of sample 2, showing the resistivity profile of the film.

5.4.1 Doped GeSn Mobility Extraction

The resistivity depends on the doping concentration according to,

$$\rho = \frac{1}{q(n\mu_e + p\mu_h)} \tag{5.1}$$

where q is the magnitude of electronic charge, n and p are the active concentrations of electrons and holes, while μ_e and μ_h are the mobility of electrons and holes, respectively. The mobility of a semiconductor is,

$$\mu = \frac{q\tau}{m^*} \tag{5.2}$$

where τ is the mean scattering time and m^* is the effective mass of the carrier. Hence, for the dependence of resistivity on doping concentration to remain the same between Ge and GeSn, the mobility of the materials would have to be the same which, in general, is not expected.

In GeSn alloys, there are additional effects on the scattering time and the effective mass that could either increase or decrease the mobility relative to Ge. GeSn is an alloy, and thus will suffer from additional scattering from an inhomogeneous lattice, lowering mobility [93]. In addition, due to the compressively strained nature of these films, the valence band is expected to split, with the light-hole band dropping below the heavy hole band [16]. The higher effective mass of the heavy-hole band would cause a lower mobility for holes. On the other hand, due to a progressively more direct band gap structure with the addition of Sn, the effective mass of electrons is expected to decrease and the mobility of GeSn is expected to increase [93], [94]. Pseudomorphic layers of GeSn on Ge substrates, however, are not expected to have a direct bandgap [15], implying that for the films studied here, the lowest conduction band remains at the L-valley with its relatively larger effective mass, and there is no corresponding mobility increase. As a point of comparison, p-type GeSn, doped with Ga and strained to Ge substrates, has been previously reported to have hole mobilities about half of that in similarly doped but relaxed Ge [83].

In order to estimate the mobility of GeSn, the SIMS atomic concentrations from Figures 5.3 and 5.5 were assumed and were used with the resistivity values from Figures 5.4 and 5.6 in Equation 5.1 to calculate the GeSn mobility, shown in Figure 5.7. The extracted GeSn mobility is shown along with literature results for the mobility of n-type and p-type Ge [95]. Increased doping concentration leads to increased ionized impurity scattering, in turn decreasing the mobility, clearly seen in the Ge curves in which the mobility halves as the dopant concentration increases from $1*10^{19}$ cm^{-3} to $1*10^{20}$ cm^{-3}. In comparison, the calculated mobility values for GeSn are almost flat with doping concentration, with a value near 100 $cm^2/$ (V s). The mobility for both Ga doped and P doped GeSn slightly peaks at concentrations near 2-3 $*10^{19}$ cm^{-3} for both samples, which could be due to experimental error. The n-type, phosphorous doped, GeSn appears to have slightly lower mobility than that of Ga doped GeSn. The fact that GeSn mobility is flat across the doping concentrations measured may indicate that the mobility of the material is affected not only by ionized impurity scattering, but dominated by some other mechanism such as alloy scattering.

Rearranging Equation 7.2 allows for the calculation of the scattering time from mobility. In pseudomorphic strained GeSn, the band structure is assumed here to be indirect, with electrons in the L valley, as for unalloyed Ge. Assuming the same effective masses for electrons (0.12 * electron mass) and holes (0.34 * electron mass) as in bulk Ge, leads to a scattering time of approximately 20 fs for holes in p-type GeSn and approximately 5 fs for electrons in n-type GeSn. This scattering time information may be useful for a better understanding of the carrier transport in GeSn alloys. The mobility and scattering time extracted here are likely lower bounds, however, as the dopants were assumed to be 100% electrically active for the

calculations and a decrease in activation would cause an increase in both mobility and scattering time.

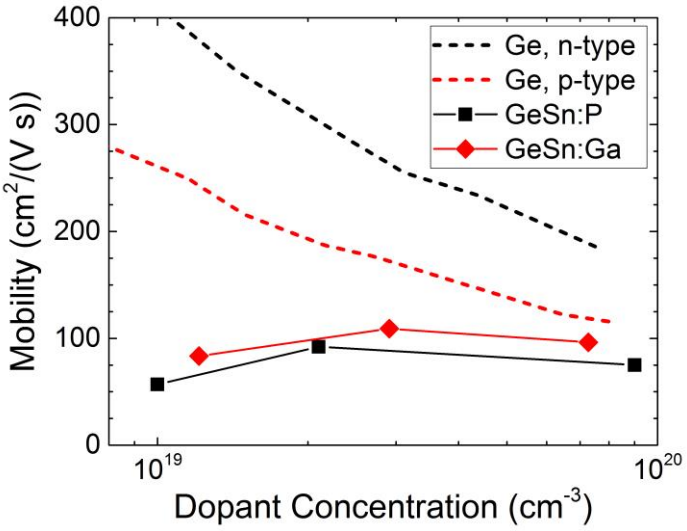

Figure 5.7: Calculated mobility of GeSn versus dopant concentration, assuming 100% activation of dopant atomic concentrations from SIMS, and the resistivity values measured from SRP. The mobility of n-type and p-type Ge are shown by the black and red dashed lines respectively from [95].

5.5 Growth Temperature Characterization

For lower Sn concentrations, a larger growth window of substrate temperatures exists than for higher Sn concentrations, and lower Sn films can be grown at higher temperatures without problem. The questions are, then, what changes occur in the film structure throughout the temperature window and what is the ideal temperature for film growth? As previously mentioned, at the high temperature end of the growth window, the Sn segregates. At the low temperature limit, the film can become amorphous due to extremely limited lateral surface diffusion rate during epitaxy. In the middle temperature regime, there are other effects on film quality. For instance,

Nakatsuka et al. found that at these lower growth temperatures, the film was unintentionally doped p-type, with carrier concentrations near 10^{18} cm^{-3}, which they attributed to vacancies due to low temperature growth [96]. In addition, for Si and SiGe films, lower growth temperatures lead to higher O content in the films [32], although this effect has not been measured in the GeSn system.

In order to investigate what effects the substrate growth temperature would have on the film, a GeSn film was grown where the substrate temperature was varied during growth. The same wafer cleaning and growth procedures outlined in Section 5.3 were followed. SIMS as well as SRP was performed on this film, and are shown along with the actual substrate temperature during growth in Figure 5.8 taken from the MBE software AMBER. The film was grown on an undoped Ge (100) wafer, and included a Ge buffer layer grown at 420 ^{o}C. After the Ge buffer layer, all cell shutters were closed and the substrate temperature was dropped to 175 ^{o}C. At 175 ^{o}C, the Ge and Sn shutters were opened and remained open throughout the temperature changes shown in Figure 5.8, until the growth was done. The film growth rate was targeted at 0.76 nm/min, with a Sn concentration of 8%. The substrate temperature was varied from a high of 250 ^{o}C to a low of 125 ^{o}C.

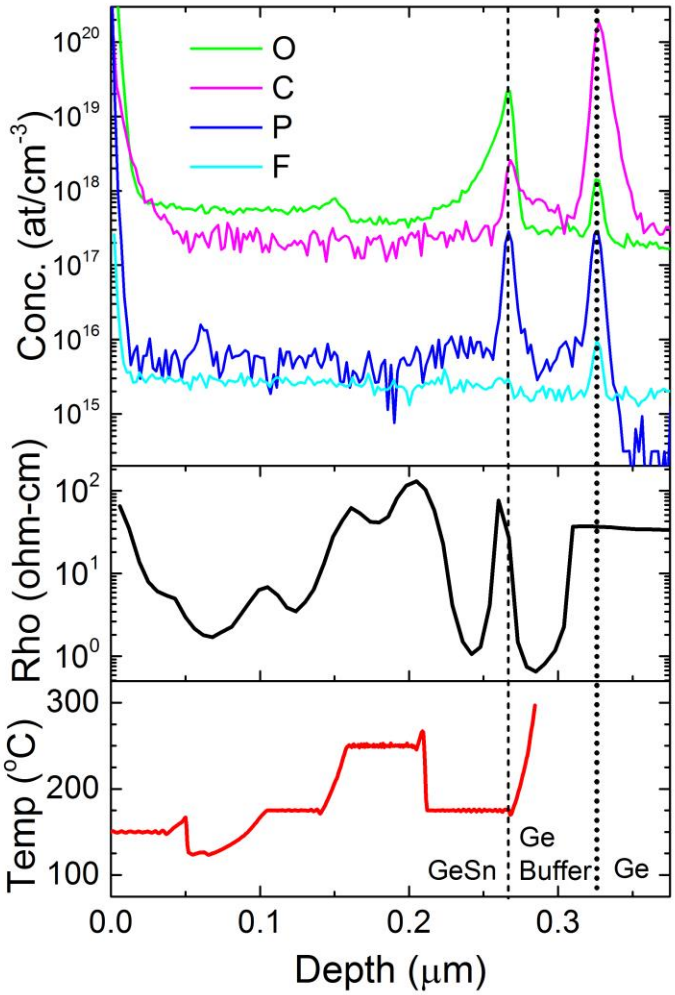

Figure 5.8: Characterization of GeSn impurities versus growth temperature. The top plot shows atomic concentration of film contaminants film as measured by SIMS. The middle plot shows the resistivity of the film as measured by SRP. The bottom plot shows the actual temperature profile of the film as measured by the AMBER software that was used for MBE system control. The data for the substrate temperature was measured as a function of time, which is multiplied by the growth rate to get depth. During the Ge buffer layer, the substrate temperature was 420 °C; this is not properly captured in the temperature plot from AMBER because the shutters were closed and re-opened at the end of the buffer. The GeSn layer is approximately 260 nm thick, and the Ge buffer is approximately 50 nm. The locations of the layer interfaces are designated by dashed lines, and the alloy content of the films are labeled on the depth-axis.

From the SIMS shown in Figure 5.8, the two layer interfaces can be seen by their characteristic peaks in O and C contents. Throughout the layers, the O and C content are flat, and show little variation with growth temperature. There is a slight peak in O at a depth of approximately 150 nm, which corresponds to a point in the growth where the substrate temperature was being decreased from 225^{o}C to 175^{o}C. It is unknown what the cause of this peak is. The O signal does appear to increase slightly ($\approx$ 1-2 *10^{18} cm^{-3}) in the top half of the film, which is grown at lower temperatures. The growth that was performed just prior to this film was the P doping test structure of Section 5.2, so the P content of the current sample was measured to see if there was any residual contamination. The SIMS does show P peaks at the Ge/Ge buffer and Ge buffer/ GeSn interfaces, but in the layer the concentration is at the SIMS background and does not vary with substrate temperature. F was also measured, and it showed a slight peak at the Ge/Ge buffer interface, for reasons that are unclear.

The resistivity of the film was extracted with SRP as described in Section 5.4. It showed, in general, a higher resistivity for a higher growth temperature. The resistivity range spans from about 1 ohm-cm to approximately 100 ohm-cm. A lower growth temperature leading to a lower resistivity film would seem to be consistent with the theory that low temperature growth introduces some sort of defect that dopes the film [96]. The highest resistivity measured in GeSn is higher than that in the Ge wafer, perhaps due to a decreased mobility in the GeSn region. The lowest resistivity was measured was in the Ge buffer layer, the cause for this is unknown.

There are also a few spikes in the resistivity versus depth. The largest is a spike at the Ge/ Ge buffer interface, possibly due to interface contamination, or to a space-

charge region depleted of charge carriers, and there are also small spikes at the points in the film where the substrate temperature was changed. The spikes happen regardless of whether the substrate temperature was increased or decreased.

5.6 Growth of High Tin Content Alloys and Sn segregation

The growth window for successful GeSn growth is at temperatures much lower than traditional group IV epitaxy. Most films in this work focused on the higher Sn concentrations, and this section outlines what conditions were necessary for the epitaxy of high Sn content films. Shown in Figure 5.9 are photographs of a wafer surface obtained in the course of a growth optimization study. The left picture Figure 5.9 shows a uniformly hazy wafer; the growth conditions were T_{sub} = 150 ^{o}C and growth rate = 0.52 nm/min. The middle picture shows a specular wafer with segregation spots; the grown conditions were T_{sub} = 120 ^{o}C and growth rate = 0.52 nm/min. The right picture is a completely specular wafer; the grown conditions were T_{sub} = 120 ^{o}C and growth rate = 0.79 nm/min. Growing faster, and at lower temperature, has a profound effect on improving the film morphology. At higher temperatures, the film is very hazy because the Sn is almost completely segregated. At lower temperatures, and also lower growth rates, the surface of the film is spotty with dispersed Sn segregate spots strewn randomly across the wafers surface. An XRD RSM plot focused on one of these spots can be seen in Figure 5.10. The RSM shows a peak of GeSn with 4% Sn strained to the Ge substrate, which is attributed to the removal of Sn from the GeSn alloy. The spots then are assumed to be the segregated Sn atoms. There is also a residual peak of 14.6% Sn in GeSn; it's unknown whether this material exists under the Sn segregated region, or it's due to the width of the X-ray beam on the wafer surface being wider than the spots. Figure 5.10 is a typical

RSM plot for segregated Sn, where a small amount of Sn is left residual in the Ge film, usually at levels still above the solubility of Sn in Ge as seen in 1.3.

Close up micrographs of one of the segregation spots can be seen in Figures 5.11 and 5.12 using dark field microscopy. The segregated Sn appears to segregate outward, originating from one centralized point, which can be seen most clearly in Figure 5.12. The growth substrate was a (100) Ge wafer, and the Sn globs can be seen forming along the (100) and (110) directions. The Sn globs appear to leave trails behind them, as if these streaks were the result of motion. An AFM micrograph of such a trail is shown in Figure 5.13. The aspect ratio of these segregates is quite large, for films only 50 – 100 nm thick the segregate patterns can stretch multiple mm wide.

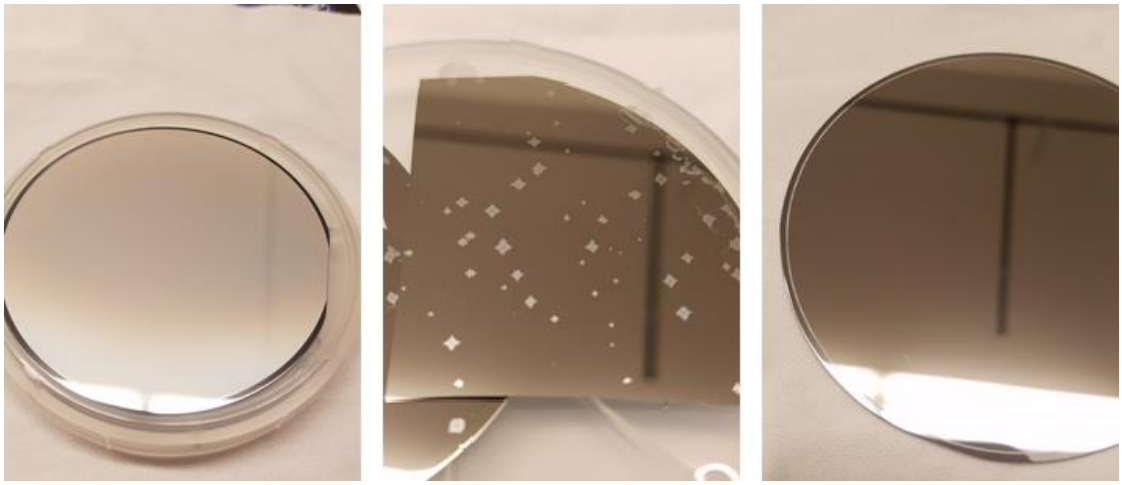

Figure 5.9: Evolution of epitaxy for 12.5% Sn concentration series, showing progressively better epitaxy conditions moving from the left picture (hazy), to the middle picture (spotted), to the right (specular).

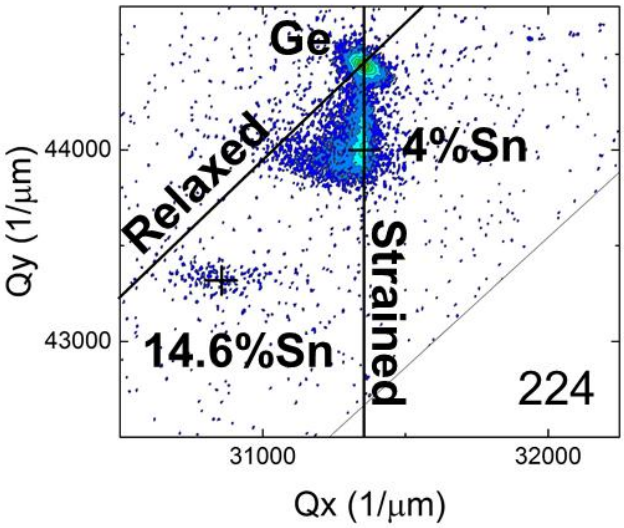

Figure 5.10: XRD 224 RSM plot of Sn segregation spot for a nominally 14.6% Sn sample on a Ge substrate. The x-ray beam has been focused onto the Sn segregate spot.

Figure 5.11: 10x magnified dark field microscope image of the edge of a Sn segregation spot. Sn globs can be seen on the surface. It appears that the Sn globs travel across the surface along the (100) and (110) directions.

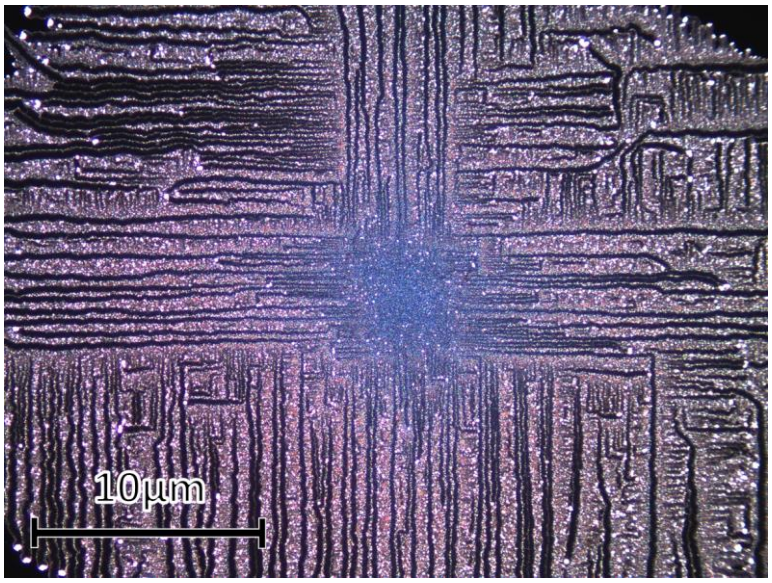

Figure 5.12: 10x magnified dark field microscope image of the center of a larger Sn segregation spot, showing "trails" extending along the (100) directions.

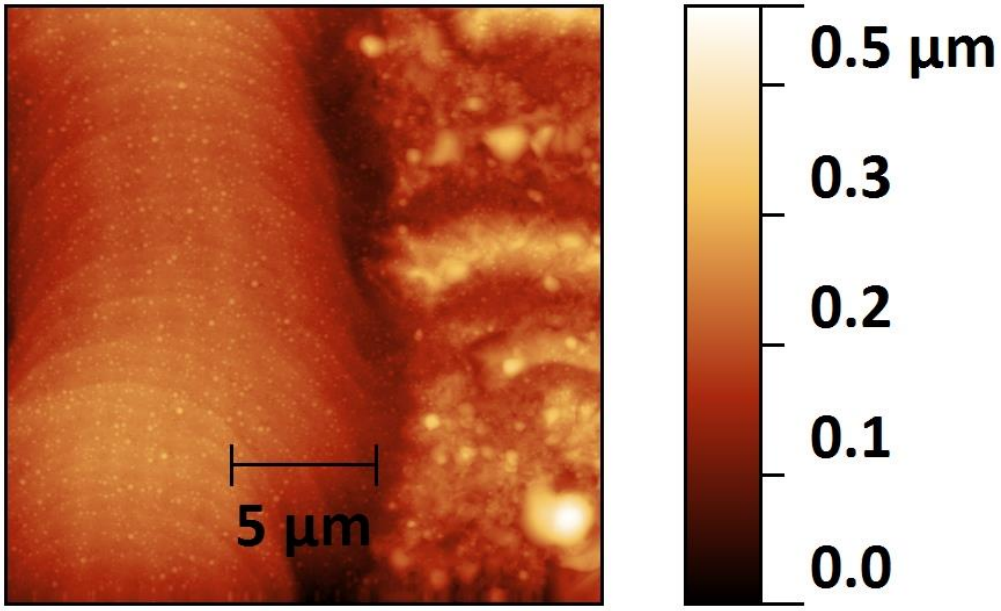

Figure 5.13: An AFM micrograph of the Sn segregate trail left along the surface as a Sn globule appears to travel outward.

Growing at lower growth temperatures and faster growth rates is needed to achieve higher Sn content films, but these variables have limits. The substrate temperature is limited by the radiation from the effusion cells heating the wafer. Currently the minimum temperature that can be stably reached throughout a growth is somewhere around 100 ^{o}C. Frequently growths are started at lower temperatures, 88 ^{o}C for example, but upon opening the shutters of hot effusion cells, the substrate rises above 100 ^{o}C within 20 minutes. The growth rate is largely dominated by the Ge cell flux for all films that are studied in this work which, while having relatively high Sn content, are still mostly Ge. The Ge cell temperature is routinely kept at 1215 ^{o}C, which is fairly high for the pyrolytic boron nitride (PBN) crucible. At high temperatures the pBN will begin to breakdown and B and N could contaminate the film. This effect hasn't been studied extensively in the University of Delaware MBE system, it could be that some additional temperature headroom exists for increasing the Ge flux rate without contaminating the source material.

The highest Sn content achieved in the MBE at the University of Delaware to date is approximately 18%. Films with this concentration have been achieved on Ge substrates up to 100 nm thick. Figure 5.14 shows an XRD RSM of the first sample grown at the University of Delaware with a Sn concentration of approximately 18%. The resulting film structure is mostly relaxed, with a wide spread in reciprocal space indicating that some of the film is residually strained. Relaxation in the middle of the film could be the result of the substrate temperature during the growth which, as mentioned above, shifted from 88 ^{o}C to >100 ^{o}C over the course of the growth.

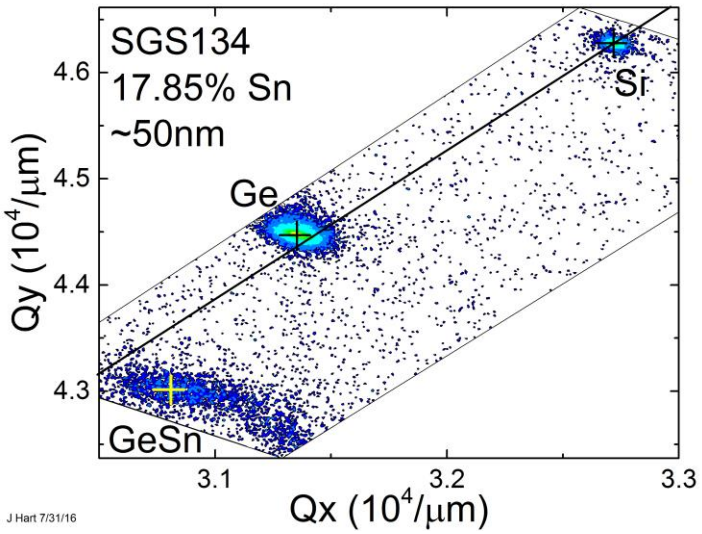

Figure 5.14: XRD RSM of SGS134, a 17.85% Sn film grown on a Ge virtual substrate on a Si wafer.

5.7 Growth of Ge Virtual Substrates on Si (100) wafers

Growing on Si substrates rather than Ge substrates presents several advantages: lower cost, increased industrial relevance, and an easier and well defined cleaning procedure (as described in Section 2.3.5). The disadvantages are that the Ge virtual substrates have a much higher amount of threading defect dislocations (TDD) due the metamorphic growth and are rougher. For relaxed GeSn films, as is discussed in Chapter 8 for photodetectors, the TDD problem isn't so large, as relaxing GeSn films by exceeding the critical thickness will introduce more threading defects, likely eliminating much of the advantage of growing on a Ge wafer.

The growth of Ge virtual substrates used in this work is similar to that used in other group IV MBE work [97]. It starts with a low temperature Ge growth to insure a smooth film, proceeds to a relatively higher temperature annealing step, and is finished by a high temperature Ge growth step. In this work, the low temperature step

was grown at 330 ^{o}C and was 200 nm thick. The anneal step was for 30 min at 850^{o}C. The high temperature growth step was at 600^{o}C and was 100 nm thick. This procedure was then repeated and resulted in a virtual substrate that was 600nm thick. The resulting Ge film had an (004) ω FWHM of 347.7 arc seconds and a surface roughness of approximately 2-3 nm RMS, which was considered to be acceptable for GeSn epitaxy.

5.8 Conclusion

We have demonstrated the doping of GeSn alloys with both Ga for p-type conductivity and P for n-type, performed in-situ during MBE growth. The GaP decomposition source and the Ga source were both able to achieve high carrier concentrations (>7*10^{19} cm^{-3}). Reasonably sharp and well behaved doping profiles were observed utilizing SIMS and SRP measurements. The electron and hole carrier mobilities of 8% GeSn was extracted, finding a value of 100 cm^{2}/ (V s) that is unchanged across the dopant concentrations measured. Scattering times extracted from these mobilities are on the order of femtoseconds.

The effect of the substrate temperature on the resistivity and impurities of 8% GeSn was investigated, revealing that higher substrate temperatures during growth lead to an increase in resistivity. By changing the temperature from 125 ^{o}C to 250 ^{o}C, the resistivity was increased by 2 orders of magnitude, from 1 ohm-cm to 100 ohm-cm. This result on growth effects could have consequences in any device structures that rely on a high resistivity layer, including, among others, photoconductive and PiN detectors.

The growth temperature window for high Sn content films was described, which needs a lower substrate temperature and a higher growth rate for full Sn

incorporation with no segregate spots. Patterns of segregated Sn that appear on the substrate the boundaries of this growth temperature window were characterized with XRD, dark field microscopy, and AFM.

Finally, the growth recipe for producing relatively high quality Ge virtual substrates grown in MBE was presented.

Chapter 6

FOURIER TRANSFORM INFRARED SPECTROSCOPY FOR SEMICONDUCTOR DEVICE CHARACTERIZATION

6.1 Introduction

Fourier Transform Infrared Spectrometry (FTIR) is a versatile technique that has been extensively applied to measure transmission, reflection, absorption, and emission spectra. These measurements are particularly important for classifying semiconductor properties such as light absorption and light emission. The FTIR spectrometer used for measurements in this dissertation was a Thermo Fisher Scientific iS50r which employs a two-beam interferometer based on Michelson's original design [98]. FTIR principles, custom modifications, and advanced measurement techniques are considered in this chapter.

6.2 Interferometer Theory

An interferometer is a device that introduces an optical path difference between two beams of light that originate from the same source. Figure 6.1 illustrates the basic components of a typical interferometer. A radiation source is first collimated by a parabolic mirror. The single collimated beam then travels to the beam splitter. As the name suggests, the beam splitter splits the incoming light, sending part of it to a moving mirror while the remaining part of the beam is reflected to a fixed mirror. After each beam reflects from their respective mirrors, the beams recombine and are directed to the detector. Because of the wave nature of light, the optical path length

difference causes the two beams to interfere when they recombine. The variation in intensity of the output beam can then be measured by a detector as a function of path difference. In reference to the object labels in Figure 6.1, the optical path difference, or retardation, δ, is given by the length 2*(OM-OF).

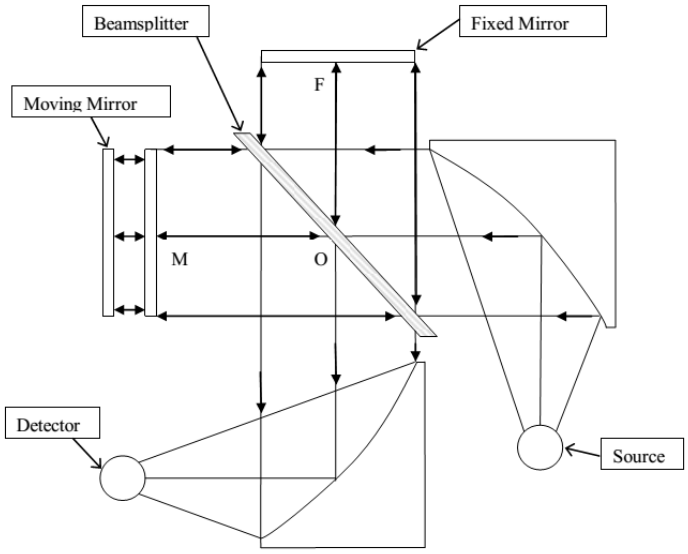

Figure 6.1: An overview of a basic Michelson interferometer showing the light source, the beam splitter, the fixed and moving mirrors, and the detector.

The signal at the detector is due then to the interference between the two optical path lengths, and referred to as an interferogram. The interferogram intensity, $I(\delta)$, can be described as a function of optical path difference between the beams, δ, for a polychromatic source as,

$$I(\delta) = \int_{-\infty}^{\infty} B(\sigma) \cos(2\pi\sigma\delta)\, d\sigma \qquad (6.1)$$

Where $B(\sigma)$ is the spectral intensity as a function of wavenumber, σ (cm^{-1}). For a monochromatic source, $I(\delta)$ is a sinusoidal wave while for a broadband source $I(\delta)$ is a superposition of sinusoidal waves at all wave numbers σ. At zero path length difference (ZPD), all the sinusoidal waves interfere constructively, producing a "center burst" in the interferogram. Fourier transformation of $I(\delta)$ then gives the ***single-beam*** spectrum, as shown in Equation 6.2.

$$B(\sigma) = \int_{-\infty}^{\infty} I(\delta)\cos(2\pi\sigma\delta)\, d\delta \tag{6.2}$$

In practice, a Discrete Fourier Transform (DFT) is used as a digital approximation of the continuous Fourier series. With this, Equation 6.2 becomes,

$$B(k \cdot \Delta\sigma) = \sum_{n=0}^{N-1} I(n \cdot \Delta\delta)\cos(\frac{2\pi kn}{N}) \tag{6.3}$$

Where the continuous variables of wavenumber σ, and optical retardation δ, have been replaced by the discrete variable k and index n, respectively. The summation is then over the total number of data points N.

6.3 iS50r Tool Description and Possible Beam-Paths

The Thermo Fisher Scientific is a versatile tool, capable of many different types of measurements. This section outlines the many different parts of the iS50r and describes the necessary setups needed for semiconductor tests done at the University of Delaware. The FTIR Omnic software is responsible for switching the internal FTIR mechanisms, while the external optical bench is configured manually.

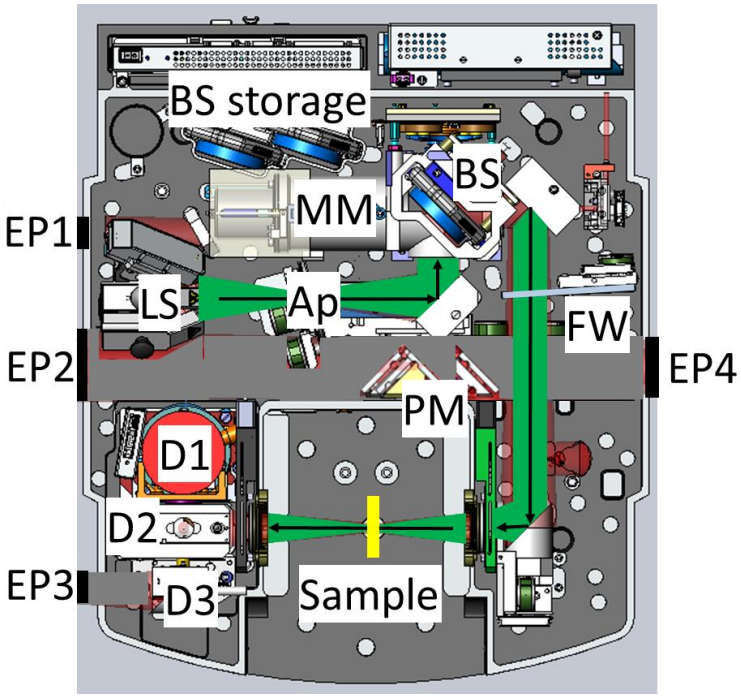

Figure 6.2: FTIR beam path setup for traditional transmission measurements. The components of the tool have been labeled, with explanations given in the Table

Table 6.1: Description of iS50r components, as labeled in Figure 6.2

Label	Description
LS	Light sources for the FTIR. Adjustable in Omnic. Choices include the IR-Globar, Visible-Xe lamp, and external light source through the focused external mirror
Ap	Beam aperture. Adjustable in Omnic
BS	Beam splitter. The system will automatically detect the inserted beam splitter
BS storage	Beam splitter storage for up to two beam splitters
MM	Moving mirror. This moves back and forth to create the light interference and result in an interferogram

FW	Filter wheel. Has different settings for filtering the light, including reducing the optical power. Adjustable in Omnic
PM	Passport mirror. Adjustable in Omnic. Can send collimated light to EP2 (as shown in Figure 6.3), collimated light to EP4 (as shown in Figure 6.6), or let light pass through (as shown in Figures 6.4 and 6.5)
Sample	Sample compartment. Samples are put in the beam path here for transmission measurements
D1	Detector position 1. All detectors fit into this slot, including: LN2 cooled MCT, Si, InGaAs, TEC cooled DTGS, and DTGS with a PE window. The system will automatically detect which light detector is inserted
D2	Detector position 2. This is a permanent DTGS detector with a KBr beam splitter mounted above the rotating mirror. Used for default settings and is useful for Mid-IR transmission experiments
D3	Detector position 3. This position accepts new style, thin profile, detectors, including the DTGS with a PE window. This position also accepts a 90^{o} gold plated mirror to send the light signal to EP3
EP1	Beam entry point 1. Used for external collimated light beams to be used as a light source. See Figures 6.4 and 6.5 for example setups
EP2	Beam exit point 2. Used to extract a collimated light beam from the internal FTIR light source for external detectors (see Figure 6.3), or to receive a collimated light beam from an external detector (Figure 6.4).
EP3	Beam exit point 3. Used to send light to the external Si bolometer. See Figure 6.5 for an example setup
EP4	Beam exit point 4. Used to send light to the external microscope. See Figure 6.6 for an example setup

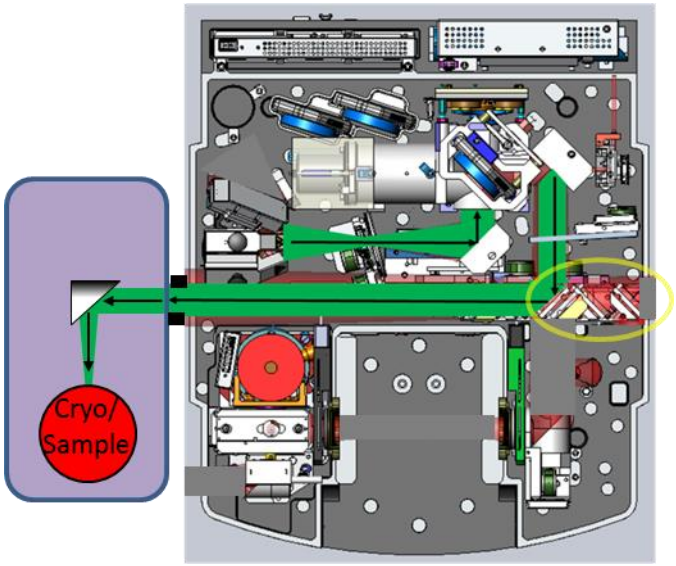

Figure 6.3: FTIR setup for measuring external detectors including photoconductors and photodiodes. This setup uses the FTIR internal light source. The passport mirror, circled in yellow, reflects a collimated beam to the sample container, where it hits a focusing mirror before reaching the sample in the cryo-cold finger.

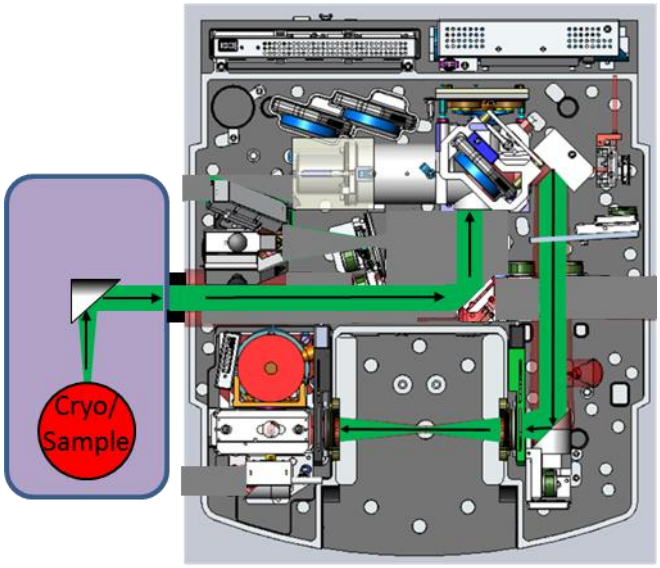

Figure 6.4: FTIR setup for measuring external emitters using the FTIR internal detectors. For this setup, a collimated external source is needed (or 90^{o} collimating mirror in the N2 purge box) to send collimated light into the FTIR. This is the setup needed for measuring GeSn light emitters with internal detectors.

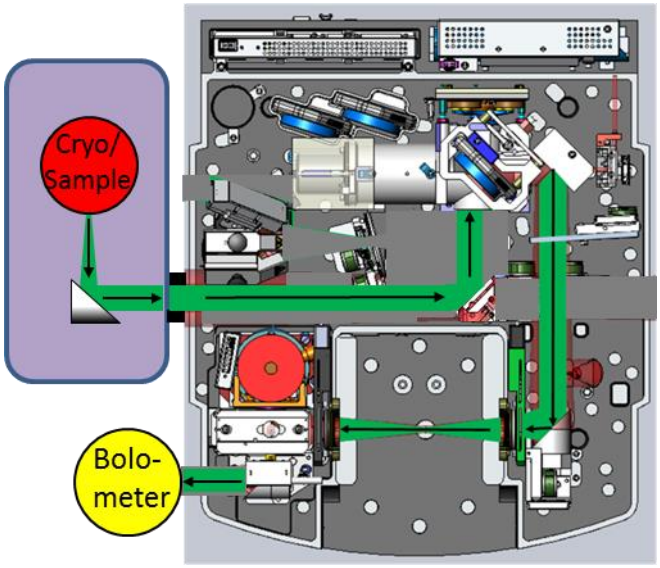

Figure 6.5: FTIR setup for measuring external emitters with the external Si bolometer. This is the setup needed for measuring THz emitters. To use this setup for THz measurements, the ideal material for the 90^{o} collimating mirror is gold plated.

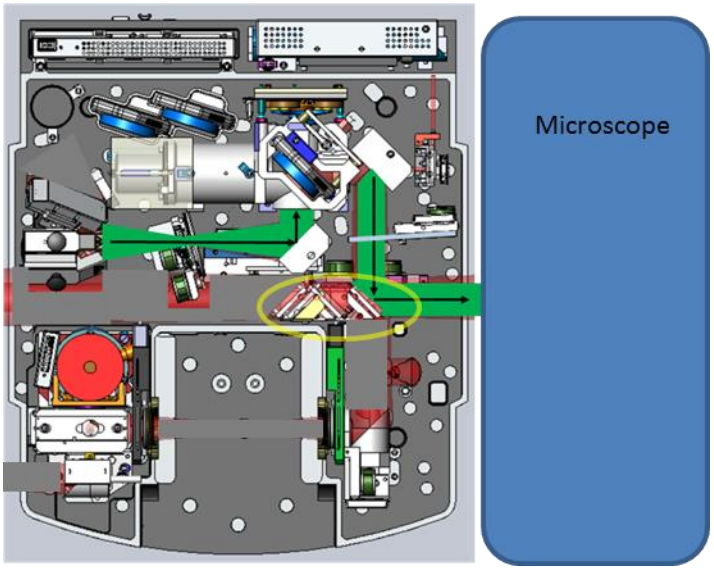

Figure 6.6: FTIR setup for measuring using the external microscope. In this configuration, the passport mirror, circled in yellow, needs to be configured in Omnic.

6.3.1 Custom Cryostat Stage

It is often desirable to cool samples during testing. This was done in a closed loop He cryostat, made by ARS Cryo, Inc. 4K system, model # DE-204SF. In spring of 2016 a custom stage was machined at the University of Delaware so that samples could be tested without cleaving or wire-bonding. This custom stage is shown in Figure 6.7. It consists of copper block grounded to the FTIR and four pins that are electrically isolated and are connected to the FTIR BNC cable leads through the back. The copper stage is mounted directly onto the cold finger. The stage is meant to be used with the cryo in a horizontal position instead of a vertical one that had traditionally been used.

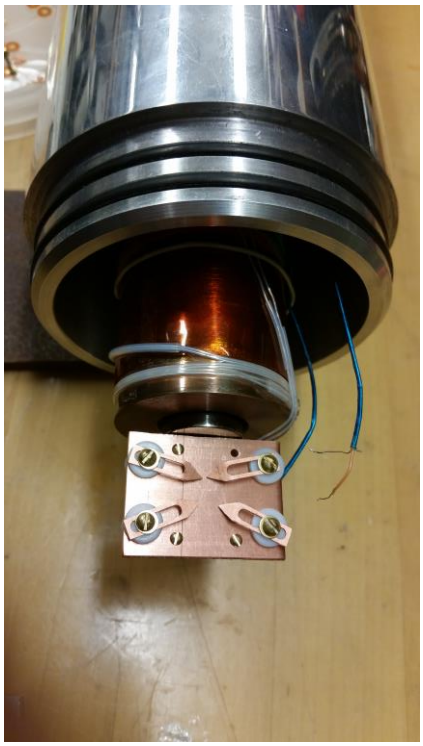

Figure 6.7: Custom stage machined for the ARS Cryo 4K system.

6.3.2 Choosing Beamsplitters/ Detectors/ Light Sources

In practice, the obtainable portion of the spectral data is limited by the combination of spectral responses of the beam splitter, the source, and the detector. The Thermo Fisher Scientific iS50r is equipped with two broadband light sources: IR and white light. The IR source is a globar, a silicon carbide infrared source that mimics the emittance of a 1140^{o}C blackbody source. The wavenumber range for this source is approximately from 9000 cm^{-1} to 20 cm^{-1}. The white light source is typically used for wavenumbers above 3000 cm^{-1} up to 32000 cm^{-1}. Table 6.2 lists the typical spectral ranges for many components available for use in the FTIR. Some beam splitter/ light source combinations have a stronger signal at a given spectral range than others. An example of the intensity of different beam splitter and light source combinations is shown in Figure 6.8 for the spectral range of interest for GeSn light emitters and detectors. In this range, the white light source and the CaF_2 beam splitter combination are the strongest in the Near -IR down to 2.5 µm, at which point the KBr beam splitter has a stronger signal. For even longer wavelengths, the IR source should be used.

Table 6.2: Suggested spectral ranges for iS50r beam splitter and detector combinations for the White Light (WL) and IR globar (IR) light sources.

Beam Splitter	Detector	Source	Spectral Range (cm^{-1})	Wavelength (µm)
Quartz	InGaAs	WL	12,000 - 4,000	0.83 – 2.5
		IR	7,400 – 4,000	1.35 – 2.5
	DTGS KBr	WL	4,000 – 2,800	2.5 – 3.6
		IR	4,000 – 2,800	2.5 – 3.6
	DTGS TEC	WL	12,500 – 2,800	0.83 – 3.6
		IR	7,400 – 2,800	1.35 – 3.6
	MCT - A	WL	4,000 – 2,800	2.5 – 3.6
		IR	4,000 – 2,800	2.5 – 3.6

	Silicon	WL	15,000 – 9,000	0.66 – 1.1
		IR	N/A	
CaF_2	InGaAs	WL	12,000 – 4,000	0.83 – 2.5
		IR	7,400 – 4,000	1.35 – 2.5
	DTGS KBr	WL	4,000 – 2,100	2.5 – 4.8
		IR	4,000 – 2,100	2.5 – 4.8
	DTGS TEC	WL	12,500 – 2,100	0.8 – 4.8
		IR	7,400 – 350	1.35 – 28.5
	MCT - A	WL	4,000 – 2,100	2.5 – 4.8
		IR	4,000 – 2,100	2.5 – 4.8
	Silicon	WL	15,000 – 9,000	0.66 – 1.1
		IR	N/A	
KBr	InGaAs	WL	7,400 – 4,000	1.35 – 2.5
		IR	7,400 – 4,000	1.35 – 2.5
	DTGS KBr	WL	4,000 – 2,000	2.5 – 5
		IR	4,000 – 400	2.5 – 25
	DTGS TEC	WL	7,400 – 2,000	1.35 – 5
		IR	7,400 – 2,000	1.35 – 5
	MCT - A	WL	4,000 – 2,000	2.5 – 5
		IR	4,000 – 650	2.5 – 15.4
	Silicon	WL	N/A	
		IR	N/A	

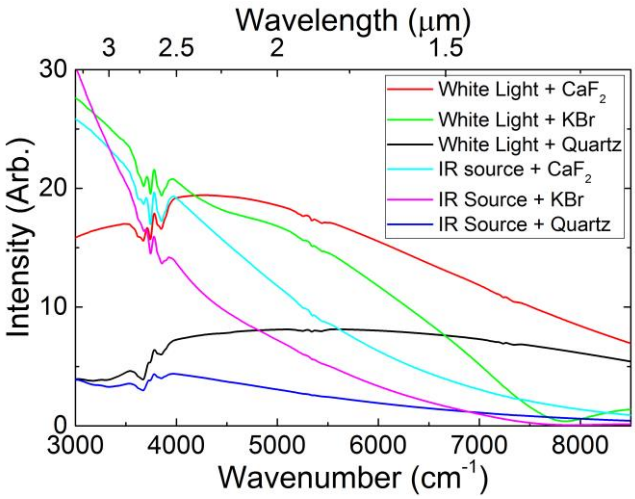

Figure 6.8: The beam intensity at the FTIR detector of multiple beam splitter / light source combinations for the range of NIR wavelengths interesting to GeSn devices. Data was taken on rapid scan mode with a resolution of 32cm^{-1} with a DTGS TEC detector that has a flat spectral response. The features at 3500 cm^{-1} and 5500 cm^{-1} are due to water absorption.

6.3.3 Removal of system background

As seen in Figure 6.8 variations in the detector response, the beam splitter efficiency, and amplifier characteristics all have a spectral response in the recorded intensity at the detector. The spectral response of the components will affect the shape of the resulting data and affect any subsequent curve fitting and analysis. Fortunately, each of these effects can be quantified, and a wavenumber dependent correction factor can be removed from the desired spectra to yield a corrected, actual, spectra.

As an example, the system background response of the setup used for measuring GeSn photoconductive devices was removed in the following way. The response of the GeSn device was measured, $I^*(\sigma)$. The measured response is a combination of the true device response, $I(\sigma)$, and the system background, $B(\sigma)$. The background was measured with the same setup, including the same scan parameters,

except that the light was directed to the internal DTGS TEC detector instead of the GeSn detector. The DTGS TEC detector has a spectral response that is flat over the near to mid-IR and can effectively be considered constant. The device response was then isolated according to the Equation 6.4,

$$I(\sigma) = \frac{I^*(\sigma)}{B(\sigma)} \tag{6.4}$$

FTIR single-beam spectra are spectrally correct but uncalibrated, the calibration of GeSn photodetectors is covered in Section 6.4.2.

6.3.4 Amplitude Modulation Step Scan

When the measurement of dynamic processes or low level signals is desired, amplitude modulated (AM) step scans are preferable to rapid-scan measurements. Amplitude modulated step scans generate an interferogram by recording the detector intensity as the mirror is moved in discrete steps. Low-level signals can be isolated from background radiation through opto-mechanical chopping or pulsing by using a lock-in amplifier. For weak signals, noise can be minimized by increasing the acquisition time per data point. Noise can then be further reduced by averaging several interferograms. Because the iS50r has the capability to interface with external detectors and sources, it is an efficient tool for the initial analysis and spectral characterization of non-optimized detectors. The parameters used for GeSn detector characterization using AM step scans in Chapter 7 and Chapter 8 are with 32cm^{-1} resolution, a device settling time of 1ms, a settling factor of 2ms, and an average step measurement time of 10 ms. The lock-in amplifier time constant was set to 10 ms.

6.4 Photodetector Measurements

For thin films, photocurrent spectroscopy is a useful technique for identifying spectral absorption characteristics that are too faint to see using reflection and transmission spectroscopy.

6.4.1 Semiconductor Photoconductor Theory

Photocurrent (PC) in semiconductor photoconductors occurs when incident radiation of sufficient energy creates electron-hole pairs. In the presence of an electric field, the optically generated carriers are swept to the contacts where their contribution to the total current in the device can be measured. Absent illumination, the conductivity of a semiconductor can be expressed as

$$\sigma_o = q\mu_e N_o + q\mu_h P_o \tag{6.5}$$

where N_0 and P_0 are the free carrier concentrations of electrons and holes, respectively, μ_e and μ_h are the electron and hole mobilities, respectively, and q is magnitude of the electron charge. When a photoconductor is illuminated, the change in conductivity is called the photoconductivity, which can be represented in terms of the concentrations of excess electrons, ΔN, and holes, ΔP, as

$$\Delta\sigma = q\mu_e \Delta N + q\mu_h \Delta P \tag{6.6}$$

so the total conductivity under illumination is,

$$\sigma = \sigma_o + \Delta\sigma = q[\mu_e(N_o + \Delta N) + \mu_h(P_o + \Delta P)] \tag{6.7}$$

Since the photoconductors considered in this dissertation are intrinsic, for simplicity the electron and hole free (dark) carrier concentrations were assumed to be the same, and because any excess carriers are created in pairs, the excess carrier concentrations were also assumed to be equal. Thus,

$$\sigma = \sigma_o + \Delta\sigma = q(\mu_e + \mu_h)(N_o + \Delta N) \tag{6.8}$$

Excess carriers that contribute to photocurrent depend on the wavelength of radiation incident on the detector,

$$\Delta N = \frac{\eta \lambda \Delta \phi_e \tau_L}{hcA_d t} \tag{6.9}$$

where η is the external quantum efficiency, λ is the wavelength of the radiation, $\Delta\varphi_e$ is the radiant power incident at that wavelength, τ_L is the carrier lifetime, h is Planck's constant, c is the speed of light, A_d is the detector area, and t is the detector thickness. Alternatively, in terms of incident photons,

$$\Delta N = \frac{\eta \Delta \phi_e(\lambda) \tau_L}{A_d t} = \frac{\alpha(\lambda) t}{V_d} \tag{6.10}$$

where $\Delta\varphi_e$ is the number of incident photons per second, A_d is the detector area, t is the detector thickness (see Figure 6.9a), α(λ) is the wavelength dependent absorption coefficient, and V_d is the detector volume. The relative change in conductivity, or photoconductivity, under illumination can then be expressed as,

$$\frac{\mathrm{d}\sigma}{\sigma} = \frac{q(\mu_e + \mu_h)\alpha(\lambda) t}{\sigma V_d} \tag{6.11}$$

or, in terms of the change in resistance,

$$dR_d = -R_d \frac{q(\mu_e + \mu_h)\alpha(\lambda) t}{\sigma V_d} \tag{6.12}$$

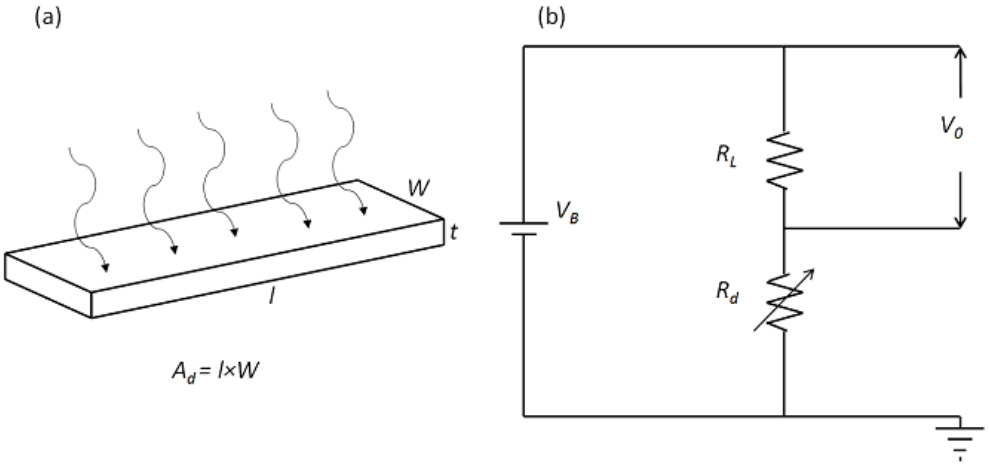

Figure 6.9: Photoconductor geometry. (a) Light incident on a surface A_d (b) Biasing circuit for photoconductor measurements, as referenced in the text.

Equation 6.12 suggests that the change in device resistance as a result of incident photons of known wavelength can be used to quantify photocurrent when the sample is under a DC bias. One commonly used biasing circuit is show in Figure 6.9b and consists of a DC voltage source supplying the photoconductor through a matched resistor. With the biasing circuit active, photocurrent generated in the device can then be determined by monitoring the resultant change in output voltage, V_0, as the light source is modulated. The change in output voltage is given as,

$$dV_o = \frac{V_B R_L R_d}{(R_d + R_L)^2} \frac{q(\mu_e + \mu_h)\alpha(\lambda)t}{\sigma V_d} \tag{6.13}$$

where q is the electron charge, is the, μ_n and μ_p again are the electron and hole mobilities, $\alpha(\lambda)$ is the absorption coefficient as a function of the wavelength of the incident radiation, σ is the dark conductivity of the semiconductor, V_d is the detector volume, V_B is the bias voltage, and R_L and R_d are the load and detector resistances.

Thus, the change in the output voltage under illumination is proportional to $\alpha(\lambda)$, the absorption coefficient.

6.4.2 Bench Setup and Responsivity Calibration

The single-beam spectra the FTIR produces need to be calibrated for the absolute magnitude of the response. The method of calibration covered here involves calibrating the responsivity of a GeSn detector at one wavelength value. The responsivity at different wavelengths can then be inferred from the FTIR spectrum. The method discussed here was used to measure the GeSn photoconductors and photodiodes in Chapter 7 and Chapter 8 respectively, and the specifics of those experiments are mentioned in their respective chapters.

The internal FTIR setup for measuring photoconductors followed the configuration shown in Figure 6.3, where a collimated light beam exited the FTIR on the left hand side of the tool. The optical bench setup for measuring photoconductive responsivity is shown in Figure 6.10.

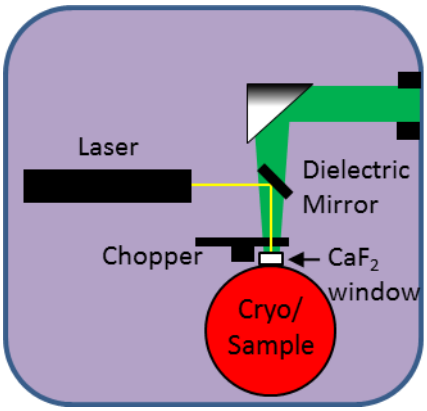

Figure 6.10: The optical bench setup for GeSn photoconductivity measurements. The light from the FTIR (in green) enters the N2 purge box from the right, it reflects off of a collimating mirror and travels through a chopper wheel before it arrives at the sample. For responsivity calibration, a laser is used as the incoming light (in yellow), which reflects off of a dielectric mirror mounted on a pivoting stand that lets it rotate out of the FTIR beam path when not in use.

A laser is used to measure the devices response at one wavelength. The power of the laser is measured using a calibrated laser power meter, which measures in W/cm^2, while the power meter is placed in the exact sample position before the sample is mounted. It is important that any windows, such as the CaF_2 window shown in Figure 6.10 are in place when the measurement is taken, as they reduce the incident laser power due to reflection/absorption and affect the reading. Once the laser power is calibrated then the power meter can be removed and the GeSn devices mounted.

Photoconductive devices are calibrated according to the following method shown in Figure 6.11, the current-voltage characteristics of a GeSn photoconductive device in the dark and upon being exposed to 1550 nm laser light. When light is incident on the sample, carriers are generated and the conductivity increases, resulting is a photocurrent. In Figure 6.11 the measured photocurrent was around 10 mA at 2 V

bias, which, after accounting for device area and laser power, resulted in a 1550nm responsivity of 0.15 A/W at 2 V bias. The FTIR spectra is then scaled so that the response at 1550 nm is equal to 0.15 A/W. This is then repeated for all samples. For the photodiode samples in Chapter 8 the short circuit current was used, so the current was measured in the same way, but without biasing the sample. The individual methods are discussed further in Chapter 7 and Chapter 8.

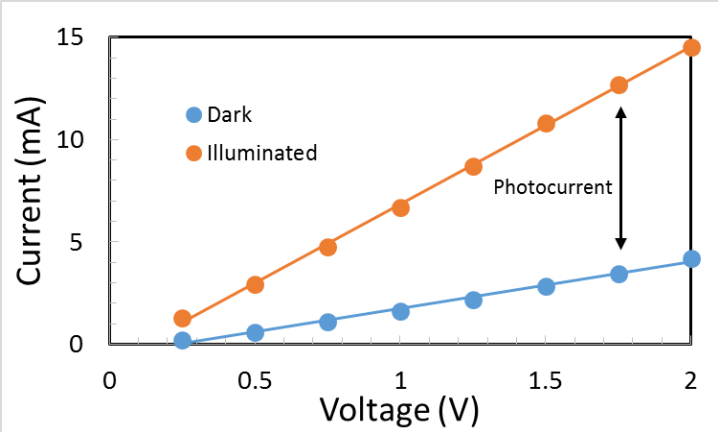

Figure 6.11: Current-voltage characteristics of an 11% Sn photoconductor at 25 K in the dark and with exposure to a 1550 nm laser at a power of 50 µW, showing the photocurrent.

Chapter 7

TEMPERATURE VARYING PHOTOCONDUCTIVITY OF GERMANIUM-TIN ALLOYS GROWN BY RPCVD

7.1 Introduction

The photoconductivity of GeSn layers has been measured previously at cryogenic temperatures with Sn concentrations up to 10% grown on Ge substrates [29], as well as a 9% Sn strained layer grown on a relaxed Ge layer on a Si substrate measured at room temperature [99]. The temperature dependent photoconductivity has also been measured on GeSn layers up to 10% Sn [100]. In this chapter the temperature dependent spectral photoconductivity for samples of GeSn layers grown strained to relaxed Ge virtual substrates on Si wafers, with Sn compositions of up to 11.3% are measured.

7.2 Sample Preparation

GeSn deposition was conducted by reduced pressure chemical vapor deposition (RPCVD) on a bare Si(001) substrate in a Centura® 300 mm RP Epi chamber from Applied Materials. A low temperature (< 350°C) process was developed to overcome challenges such as low Sn solid solubilities in Ge and Sn surface segregation. Strained GeSn layers were grown on relaxed Ge buffer layers on double- sided polished 300 mm p-type Boron doped (1–10 Ohm-cm) Si. Digermane (Ge_2H_6) and tin tetrachloride ($SnCl_4$) were used as precursors for Ge and Sn, respectively. The substrates were subjected to a high temperature hydrogen bake at

1040^{o}C to remove any contamination on the Si substrate wafer before Ge deposition. No intentional doping source was used during the growth.

For electrical characterization of deposited GeSn films, adjacent Ti/Au finger contacts were patterned on the surface of the samples by standard lithography techniques as shown in Figure 7.1. The electrical contacts were 600 nm thick Au on 30 nm of Ti, with dimensions 2.8 mm long by 50 um wide and separated by 50 um (the top device in Figure 7.1). The GeSn Samples were cleaved to approximately 4 mm x 8 mm devices and mounted on a copper block for improved temperature uniformity.

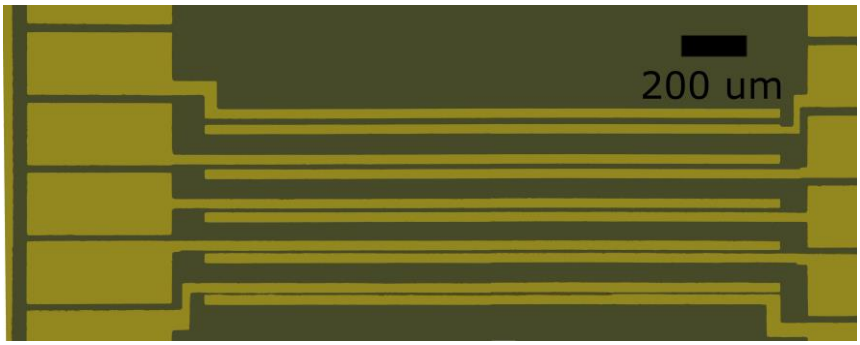

Figure 7.1: A top view photomicrograph of a typical photoconductive device, showing a series of Au/Ti metal finger electrodes with larger contact pads for wire bonding on the left and right. The photo shows five device configurations, each with different separations between fingers: 50 μm – 10 μm in steps of 10 μm. For this study, the device configuration used is at the top of the photo, with 50 μm spacing between fingers.

7.3 Measurements

High resolution X-Ray diffraction (HRXRD) was performed with ω-2θ coupled scans and reciprocal space measurements (RSM) using a Philips/Panalytical X'Pert MRD, results of which are summarized in Table 7.1. Across all samples measured via RSM, the Ge virtual substrate (VS) was found to have a small, in-plane,

tensile strain, $\varepsilon_{\parallel} = (a_{\parallel} / (a_0 - 1)) * 100$, presumably due to post Ge epitaxy wafer cooling and the mismatch between the thermal expansion coefficients for the Si substrate and the Ge-VS. GeSn layer compositions were determined via high resolution reciprocal space maps in a <224> alignment following the procedure of [89], while assuming the lattice constant and Poisson's ratio of the GeSn layers follows Vegard's Law [87]. The composition from x-ray diffraction was in good agreement with previous Rutherford Back Scattering (RBS) measurements performed on the same samples [101]. All GeSn layers were found to be fully strained against the Ge-VS, with the relaxation measured by RSM to be ≤1% for all layers. ω-2θ coupled scans in a <004> alignment were performed, and layer interference fringes were used to determine the thickness of the epilayer. The results for the XRD measurements are shown in Table 7.1. The Ge virtual substrate was 640nm thick, approximately 10x the thickness of the GeSn layers [101].

Table 7.1: Results from XRD measurements. The strain in the Ge virtual substrate and the GeSn layers as well as the Sn content were extracted from the (224) reciprocal space maps. The thickness of the GeSn layers was extracted from (004) ω-2θ layer thickness fringes. RBS measurements from the same sample set was included from [101].

	(224) RSM				RBS	(004) ω-2θ
Sample	Ge VS $\varepsilon_{\parallel}$ %	GeSn $\varepsilon_{\parallel}$ %	GeSn $\varepsilon_{\perp}$	Sn (%)	Sn	GeSn
1	0.16	-	-	0.0%	0.0%	-
2	0.17	-0.47	0.36	4.5%	4.5%	76
3	0.17	-0.52	0.39	5.2%	5.5%	78
4	0.17	-0.71	0.54	6.2%	6.0%	69
5	0.19	-0.80	0.61	7.0%	7.3%	67
6	0.19	-1.02	0.77	8.6%	8.0%	62
7	0.17	-1.13	0.86	9.6%	9.0%	65
8	0.23	-1.38	1.05	11.3%	11.0%	66
9	0.19	-1.41	1.07	11.1%	11.0%	66

The GeSn photoconductivity was measured by fourier transform infrared spectroscopy (FTIR) on a Thermo Fisher iS50R system equipped with a CaF_2 beam-splitter. The copper block with GeSn devices was mounted in a He cryostat (ARS, Inc. DE-204SF) equipped with a CaF_2 transmission window and arranged in the beam path of the FTIR. A mechanical rotary chopper set to a frequency of 509Hz was used to modulate the light from the iS50r internal Xe lamp white light source. The GeSn device was placed in series with a 2 VDC power supply and a 100 Ohm resistor. The voltage across the sample was probed by a lock-in amplifier synchronized to the chopper. Fine alignment of the FTIR beam was done by maximizing the signal strength on the lock-in amplifier. The signal from the lock-in was fed back into the FTIR control electronics and analyzed using the software Omnic. The lock-in time constant was set to 10 ms. The measurements were done in amplitude modulation step scan mode with 32 cm^{-1} resolution, a device settling time of 1 ms, a settling factor of 2 ms, and an average step measurement time of 10 ms. As a reference signal, a thermoelectrically cooled deuterated triglycine sulfate (DTGS) detector was used to measure the background of the FTIR system under the same scan conditions as the device, giving a spectrally dependent FTIR response curve for the optical path. The FTIR response curve was then divided out of the original GeSn photoconductivity measurements in order to remove it and subsequently provide the response from the GeSn devices alone. Multiple scans of each device at each temperature were averaged in order to reduce error from random noise.

The photocurrent of the fabricated device can be described by [29]:

$$I_{ph}(h\nu) = \frac{q\eta\Delta\phi_e\tau_L(\mu_n+\mu_p)Wd^2V_B}{h\nu*l}\alpha(h\nu) \tag{7.1}$$

where q is the electron charge, η is the quantum efficiency, $\Delta\varphi_e$ is the spectral power incident on the sample, α(hν) is the spectral absorption coefficient, *d* is the thickness of the device absorbing layer, *W* is the lateral width of the device contacts, *h* is Planck's constant, *c* is the speed of light, *l* is the separation between contacts, and V_B is the bias voltage. τ_L and μ_n, μ_p are the carrier lifetime and the electron and hole mobilities respectively, collectively referred to as the mobility-lifetime or μτ product and are an important metric for device quality.

The DC dark current was measured to be linear with bias, and the dark conductance is shown as a function of temperature in Figure 7.2. At room temperature, the dark conductance increased with increasing Sn composition. In addition, across all temperatures, the 11.3% Sn device, had a dark conductivity approximately 3 times larger than the Ge reference device. At temperatures below 77K, the 6.2% and 9.6% Sn samples had a lower dark conductivity than the Ge reference sample, while at higher temperatures the dark conductivity was between that of the Ge reference sample and the highest Sn concentration.

The conductance data is plotted in Figure 7.2 as an Arrhenius curve in order to extract an activation energy from the slope. From room temperature down to 77K, the activation energy of the conductance varied from 10-30meV for all samples. In extrinsic semiconductors, the activation energy should be related to the dopant ionization energies in the material. Many groups have found GeSn layers to have an un-intentional p-type doping [102], [103], this is thought to be from acceptor-like multi-level Ge vacancies due to the low epitaxy growth temperature [96]. The activation energy for multi-level Ge vacancies is 10-20meV [104], which is close to

the activation energy measured in this work, and could be the source of what is observed.

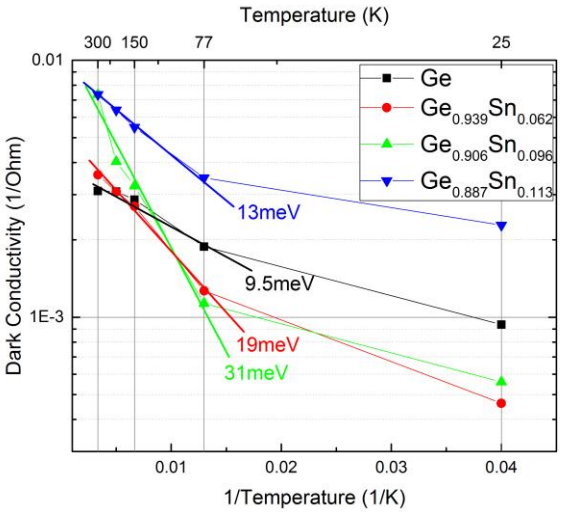

Figure 7.2: The dark conductance of the photoconductor devices as a function of temperature showing an increase in the dark resistance as the temperature is decreased and carriers are frozen out.

The responsivity of the devices was calibrated by placing the GeSn device in series with a 2V power source and an ammeter and using A 1550 nm free space laser to illuminate the device. The power of the laser was measured to be 50 $\mu W/cm^2$ at the sample, with a 1550 nm calibrated photodetector. The responsivity of the GeSn device was calculated simply by measuring the current at 2 V with the laser powered on, subtracting the dark current at the same voltage, and dividing by the incident power. The cleaved area of the device was used to calculate the incident power. At low temperatures the illumination from the laser caused heating in the device; this was seen in the current slowly rising with time as the laser was on as well as slowly

dropping with time after the illumination was turned off. In order to prevent heating at low temperatures, both the voltage and the laser were pulsed with pulses lasting less than a second, with long "off" times on the order of ten seconds. The laser illumination was pulsed with a manual shutter.

The resulting FTIR spectra was normalized, and plotted as a function of wavelength at 300K in Figure 7.3a. The Ge reference sample curve (solid black) has a strong peak with an edge approximately 0.8 eV, corresponding nicely to the literature value of the direct gap in germanium of 0.8 eV. The indirect gap of bulk germanium is 0.66 eV at room temperature, and the photocurrent associated with this indirect peak is visible as a small signal tail that extends to longer wavelengths. The GeSn samples all show a similar peak at 0.8 eV, attributed to the germanium of the virtual substrate and an additional absorption peak that is seen to shift to lower energies as the Sn concentration is increased. A peak associated with the silicon substrate, not shown here, was observed for wavelengths <1.1 um.

The responsivity measured with the 1550 nm laser is shown as the inset in Figure 7.3a. The response is strongest for the 4.5% Sn and 5.2% Sn alloy, with values of 0.027 A/W and 0.022 A/W respectively. The 1550 nm response of the devices for all other concentrations, including the Ge reference device, showed similar magnitudes, this is an important result in that it shows that even as the Sn concentration is increased in the alloys up to 11%, and the GeSn material was increasingly metastable, there was no decrease in the photodetector quality.

Figure 7.3b shows the 1550 nm responsivity of samples 1, 4, 7, and 9 as a function of temperature. At 300K, the direct band gap of germanium is 0.8 eV (1550 nm). As the temperature is decreased however, the band gap of germanium increases,

and the absorption spectra will shift to shorter wavelengths. For temperatures below 300K, the direct band gap of germanium shifts to higher energies and less strongly absorbs 1550 nm light. The shift is apparent in Figure 7.3b where, as the temperature is decreased in the Ge reference sample, the 1550 nm responsivity decreases. With the addition of Sn to the devices the wavelength response is shifted to much lower energies and longer wavelengths. Thus, the GeSn samples response at 1550 nm as temperature is decreased should be less dependent the bandgap moving to a higher energy.

What is observed in this study, shown in Figure 7.3b, is that as temperatures are decreased the responsivity at 1550 nm is generally increased in the GeSn devices. The 6.2% Sn sample had a maximum at 150K while the response for the two higher Sn concentration samples continued to increase at lower temperatures. At 25K the responsivity of the highest Sn concentration sample was two orders of magnitude higher than the germanium reference sample. An effect that could explain the increase in responsivity as temperature is lowered is that as the temperature is decreased the $\mu\tau$, seen in Equation 6.1, increases due to less scattering from phonons. A higher $\mu\tau$ would imply that more carriers can be collected before recombining. The peak in the 6.2% Sn sample could be explained as a competition between greater carrier collection increasing the response, and the absorption shifting higher in energy with the band gap and subsequently decreasing the response.

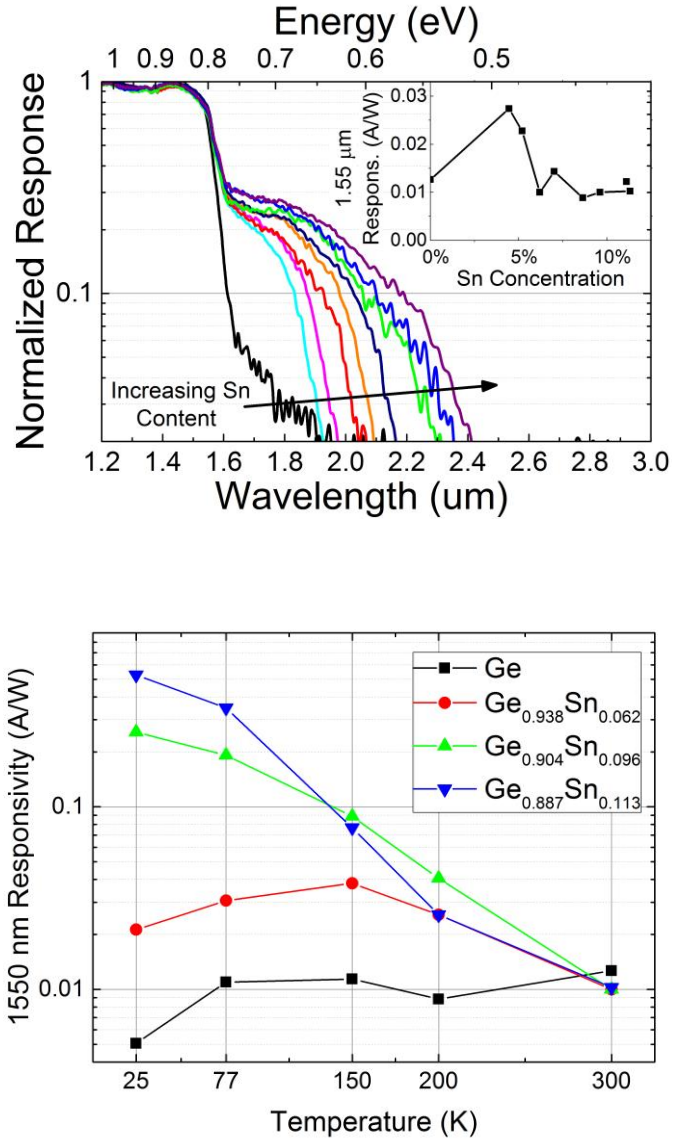

Figure 7.3: a) Normalized Response vs. wavelength at 300K for Ge (black curve) and GeSn photoconductors with Sn from 4.5% to 11.3%. The inset is a plot of 1550nm responsivity vs. Sn concentration at 300K. b) 1550 nm responsivity as a function of temperature for three different compositions: 6.2%, 9.6%, and 11.3% Sn.

7.4 Band Gap Extraction

From Equation 6.1 we can see that the measured photocurrent is proportional to α, the absorption coefficient. The spectral characteristics of the absorption coefficient give insight on the band structure of the semiconductor through the equation,

$$\alpha \propto \frac{\beta}{h\nu}\left(h\nu - E_g \pm E_{ph}\right)^m \tag{7.2}$$

where β is a constant, hν is the photon energy, E_g is the semiconductor band gap, E_{ph} is the effective phonon energy for indirect band transitions, and m is an exponential factor depending on the nature of the optical transition [105]. In a direct band gap material, the exponent, m, is equal to ½, while in an indirect material it equals 2. A Tauc plot [106] was used to find the direct bandgaps of the devices, following the standard procedure of plotting $(\alpha * h\nu)^2$ vs. hν to find the direct gap and extrapolating the straight line regions of the resulting plots to the energy axis to find the band gap.

The Ge responsivity data in Figure 7.3a, shows an absorption tail extending to lower energies from the main peak. The responsivity of this tail is approximately an order of magnitude smaller than that of the main Ge peak, and was attributed to the indirect gap of Ge. The indirect band gap of the Ge reference device was extracted from the Tauc fitting method of plotting $(\alpha * h\nu)^{1/2}$ vs. Energy, and yielded an energy intercept of 0.61 eV. No similar low energy tail for the GeSn devices was observed that could be attributed to indirect band absorption. Using the Ge device as reference, a tail due to indirect band absorption could be expected for the GeSn samples at roughly an order of magnitude less intensity than the direct peak, which is at or below

the noise floor of the measurement. With more sensitive experiments or perhaps thicker GeSn device layers, the indirect tail could be seen.

The extracted values of the direct and indirect band gaps are plotted in Figure 7.4 as a function of Sn concentration. For the pure Ge sample, both the direct and indirect band gap are lower than the literature values, this is to be expected however, as the layer has a slight tensile strain, seen in Table 7.1. As the Sn concentration is increased, the direct band gap of the material decreases as expected. The lowest bandgap measured with the photoconductive absorption method in this work (shown with red circles) agrees nicely with the direct bandgap measured using VASE on the same samples[101], shown by the inverted green triangles.

As seen in Table 7.1, all samples in this study had varying amounts of strain, which will affect the band structure of these materials in many ways, most notably by splitting the valence band into separate heavy hole and light hole bands. In order to more accurately compare the band gap measured in this work with theory, the values of the heavy hole and light hole band gaps for strained GeSn were calculated using deformation potential theory [16]. The in-plane and perpendicular strain components as well as the Sn compositions from Table 7.1 were used to generate theoretical band gap values shown in Figure 7.4. The values for the deformation potential fitting parameters were taken from [16], specifically the bandgap bowing parameter is 2.42eV, and the dilational and shear deformation potentials of the direct band gap are -11.04 eV and -4.07 eV, respectively. For this analysis, the split off band energy was taken to be that of Ge Δ_0 = 0.289 eV. It's worth mentioning that the deformation potential theory predicts that the bandgap of the compressively strained GeSn material will be higher in energy than that of the relaxed GeSn material.

Comparing the data with the theory in Figure 7.4, there is very good agreement between the lowest direct bandgap measured in this work, the bandgap measured by VASE in [101], and the theoretical value for the energy of the heavy hole valance band to Γ-point of the conduction band transition

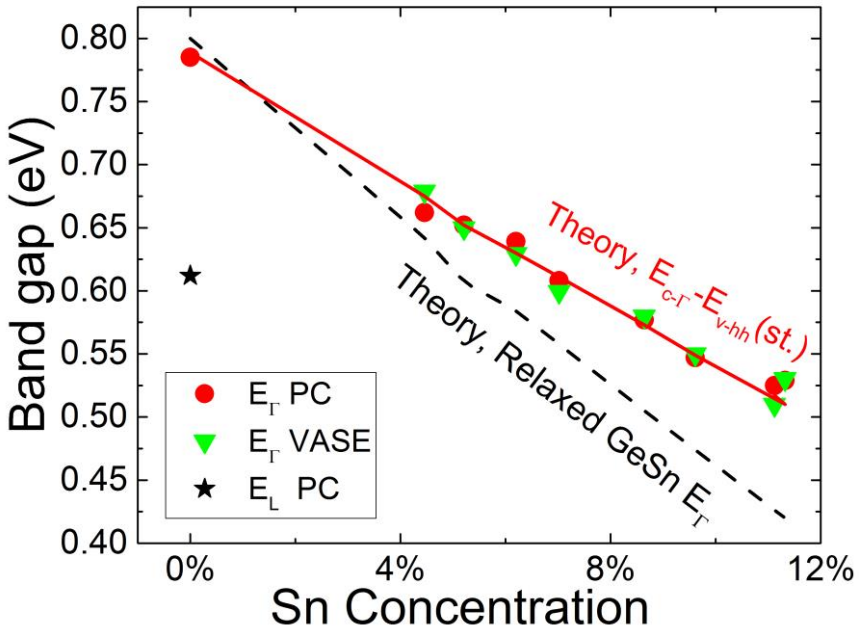

Figure 7.4: A comparison between theory and extracted band gaps vs. Sn concentration at 300K. The direct band gap and the indirect band gap of Ge measured by photoconductivity (PC) are indicated by the red circles and the black stars, respectively. The data has been plotted as a function of Sn concentration from the XRD values in Table 1. Variable angle spectroscopic ellipsometry (VASE) measurements of the direct band gap for the same samples [101] are also shown as inverted green triangles. The dashed black line is the direct band gap, E_Γ, vs. Sn concentration for a relaxed GeSn material with a band gap bowing parameter of 2.4eV, obtained from [108]. The red line is the theoretical band gap to the heavy hole valence band, from [108] with more details given in the text.

7.5 Varshni Analysis

The band gap of semiconductors increases as the temperature is decreased, due to the decreased interatomic distances between atoms. This phenomena is described by the equation of Varshni [109],

$$E_g = E_0 - \frac{\alpha T^2}{T+\beta} \tag{7.3}$$

where Eg is the band gap, E_0 is the band gap at absolute zero, and α and β are empirical fitting constants. The direct band gap of the devices was measured as a function of temperatures and plotted in Figure 7.5. The data points in the figure are the measured bandgap of the alloys from this work, while the trend lines through them are fits to the Varshni equation, the parameters of which are shown in Table 7.2. The values obtained for the Varshni equation are close to what has been reported elsewhere for GeSn [110]. With decreasing temperature, there will be a change in the strain of the layers due to thermal expansion mismatch between the different material layers, which wasn't measured, but should be kept in mind when viewing Figure 7.5 and Table 7.2.

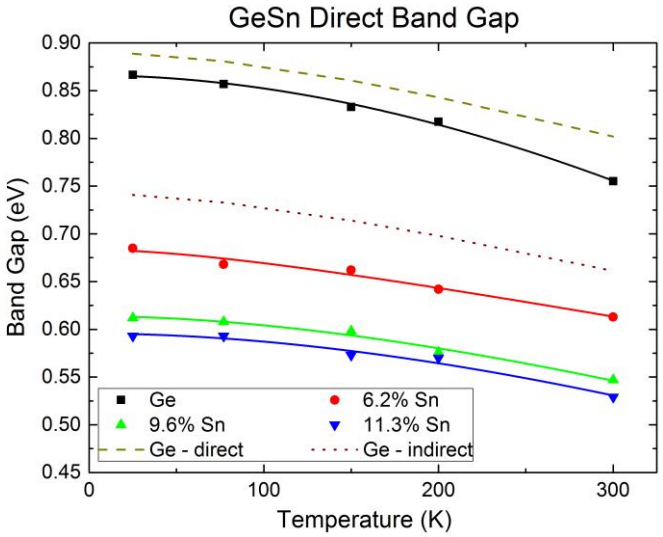

Figure 7.5: The band gap value extracted from the FTIR data at a series of temperatures for strained GeSn layers grown on a Ge-VS. The curves through the data point symbols are fits to the Varshni equation, and the fitting constants for these curves are noted in Table 2. The dashed line and the dash dotted line are literature values for the Γ-valley of germanium and the L-valley of bulk germanium respectively.

Table 7.2: The Varshni fitting parameters for the direct band gap of Ge and GeSn alloys as a function of temperature. The extracted band gap E_Γ at room temperature for these devices is shown for reference.

Sample	Sn	E_0 eV	α	β	E_Γ 300K eV
1	0%	0.866	2.4E-3	1.6E3	0.785
4	6.2%	0.683	3.5E-4	1.5E2	0.639
7	9.6%	0.613	7.0E-4	6.3E2	0.547
8	11.3%	0.595	9.7E-4	1.1E3	0.529

7.6 Conclusion

In summary, we have analyzed GeSn photoconductive layers for their photoconductive response in the near to mid IR region. In addition to shifting to longer

wavelengths with the addition of Sn, the photo-response was greatly improved in the long wavelength region. A peak was seen in the 1550 nm photoconductive response for the 4.5% and 5.2% Sn samples, which exhibited a responsivity of 2-3x that of Ge alone. The dark current of the devices was found to increase with Sn concentration at room temperature, up to 3x the dark conductivity of the Ge reference device. However, this was not found to be the case as temperature was decreased, below 77 K the dark conductivity for the 6.5% and 9.6% samples was below that of the Ge reference sample. The band edge of the GeSn devices was extracted from the photoconductivity data and was seen to shift to lower energies with the addition of Sn, as expected. The data was compared with other GeSn literature and the lowest energy gap was found to closely match to the predicted heavy hole band transition energy by the deformation pseudopotential method. We conclude that GeSn devices are a promising CMOS compatible material for applications in the near to mid-IR range.

Chapter 8

INFRARED HOMOJUNCTION PHOTODIODES OF GERMANIUM TIN GROWN BY MOLECULAR BEAM EPITAXY

8.1 Introduction

The motivation and applications for Mid-IR devices are many, and outlined in Chapter 1. To achieve response in the mid-IR with GeSn alloys, the Sn content in the film has to be pushed higher than has been achieved previously for devices. To achieve the desired 3-5 μm response at room temperature, GeSn devices with relaxed Sn contents from 11-17% are needed. Strain relaxation is desirable, as seen in Figure 1.6 and ref [15], because any compressive strain will push the direct bandgap higher in energy, and drive the indirect/direct bandgap crossover point higher in Sn concentration. Cooling of the device below room temperature, as is typically done with mid-IR devices in other material systems, will also raise the Sn content required to reach mid-IR, as the bandgap of the material will increase at lower temperatures.

While GeSn films with Sn contents up to 25% [111] and even 46% [18] have been grown, little characterization exists for *devices* with such high Sn contents. Some of the highest Sn content devices reported in the literature have been looked at for light emission, such as an optically pumped $Ge_{0.88}Sn_{0.12}$ laser [23], a $Ge_{0.89}Sn_{0.11}$ active layer homojunction LED [112], as well as an n-Ge/i-$Ge_{0.88}Sn_{0.12}$/p-$Ge_{0.92}Sn_{0.08}$ (optically measured, though up to 13.7% Sn grown and fabricated) LED [25]. For detectors, the highest Sn content devices are a compressive strained p-$Ge_{0.88}Sn_{0.12}$/n-Ge heterojunction detector with response out to around 2.2 μm [26] and the GeSn

photoconductive devices by our group described in Chapter 7 [113] with response out to 2.4 µm. Photodiodes, especially, are more technologically interesting in particular for low bandgap detectors as they have a higher theoretical signal-to-noise (SNR) limit compared to photoconductive devices [114].

This chapter covers the current-voltage characteristics and the optical response of GeSn homojunction devices, grown on Si substrates, with high Sn contents of up to 15.6%. The wavelength response, at room temperature, extends out to almost 4 µm, which is needed for the technologically important mid-IR region.

8.2 Sample Preparation

Three GeSn samples, listed in Table 8.1, were grown via the MBE system discussed in Chapter 5, and fabricated with the layer configuration shown in Figure 8.1. The growth started on a lightly doped p-type Si wafer, followed by 600 nm of undoped Ge virtual-substrate (VS) layer, grown as outlined in Section 5.7. The Ge VS layer was followed by GeSn buffer layer(s). All devices had a thin 9% GeSn buffer, while the device with the 8.9% Sn active layer had an additional 15% Sn buffer (layer 2a) in order to more fully relax the GeSn active layer with less total growth thickness than would be needed with just an 8.9% Sn layer. The doping concentration of the n- and p-type GeSn was $5*10^{18}$ cm^{-3} as calibrated by SIMS, shown in Section 5.4.

The GeSn films with different active layer Sn concentrations were grown at different temperatures: sample SGS152 with 8.9% @ 150^{o}C, sample SGS148 with 12.8% @ 120^{o}C, and SGS 150 with 15.6% @ 100^{o}C, and at different growth rates: 8.9% Sn @ 0.76 nm/min, 12.8% @ 0.77 nm/min, and 15% @ 0.78 nm/min. The Ge cell temperature was held constant at 1215^{o}C, and the Sn cell temperature was varied

from 980ºC to 1008ºC in order to vary the Sn concentration from 8.9% to 15.6%, respectively.

Futurrex NR9-3000PY negative photoresist was used for photolithography to form patterns for the device mesas and the metal contacts. The photoresist procedure involved a 150ºC soft-bake of the photoresist, which was the highest temperature that the GeSn devices were exposed to after growth, followed by exposure in a Karl Seuss MJB-3 mask aligner, and development using RD6 developer. The devices were isolated with a mesa etch prior to metallization using the developed photoresist as an etch mask. The mesa etching was done with a wet etch, which was a (72:3:3:22) mixture of phosphoric acid, acetic acid, nitric acid, and water respectively. This acid mixture is mildly selective to Ge over GeSn, and etched from 100 – 200 nm/min, with higher etch rates for lower Sn concentrations. The acid mixture did have a delay before etching of approximately a minute. Mesa heights were targeted at 350 nm, about halfway through the p-GeSn layer (Layer 3 in Figure 8.1). The devices were circular with an area of 1 mm^2. The metal contact layers were defined using a metal lift-off process and formed annular rings. The metal layers consisted of Ti (20nm)/ Pd (10nm)/ Ag (300nm) layers, deposited by e-beam evaporation, chosen based on good results with previous GeSn devices at the University of Delaware [24]. There was no annealing step performed after metal deposition. The final devices were un-passivated and had no anti-reflection coating.

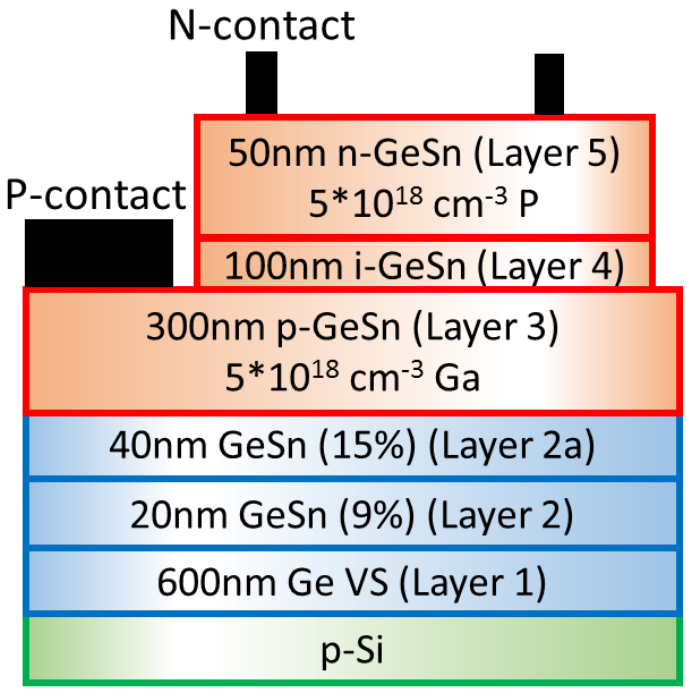

Figure 8.1: The device layer schematics for the GeSn homojunction photodetectors. Layer 2a was only used for the device with the 8.9% Sn active (PiN) GeSn layers.

8.3 Measurements

High resolution X-Ray diffraction (HRXRD) <224> reciprocal space maps (RSM) were taken using a Philips/Panalytical X'Pert MRD to characterize the film composition and relaxation. An RSM of SGS152, the 8.9% Sn active layer sample, is shown in Figure 8.2, and results for the other samples are summarized in Table 8.1. Among all samples measured via RSM, the Ge virtual substrate (VS) was found to have a small in-plane tensile strain, characterized by the Ge buffer peak being above the "relaxed film" line. The tensile strain in the Ge buffer is presumably due to post Ge epitaxy wafer cooling and the mismatch between the thermal expansion coefficients for the Si substrate and the relaxed Ge. GeSn layer compositions were

determined following the mathematical procedure of [89], assuming that the lattice constant and Poisson's ratio of the GeSn layers follows Vegard's Law [87].

The different layers from Figure 8.1 can be seen in the <224> RSM of Figure 8.2, Layer 1 is the Germanium virtual substrate, Layer 2 is the initial pseudomorphic, strained, 9% Sn buffer layer, and Layer 2a is the ~15.2% Sn relaxation layer. An initial small 15.2% Sn peak can be seen strained to the Ge VS layer (indicated in Figure 8.2), as well as a contour tail that extends towards the relaxation line, indicating that relaxation occurs in the 15.2% layer. Most likely a small amount of >15% Sn alloy deposited before the layer relaxed, leaving some material still strained to the Ge buffer. The active Sn layers (3, 4, and 5) are all at one lattice constant, which is grown pseudomorphic on Layer 2a. A small residual biaxial compressive strain remains in the 8.9% Sn layer, characterized by its RSM peak being below (smaller Qy) the diagonal "relaxation line". As seen in Table 8.1, all three different GeSn devices have different active layer Sn concentrations and degrees of film strain. While a higher Sn content will result in a lower bandgap, a higher amount of strain will counteract the effect, as seen in Figures 1.5 and 1.6 in Chapter 1, and summarized in Table 8.1.

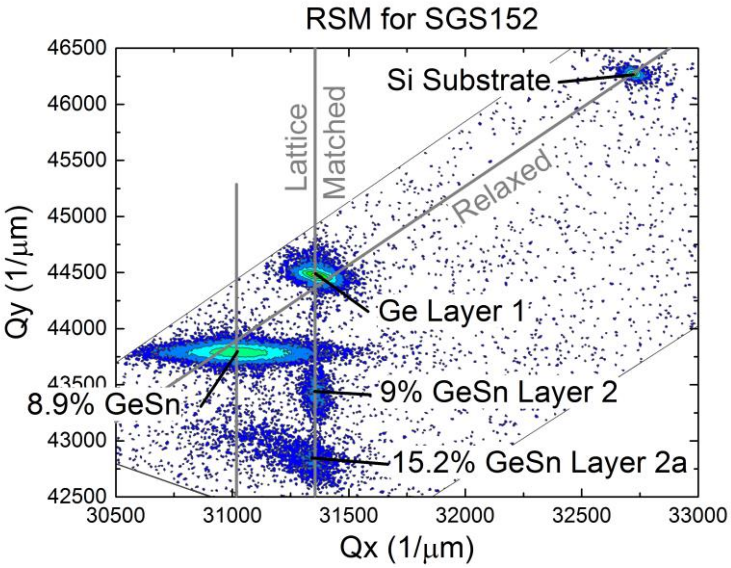

Figure 8.2: <224> RSM for SGS152 showing the peak position for each layer. The diagonal grey line passing though the Si peak and near the Ge and 8.9% Sn peak represents the locus of peak locations for a completely relaxed film. Peaks above the diagonal line are under biaxial tensile strain, while those below the diagonal are under biaxial compressive strain. The vertical grey lines indicate an identical in-plane lattice constant, layers on the same vertical line are lattice matched.

Table 8.1: Sample numbers, Sn concentrations, and strain parameters for the GeSn homojunction devices. The in plane strain, $\varepsilon_{\parallel} = (a_{\parallel} / a_0 - 1)) *100$, and out of plane strain, $\varepsilon_{\perp} = (a_{\perp} / a_0 - 1) *100$, of the GeSn active layers are shown. All devices are expected to be direct band-gap, as indicated by a positive value for the energy difference between conduction band peaks ($E_{cL} - E_{c\Gamma}$) obtained from [15].

Sample	Sn %	GeSn $\varepsilon_{\parallel}$ %	GeSn $\varepsilon_{\perp}$ %	$E_{cL} - E_{c\Gamma}$ (meV)
SGS152	8.9	-0.08	0.06	50
SGS148	12.8	-0.51	0.38	70
SGS150	15.6	-0.21	0.16	140

8.3.1 Homojunction Diode Characteristics

The device samples were mounted in a cryostat (ARS Cryo 4K system) and the current density – voltage (J-V) measurements were taken from room temperature down to 25K. All J-V characteristics were taken in the dark with the device shielded from ambient light. Shown in Figure 8.3 are the current density – voltage characteristics of SGS152 the 8.9% homojunction diode, for which rectification can be seen at low temperatures. The magnitude of the reverse break-down voltage at 25 K is a bit over -4 V. A good deal of both shunting (evident from the symmetry of forward and reverse characteristics at low bias) and series resistance (from the relatively high voltage at high forward current) can be seen, but the diode rectifying characteristic is evident. As the temperature is increased, the magnitude of breakdown voltage decreases, and the shunt conductance increases. Above 250 K, the device characteristics are resistor-like, with a straight line trend that is almost, but not quite symmetric across the origin. As the temperature is increased farther up to room temperature, the series resistance of this device increases, as indicated by the lower current density for the same voltage.

Figure 8.4 shows the current density – voltage characteristics of sample SGS148, the 12.8% Sn homojunction sample, which are similar to that of the previous SGS152. The reverse break-down voltage is smaller, being a bit less negative than -2.75 V. Again, above 250 K the device characteristics are resistor-like, with a straight line that is somewhat symmetric across the origin. Similar to SGS152, as the temperature is increased further up to room temperature, the series resistance of this device increases.

Figure 8.5 shows the current density – voltage characteristics of SGS150, the 15.6% Sn homojunction device sample. At all temperatures, the characteristics are

resistor-like with no clear rectification. Interestingly, the 15.6% Sn sample follows a similar trend as the lower Sn devices, in that it appears to get more conductive as the temperature increases until 250 K, at which higher temperatures result in higher resistances (slightly less current density).

Above 250 K, all samples were seen to be ohmic and non-rectifying. In addition, at these elevated temperatures, the resistance was seen to *increase* as the temperature was increased, which is a characteristic of metals, which will have increased phonon scattering at higher temperatures, rather than semiconductors, which will have increased carrier activation at higher temperatures. It could be that for these low bandgap devices the carriers are completely activated at 250 K, and increasing the temperature beyond this only results in additional phonon scattering.

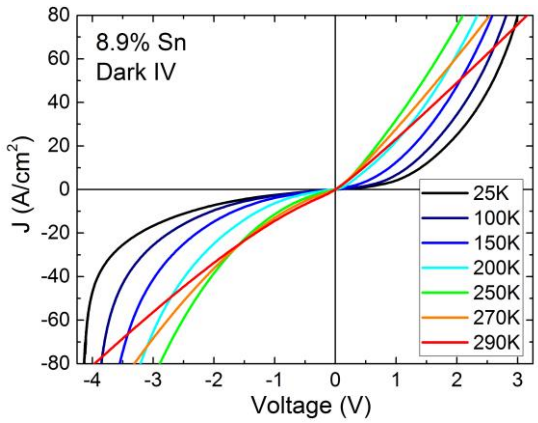

Figure 8.3: Current density – voltage characteristics in the dark of SGS152, the 8.9% homojunction device, with different measurement temperatures from 25 K to 290K. Note the trend of increasing current as the temperature increases until 250K, at which increasing temperature results in lower current.

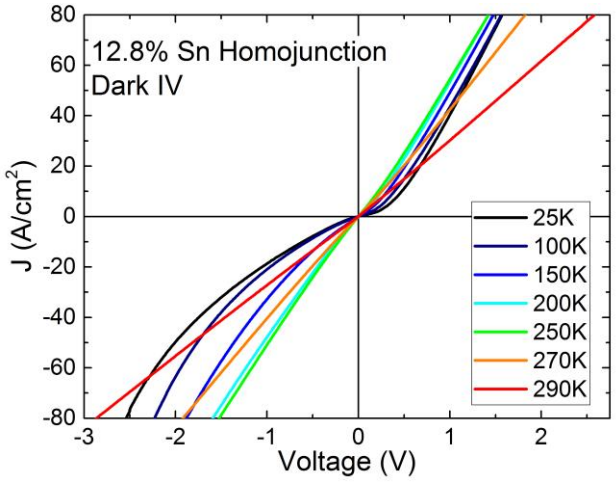

Figure 8.4: Current density – voltage characteristics of SGS148 the 12.8% homojunction sample.

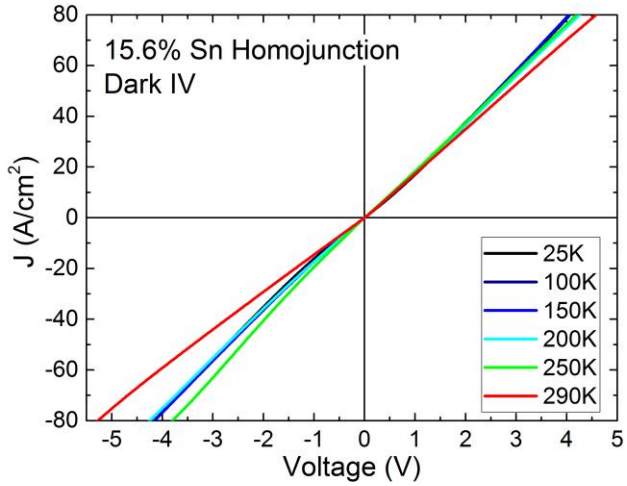

Figure 8.5: Current density – Voltage measurements of the 15.6% Sn homojunction diode as a function of temperature.

8.3.2 Homojunction Optical Response

To optically characterize the samples, a Thermo Fisher IS50r Fourier Transform Infrared Spectrometer (FTIR) interferometer was used. The IS50r was equipped with a CaF_2 beam splitter and a halogen "white-light" broadband light

source incident on the sample. The spectral characteristics of this light source can be seen in Figure 6.8. The GeSn devices exhibited a photo-response to the halogen that produced an open circuit voltage (Voc) and a short circuit current density (Jsc) as seen in Figure 8.6. The shift in the current density – voltage characteristics are subtle with illumination, as the Voc and Jsc seen in Figure 8.6 are three orders of magnitude smaller than the features shown in Figures 8.3, 8.4, and 8.5.

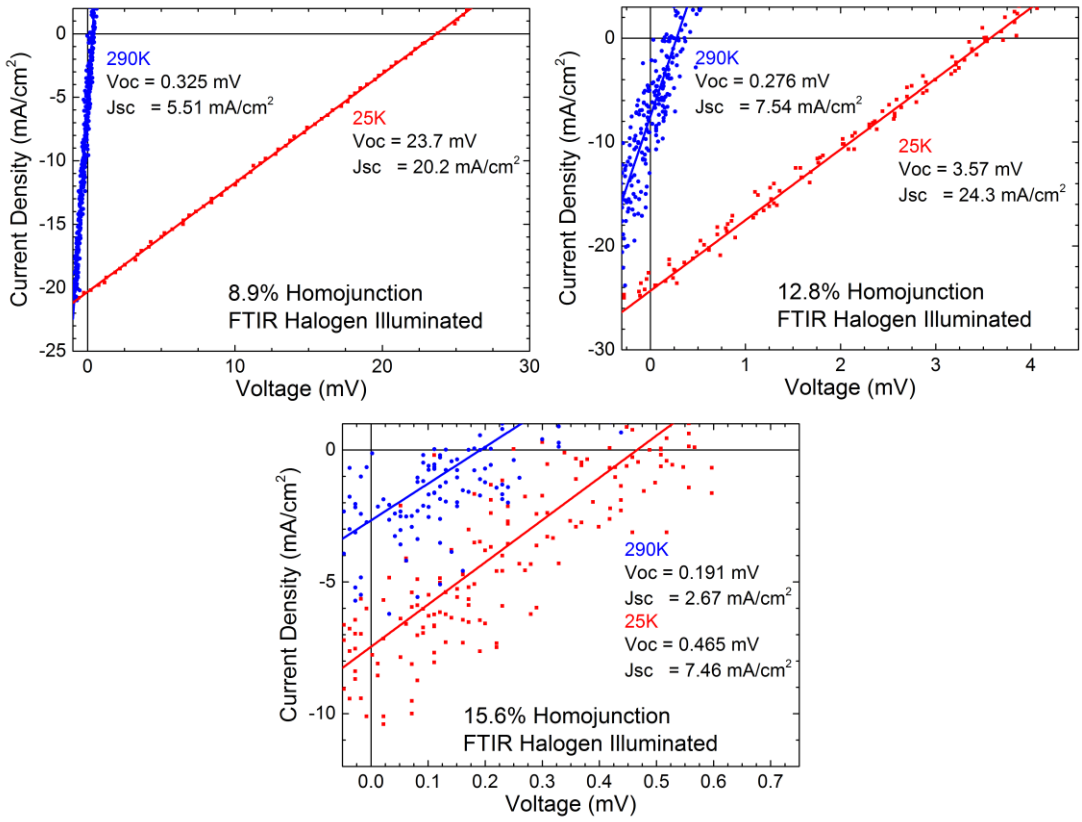

Figure 8.6: Illuminated current-voltage measurements for the GeSn homojunction samples showing the open circuit voltage and the short circuit current at 25K and 290K. Plot A) is the 8.9% device, B) is the 12.8% device, and C) is the 15.6% device. The light source was a halogen from the IS50r.

The GeSn photodiodes were attached to a photodiode transimpedance current amplifier (ThorLabs model PDA200C) and measured under short-circuit current conditions with zero bias. The FTIR halogen light was then chopped with a chopper wheel (ThorLabs MC1000) and the photodiode amplifier voltage output was connected to a lock-in amplifier that was synchronized to the chopper. The output from the lock-in was then fed into the FTIR electronics for signal processing by the FTIR software, Omnic. Measurements were taken in step-scan mode at a resolution of 4 cm^{-1}, and multiple scans of each device at each temperature were averaged in order to reduce error from random noise.

Figure 8.7 shows the normalized spectral response of the p-n homojunction device samples. For the 8.9% Sn device, the response starts at photon energies around 0.43 eV at room temperature, which is attributed to the energy band edge of the GeSn. The response shifts to lower energies, or longer wavelength, with increasing temperature, resulting in approximately a 50 meV total shift across the 265 K temperature shift. At energies higher than about 0.5 eV, the spectra are fairly flat with a slight waviness that is attributed to interference fringing from the film thickness due to light reflection. There are also slight peaks around 0.65 eV and 0.9 eV, attributed to water absorption. The 12.8% and 15.6% Sn p-n homojunction devices have a photo-response that is similar to that of the lower Sn sample, except they start at lower energies, approximately 0.4 eV and 0.3 eV for the 12.8% and 15.6% Sn devices respectively. The higher Sn content appears to have a larger shift in response with temperature; for the 12.8% Sn device approximately a 60 meV total shift across the temperature range was seen, while for the 15.6% Sn it was 70 meV. One particular feature for the higher Sn samples is that above 0.8 eV, an increase in absorption is

seen that is attributed to the Ge buffer layer. As the temperature is increased, the contribution from the Ge appears to decrease relative to the GeSn. Additionally, at temperatures higher than 175 K in the highest Sn sample, a response feature is seen at energies above 1 eV, which is attributed to the Si substrate, and it increases in relative response to the GeSn as the temperature is increased.

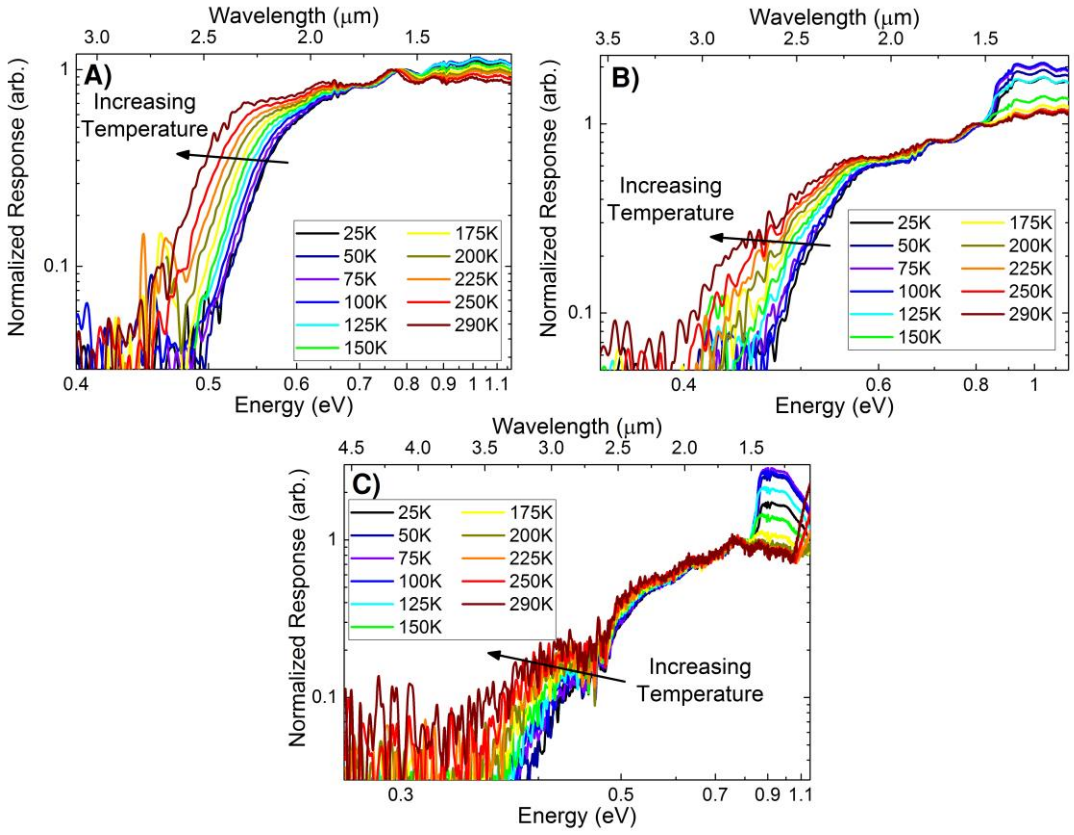

Figure 8.7: The spectral response of the GeSn homojunction samples, versus photon energy and wavelength. The data has been normalized at the energy value of 0.78eV. Clockwise from the top left, plot A) is the 8.9% Sn, B) is the 12.8% Sn, and C) is the 15.6% Sn device.

8.4 Analysis of GeSn Homojunction Optical Characteristics

The photo-generated current for a p-n junction device is a function of the photons incident on the material and the amount of those photons turned into carriers and collected that then contribute to the current. Photocurrent obeys the equation,

$$I_{photo} = \frac{q\lambda}{hc} P_{opt} EQE \tag{8.1}$$

Where I_{photo} is the photo-generated current, h is plank's constant, c is the speed of light, q is the elementary charge, λ is the wavelength of light, P_{opt} is the power of the incident light, and EQE is the external quantum efficiency. The external quantum efficiency is an important device parameter for comparison between different detectors as it indicates the efficiency of the device for converting photons into collected electrons.

The external quantum efficiency of the GeSn devices were calculated from the photo-generated current in the following way. The spectral dependence of the photo-generated current is shown in Figure 8.7. The spectral dependence of the incident power was measured utilizing the thermoelectrically cooled deuterated tryglycine sulfate (DTGS) detector in the FTIR. The thermoelectric DTGS detector has a flat spectral response, so the resulting spectra is only a function of the spectral characteristics of the halogen light source, the beam splitter, and other system components like mirrors and water absorption.

The magnitude of the FTIR halogen power spectra was initially uncalibrated, however. To calibrate the magnitude of the device response spectra, the quantum efficiency of the GeSn devices was measured at a single wavelength under illumination by a 1550 nm laser with a known power density. The active surface area of the devices was taken as the mesa area minus the area of the metal contact from

shading. The uncalibrated spectra of the GeSn photodiodes measured by the FTIR were then scaled to the quantum efficiency measured at 1550 nm using the calibrated laser. Using this calibration method, the spectrally correct FTIR spectra was calibrated, this was done for each sample at multiple temperatures and laser powers. The calibration method presented here is also covered in Section 6.3.3.

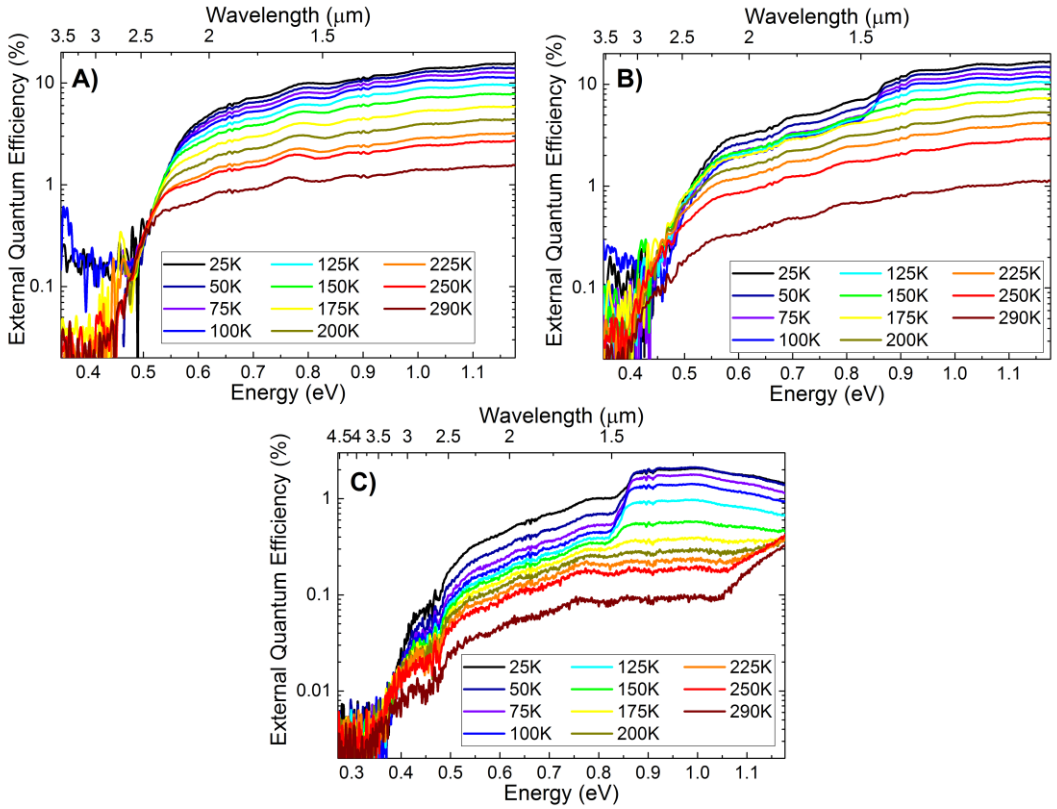

Figure 8.8: The external spectral quantum efficiency of the GeSn homojunction samples at several temperatures. Plot A) is for the 8.9% device, B) is 12.8%, and C) is the 15.6% Sn device. Note the shift in response to lower photon energies with increasing Sn content, to below 0.35 eV for the 15.6% Sn device.

The external quantum efficiency of the GeSn devices are shown in Figure 8.8. At 25K the quantum efficiency is the highest; for the two lower Sn concentrations it is about 20% while for the highest Sn concentration sample it is 2%. For all samples, the quantum efficiency decreases as the temperature is increased until at 290K the maximum response is an order of magnitude lower in each sample. The internal quantum efficiency (IQE) is related to the external quantum efficiency according to the relationship EQE = IQE (1-R), where R is the reflection from the surface. The reflection was not measured for these devices, however, the refractive index mismatch between air (n=1) and the GeSn film (n ≈ 4.5 [115]) would lead to a reflection of approximately 40%, indicating the IQE of the devices is about 60% higher than the EQE.

Above the bandgap energy, the quantum efficiency depends on the diffusion length in the material. The diffusion length affects the amount of generated carriers that are collected before they recombine. The quantum efficiency will increase as the temperature is decreased due to longer diffusion lengths caused by less scattering and by longer lifetimes for the carriers. The quantum efficiency of each of the three GeSn samples increased by an order of magnitude as the temperature was decreased from 290K to 25K, suggesting that the diffusion length is an order of magnitude larger for these samples at 25K than at room temperature. In addition, the 15.6% Sn sample has a much lower EQE, indicating a diffusion length that is about a tenth of that of the lower Sn samples.

As noted in Section 7.4, the relationship between the absorption constant and the illumination photon energy for a direct semiconductor is,

$$\alpha = \frac{\beta}{h\nu}\sqrt{h\nu - E_g} \tag{8.2}$$

where β is a constant pre-factor, hν is the photon energy, and Eg is the semiconductor bandgap energy [105]. Near the semiconductor bandgap energy, where the light absorption is small, the EQE is proportional to α [116]. Based on Equation 8.2, A plot of $(EQE * h\nu)^2$ vs energy will give a straight line relationship for a direct band-gap semiconductor, with an x-axis intercept equal to the bandgap [106]. The extracted bandgaps at room temperature for the GeSn devices are shown in Figure 8.9 and an example of the fitting technique is shown in the inset. Deformation potential theory [16] allows for calculation of the bandgap based on Sn content as well as for the residual compressive strain conditions of the films (shown in Table 8.1), calculated values are shown in Figure 8.9 and display good agreement with the extracted device bandgaps.

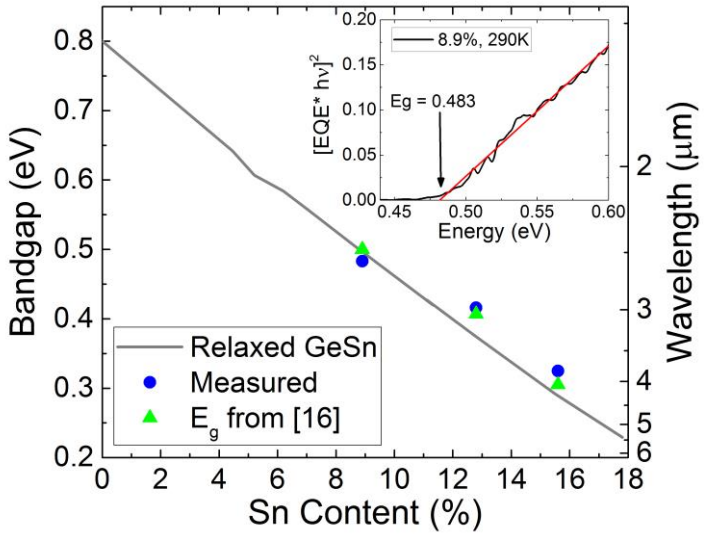

Figure 8.9: Comparison of the extracted bandgap vs Sn content measured from the spectral quantum efficiency for the GeSn homojunction devices is shown in blue. The grey line is the bandgap for relaxed GeSn with an energy gap bowing parameter of 2.42eV. The green triangles are theoretical values for the bandgap using the actual film strain conditions shown in Table 8.1 and deformation potential theory [16]. The inset shows an example of a Tauc plot [106] of the $(EQE * h\nu)^2$ vs energy with a straight line fit for the 8.9% device at 290K.

8.5 Conclusion

GeSn mid-IR photodiodes were grown, fabricated, and characterized, showing showed reasonable responsivity to wavelengths as long as 4 um. The device current-voltage characteristics were found to be rectifying at low temperatures for the lower Sn concentrations, and less rectifying (more resistor-like) for the higher Sn concentrations and for temperatures higher than 250 K. The maximum external quantum efficiency was around 10-20% at 25 K, and decreased as the temperature was increased. The highest Sn concentration sample, however, had a maximum external quantum efficiency of only 2% at 25 K. The spectral quantum efficiency was used to extract the bandgap of the films, which agreed with published theory [16]. These

photoresponse results suggest that mid-IR devices can be fabricated using Group-IV semiconductors and processing that is compatible with CMOS circuit technology.

Chapter 9

DISSERTATION CONCLUSIONS

9.1 Summary

The focus of this dissertation is on the advancement of low temperature Group IV epitaxy of tin containing alloys for use in near to mid- infrared technologies. To that end, various epitaxial techniques and improvements were made and several device structures were characterized.

The Oerlikon/ Leybold Sirius CVD-300 chemical vapor deposition system was setup with epitaxial source materials and calibrated for regular operation at the University of Delaware. The novel precursors tetrasilane and digermane were assessed for their potential for the low temperature epitaxy of crystalline silicon, crystalline silicon-germanium, and amorphous silicon films. The films were characterized using materials analysis techniques, and the deposited crystalline films were found to be bulk-like in their quality. Tin chloride was installed as a potentially commercially available tin source precursor and its viability as well as its etching capabilities were characterized. No Sn was seen incorporating into the Ge films, but it was found that the $SnCl_4$ can etch the growing Ge layers under certain conditions.

Advancements in GeSn MBE epitaxy were made including the development of novel dopants of GeSn, both p- and n-type. Low growth temperatures and high growth rates were investigated in order to achieve high Sn contents crystalline films. The growth temperature effect on the film resistivity was also investigated. The process on record (POR) recipe for Ge virtual substrates by MBE is also presented.

The Thermo Fisher Scientific iS50r FTIR infrared spectrometer was installed at the University of Delaware, in place of the previous Thermo Fisher Scientific 870 model, in order to upgrade the capabilities for analyzing the infrared characteristics of group IV semiconductors. A series of GeSn devices with Sn concentrations up to 11% from Applied Materials Corporation were fabricated into photoconductive devices and characterized optically using the FTIR, and characterized electrically using current-voltage measurements. These experiments measured the spectral photoconductivity of the GeSn devices, and revealed that the absorption edge shifted to longer wavelengths with the addition of Sn. The band edge was extracted from the spectral response, and the values were compared with other GeSn values from literature, finding the lowest energy gap closely aligned to the predicted heavy hole band transition energy by the deformation pseudopotential method. The direct bandgap of these alloys was found to be below that of bulk Ge, and fit well to theoretical values for strained GeSn. The temperature dependence of the bandgap was fit using the Varshni equation.

GeSn homojunction photodiodes were grown with MBE with Sn content up to 15.6%, and characterized electrically and optically. The devices showed diode rectification at lower temperatures, except for the highest Sn concentration sample which was Ohmic at all temperatures. The optical responsivity of the devices was measured which showed similar response for the lower Sn concentrations but a lower response for 15.6% Sn. The bandgap was extracted, finding values in the 0.4 to 0.6 eV range, which is significantly less than that of bulk Ge.

GeSn was successfully grown and characterized for near and mid-infrared detectors. The wavelength response of the material was measured to continually increase into the mid-infrared as the Sn content was increased, reaching almost 4μm at

room temperature for 15.6% Sn. The device bandgaps presented in this work are collated in Figure 9.1. While careful consideration needed to be taken into account for the growth of the material, normal clean room processing was not found to have any adverse effect on the material, paving the way for commercial manufacturability.

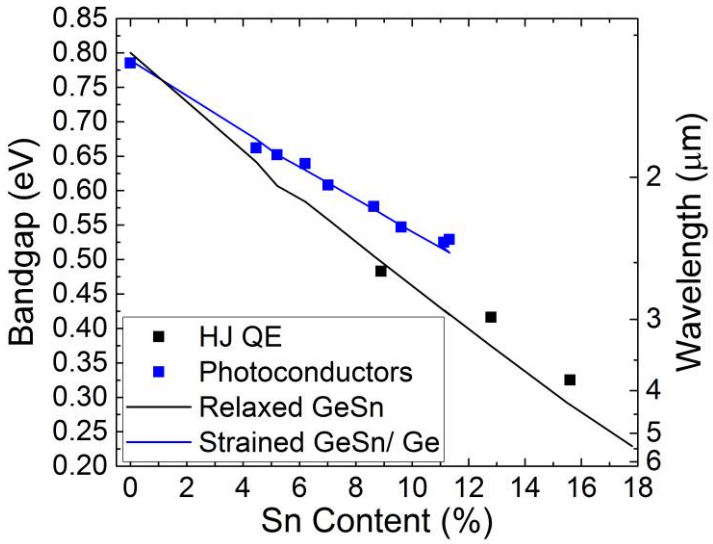

Figure 9.1: Comparison of the bandgap vs Sn content for the devices measured in this thesis (solid points). The GeSn homojunctions from Chapter 8 are mostly relaxed material, while the photoconductors from Chapter 7 were strained to the Ge substrate. Theoretical values for the bandgap from pseudopotential theory (solid lines) are from [16], showing good agreement, as well as the bandgap difference due to strain.

9.2 Future Work

In the course of any good research topic there are always additional interesting topics that arise. GeSn material was grown and characterized in this work and while it exhibited the desired infrared qualities, improvements in understanding the material

will be needed in order to create truly commercially useful devices. A few areas to focus GeSn device research moving forward are presented below.

The first is that of metallization of ohmic contacts with low contact resistance that require little, or hopefully no, annealing. The issue is primarily with achieving good contacting to n-type material. This issue has been researched at the University of Delaware to a degree and also in literature [117], [118], with most research focusing on annealing Ni contacts. Annealing to reduce contact resistance works fine for lower Sn concentrations, but keeping the thermal budget low enough to avoid Sn segregation becomes increasingly more difficult for high Sn content alloys. From experience with GeSn films at the University of Delaware, annealing >16% Sn films for any length of time at temperatures above 180^{o}C results in immediate film degradation. Likely more literature research and experimentation are needed to advance this field. Contact resistance patterns are already present on the photolithography masks used in Chapter 8 for the GeSn homojunctions, and should prove to be useful for future studies.

Another topic, which may be much more scientifically interesting, is in reaching a higher understanding of GeSn defects and growth conditions. Chapter 5 introduced some of this concept in the study of mobility of the material, doping, and substrate temperature. Two particular observations made in this dissertation require more investigation. Strained GeSn with high doping was found to have a mobility limit of 100 cm^2/V s which was independent of the doping concentration in the range measured, implicating some other mechanism than impurity scattering that is reducing the carrier lifetime. The resistivity of the material was found to shift two orders of magnitude depending on the growth temperature, likely indicating some defect associated with low temperature growth. Both of these results were discovered in this

work and will likely prove necessary to achieving high quality GeSn emitters. Hall measurements as well as photoluminescence will probably be the best avenues in this regard. The path forward for reaching higher Sn content alloys was discussed in Section 5.6, although some degradation in the device responsivity and electrical characteristics presented in Chapter 8 give rise to questions about the quality of this material.

Lastly, additional novel precursors for Sn alloys for use in the UHV-CVD would also be an interesting research topic. Tin-chloride has proven to be not useful in the ultra-high vacuum deposition environment. Perhaps various metal organic precursors like tetramethal tin, which are commercially available and have been used as doping sources for III-V's and Sn-oxide material deposition [119], [120], could prove useful in incorporating Sn if the attached carbon groups do not prove much of a problem and the chemical decomposition temperature ranges are compatible.

REFERENCES

[1] M. N. Abedin, T. F. Refaat, I. B. Bhat, Y. Xiao, S. V. Bandara, and S. D. Gunapala, "Progress of multicolor single detector to detector array development for remote sensing," in *Proc. SPIE 5543, Infrared Spaceborne Remote Sensing XII*, 2004, pp. 239–247.

[2] P. Werle, F. Slemr, K. Maurer, R. Kormann, R. Mücke, and B. Jänker, "Near- and mid-infrared laser-optical sensors for gas analysis," *Opt. Lasers Eng.*, vol. 37, no. 2–3, pp. 101–114, 2002.

[3] P. R. Norton, J. B. Campbell III, S. B. Horn, and D. A. Reago, "Third-generation infrared imagers," *Proc. SPIE 4130, Infrared Technol. Appl. XXXVI*, vol. 226, pp. 226–236, 2000.

[4] A. Hoffman, "IR DETECTORS: Semiconductor processing technology improves resolution of infrared arrays," *Laser Focus World*, no. Feb, pp. 81–84, 2006.

[5] D. J. Macdonald, M. R. Hawks, and K. C. Gross, "Passive ranging using mid-wavelength infrared atmospheric attenuation," *Proc. SPIE 7660, Infrared Technol. Appl. XXXVI*, p. 766041, 2010.

[6] R. W. Waynant, I. K. Ilev, and I. Gannot, "Mid-infrared laser applications in medicine and biology," *Philos. Trans. R. Soc. A Math. Phys. Eng. Sci.*, vol. 359, no. 1780, pp. 635–644, Mar. 2001.

[7] B. Su and G. Duan, "Research of the solar photovoltaic cells output characteristics influenced by infrared wave in the solar spectrum," in *Proc. SPIE 7854, Infrared, Millimeter Wave, and Terahertz Technologies*, 2010, p. 78541K.

[8] R. King, C. Fetzer, and P. Chiu, "Group-IV Subcells in Multijunction Concentrator Solar Cells," *ECS Trans.*, vol. 50, no. 9, pp. 287–295, 2012.

[9] R. Roucka, A. Clark, and B. Landini, "Si-Ge-Sn alloys with 1.0 eV gap for CPV multijunction solar cells," *11th Int. Conf. Conc. Photovolt. Syst.*, vol. 1679, no. 40008, pp. 1–7, 2015.

[10] G. FEVOTTE, “Applications of NIR spectroscopy to monitoring and analyzing the solid state during industrial crystallization processes,” *Int. J. Pharm.*, vol. 273, no. 1–2, pp. 159–169, Apr. 2004.

[11] R. Soref, “Mid-infrared photonics in silicon and germanium,” *Nat. Photonics*, vol. 4, no. 8, pp. 495–497, 2010.

[12] P. Moontragoon, R. a. Soref, and Z. Ikonic, “The direct and indirect bandgaps of unstrained $Si_xGe_{1-x-y}Sn_y$ and their photonic device applications,” *J. Appl. Phys.*, vol. 112, no. 7, p. 73106, 2012.

[13] G. Chang, S. Chang, and S. Chuang, “Strain-Balanced Ge_zSn_{1-z}-$Si_xGe_ySn_{1-xy}$ Multiple-Quantum-Well Lasers,” *IEEE J. Quantum Electron.*, vol. 46, no. 12, pp. 1813–1820, 2010.

[14] H. Lin, R. Chen, W. Lu, Y. Huo, T. I. Kamins, and J. S. Harris, “Structural and optical characterization of $Si_xGe_{1-x-y}Sn_y$ alloys grown by molecular beam epitaxy,” *Appl. Phys. Lett.*, vol. 100, no. 14, p. 141908, 2012.

[15] S. Gupta, B. Magyari-Köpe, Y. Nishi, and K. C. Saraswat, “Achieving direct band gap in germanium through integration of Sn alloying and external strain,” *J. Appl. Phys.*, vol. 113, no. 7, p. 73707, 2013.

[16] H. Lin, R. Chen, W. Lu, Y. Huo, T. I. Kamins, and J. S. Harris, “Investigation of the direct band gaps in $Ge_{1-x}Sn_x$ alloys with strain control by photoreflectance spectroscopy,” *Appl. Phys. Lett.*, vol. 100, no. 10, 2012.

[17] J. P. Fleurial and A. Borshchevsky, “Si-Ge-metal ternary phase diagram calculations,” *J. Electrochem. Soc.*, vol. 137, no. 9, pp. 2928–2937, 1990.

[18] S. Zaima, O. Nakatsuka, T. Yamaha, T. Asano, S. Ike, A. Suzuki, M. Kurosawa, W. Takeuchi, and M. Sakashita, “Challenges of Energy Band Engineering with New Sn-Related Group IV Semiconductor Materials for Future Integrated Circuits,” *ECS Trans.*, vol. 69, no. 10, pp. 89–98, 2015.

[19] B. Vincent, F. Gencarelli, H. Bender, C. Merckling, B. Douhard, D. H. Petersen, O. Hansen, H. H. Henrichsen, J. Meersschaut, W. Vandervorst, M. Heyns, R. Loo, and M. Caymax, “Undoped and in-situ B doped GeSn epitaxial growth on Ge by atmospheric pressure-chemical vapor deposition,” *Appl. Phys. Lett.*, vol. 99, no. 15, pp. 1–4, 2011.

[20] H. Li, Y. X. Cui, K. Y. Wu, W. K. Tseng, H. H. Cheng, and H. Chen, “Strain relaxation and Sn segregation in GeSn epilayers under thermal treatment,” *Appl. Phys. Lett.*, vol. 102, no. 25, p. 251907, 2013.

[21] R. People and J. C. Bean, "Calculation of critical layer thickness versus lattice mismatch for Ge_xSi_{1-x}/Si strained-layer heterostructures," *Appl. Phys. Lett.*, vol. 47, no. 3, p. 322, 1985.

[22] H. Pérez Ladrón De Guevara, a. G. Rodríguez, H. Navarro-Contreras, and M. a. Vidal, "$Ge_{1-x}Sn_x$ alloys pseudomorphically grown on Ge(001)," *Appl. Phys. Lett.*, vol. 83, no. 24, pp. 4942–4944, 2003.

[23] S. Wirths, R. Geiger, N. V. Den Driesch, G. Mussler, T. Stoica, S. Mantl, Z. Ikonic, M. Luysberg, S. Chiussi, J. M. Hartmann, H. Sigg, J. Faist, D. Buca, and D. Grützmacher, "Lasing in direct-bandgap GeSn alloy grown on Si," *Nat. Photonics*, vol. 9, no. 2, pp. 88–92, 2015.

[24] J. P. Gupta, N. Bhargava, S. Kim, T. Adam, and J. Kolodzey, "Infrared electroluminescence from GeSn heterojunction diodes grown by molecular beam epitaxy," *Appl. Phys. Lett.*, vol. 102, no. 25, p. 251117, 2013.

[25] C. L. Senaratne, P. M. Wallace, J. D. Gallagher, P. E. Sims, J. Kouvetakis, and J. Menéndez, "Direct gap $Ge_{1-y}Sn_y$ alloys: Fabrication and design of mid-IR photodiodes," *J. Appl. Phys.*, vol. 120, no. 2, p. 25701, 2016.

[26] S. Kim, N. Bhargava, J. Gupta, M. Coppinger, and J. Kolodzey, "Infrared photoresponse of GeSn/n-Ge heterojunctions grown by molecular beam epitaxy.," *Opt. Express*, vol. 22, no. 9, pp. 11029–34, 2014.

[27] J. Hart, R. Hazbun, J. Nakos, D. Siegel, C. Funch, J. Kolodzey, and D. Harame, "Morphological instability of high Ge percent SiGe films grown by ultra-high vacuum chemical vapor deposition," *ECS Trans.*, vol. 64, no. 6, pp. 659–667, 2014.

[28] R. Hazbun, J. Hart, J. Nakos, D. Siegel, C. Funch, V. Kaushal, S. Hazel, and J. Kolodzey, "The Use of Dopants for Defect Monitoring for Silicon-Germanium Ultra-High Vacuum Chemical Vapor Deposition," *ECS Trans.*, vol. 64, no. 6, pp. 441–454, 2014.

[29] M. Coppinger, J. Hart, N. Bhargava, S. Kim, and J. Kolodzey, "Photoconductivity of germanium tin alloys grown by molecular beam epitaxy," *Appl. Phys. Lett.*, vol. 102, no. 14, p. 141101, 2013.

[30] R. Hazbun, J. Hart, R. Hickey, A. Ghosh, N. Fernando, S. Zollner, T. N. Adam, and J. Kolodzey, "Silicon epitaxy using tetrasilane at low temperatures in ultra-high vacuum chemical vapor deposition," *J. Cryst. Growth*, vol. 444, pp. 21–27, Jun. 2016.

[31] G. Ghidini and F. W. Smith, "Interaction of H_2O with Si(111) and (100)," *J. Electrochem. Soc.*, vol. 131, no. 12, p. 2924, 1984.

[32] B. Meyerson, "UHV/CVD growth of Si and Si: Ge alloys: chemistry, physics, and device applications," *Proc. IEEE*, vol. 80, pp. 1592–1608, 1992.

[33] K. Chung, "Silicon-Based Epitaxy by Chemical Vapor Deposition Using Novel Precursor Neopentasilane," Princeton, 2010.

[34] C. L. Yaws, P. K. Narasimhan, and C. Gabbula, *Yaws' Handbook of Antoine Coefficients for Vapor Pressure*, 2nd Editio. Knovel, 2009.

[35] H. Emeléus and A. Maddock, "251. The chemistry of the higher silanes. Part I. Tetrasilane," *J. Chem. Soc. (...*, pp. 5–8, 1946.

[36] M. Bauer, C. Ritter, P. a. Crozier, J. Ren, J. Menendez, G. Wolf, and J. Kouvetakis, "Synthesis of ternary SiGeSn semiconductors on Si(100) via Sn_xGe_{1-x} buffer layers," *Appl. Phys. Lett.*, vol. 83, no. 11, pp. 2163–2165, 2003.

[37] S. Wirths, D. Buca, G. Mussler, a. T. Tiedemann, B. Holländer, P. Bernardy, T. Stoica, D. Grützmacher, and S. Mantl, "Reduced Pressure CVD Growth of Ge and $Ge_{1-x}Sn_x$ Alloys," *ECS J. Solid State Sci. Technol.*, vol. 2, no. 5, pp. N99–N102, 2013.

[38] G. W. Gale, K. a Reinhardt, and R. J. Small, *PART II - Aqueous Cleaning and Surface Conditioning Processes*. 2008.

[39] S. W. Bedell, T. N. Adam, A. Turansky, and D. K. Sadana, "Role of interfacial oxygen on the quality and strain stability of pseudomorphic silicon-germanium layers grown on Si substrates," *J. Cryst. Growth*, vol. 316, no. 1, pp. 101–105, 2011.

[40] P. Brabant, J. Ferrara, B. Pagliaro, K. Weeks, M. Rittgers, R. Scott, Y. Zhang, T. Landin, T. Irving, J. Spear, J. Italiano, and S. G. Thomas, "Hydrogen termination for extended queue times for low temperature epitaxy," *Appl. Surf. Sci.*, vol. 255, no. 5, pp. 1741–1743, 2008.

[41] T. Adam, S. Bedell, and a Reznicek, "Low-temperature epitaxial Si, SiGe, and SiC in a 300mm UHV/CVD reactor," *ECS Trans.*, vol. 33, no. 6, pp. 149–154, 2010.

[42] D. L. Harame, J. H. Comfort, J. D. Cressler, E. F. CrabbC, J. Y.-C. Sun, B. S. Meyerson, and T. Tice, "Si/SiGe Epitaxial-Base Transistors-Part I: Materials, Physics, and Circuits," *IEEE Trans. Electron Devices*, vol. 42, no. 3, pp. 455–

468, 1995.

[43] K. Kurishima, “An analytic expression of f max for HBTs,” *Electron Devices, IEEE Trans.*, vol. 43, no. 12, p. 2074, 1996.

[44] H. Kroemer, “Two integral relations pertaining to the electron transport through a bipolar transistor with a nonuniform energy gap in the base region,” *Solid. State. Electron.*, 1985.

[45] A. Cullis, D. Robbins, A. Pidduck, and P. Smith, “The characteristics of strain-modulated surface undulations formed upon epitaxial $Si_{1-x}Ge_x$ alloy layers on Si,” *J. Cryst. Growth*, vol. 123, p. 333, 1992.

[46] D. Perovic, B. Bahierathan, H. Lafontaine, D. C. Houghton, and D. W. McComb, “Kinetic critical thickness for surface wave instability vs. misfit dislocation formation in Ge_xSi_{1-x}/Si (100) heterostructures,” *Phys. A Stat. …*, vol. 239, pp. 11–17, 1997.

[47] R. Tromp, F. Ross, and M. Reuter, “Instability-driven SiGe island growth,” *Phys. Rev. Lett.*, vol. 84, no. 20, pp. 4641–4, May 2000.

[48] B. Spencer, P. Voorhees, and J. Tersoff, “Morphological instability theory for strained alloy film growth: The effect of compositional stresses and species-dependent surface mobilities on ripple formation during epitaxial film deposition,” *Phys. Rev. B*, vol. 64, no. 23, p. 235318, Nov. 2001.

[49] B. J. Spencer, P. W. Voorhees, and S. H. Davis, “Morphological Instability in Epitxially Strained Dislocation-Free Solid Films,” *Phys. Rev. Lett.*, vol. 67, no. 26, pp. 3696–3699, 1991.

[50] M. Liehr, C. M. Greenlief, S. R. Kasi, and M. Offenberg, “Kinetics of silicon epitaxy using SiH4 in a rapid thermal chemical vapor deposition reactor,” *Appl. Phys. Lett.*, vol. 56, no. 7, p. 629, 1990.

[51] H. Yang, X. Zhang, Z. Jiang, X. Lu, L. Bai, X. Yang, Y. Fan, D. Hu, Y. Sun, and W. Huang, “The influence of the edge effect of the mask on the strain and the morphology of SiGe film grown at the patterned Si substrate by molecular beam epitaxy,” *Thin Solid Films*, vol. 514, no. 1–2, pp. 344–349, 2006.

[52] G. S. Kar, S. Kiravittaya, U. Denker, B.-Y. Nguyen, and O. G. Schmidt, “Strain distribution in a transistor using self-assembled SiGe islands in source and drain regions,” *Appl. Phys. Lett.*, vol. 88, no. 25, p. 253108, 2006.

[53] A. I. Yakimov, A. V. Dvurechenskii, and A. I. Nikiforov, “Germanium Self-

Assembled Quantum Dots in Silicon for Nano- and Optoelectronics," *J. Nanoelectron. Optoelectron.*, vol. 1, no. 2, p. 119, 2006.

[54] S. E. Thompson, M. Armstrong, C. Auth, M. Alavi, M. Buehler, R. Chau, S. Cea, T. Ghani, G. Glass, T. Hoffman, C. H. Jan, C. Kenyon, J. Klaus, K. Kuhn, Z. Ma, B. Mcintyre, K. Mistry, A. Murthy, B. Obradovic, R. Nagisetty, P. Nguyen, S. Sivakumar, R. Shaheed, L. Shifren, B. Tufts, S. Tyagi, M. Bohr, and Y. El-Mansy, "A 90-nm logic technology featuring strained-silicon," *IEEE Trans. Electron Devices*, vol. 51, no. 11, pp. 1790–1797, 2004.

[55] N. Sugiyama, "High concentration n-type doping in Si layers epitaxially grown by ultra-high vacuum chemical vapor deposition with cracking heater," *J. Cryst. Growth*, vol. 172, no. 3–4, pp. 376–380, 1997.

[56] T. N. Adam, S. Bedell, A. Reznicek, D. K. Sadana, A. Venkateshan, T. Tsunoda, T. Seino, J. Nakatsuru, and S. R. Shinde, "300mm cold-wall UHV/CVD reactor for low-temperature epitaxial (100) silicon," *ECS Trans.*, vol. 33, no. 6, pp. 595–602, 2010.

[57] J. Sturm and K. Chung, "Chemical vapor deposition epitaxy of silicon-based materials using neopentasilane," *ECS Trans.*, vol. 16, no. 10, pp. 799–805, 2008.

[58] J. D. Gallagher, C. Xu, L. Jiang, J. Kouvetakis, and J. Menéndez, "Fundamental band gap and direct-indirect crossover in $Ge_{1-x-y}Si_xSn_y$ alloys," *Appl. Phys. Lett.*, vol. 103, no. 20, pp. 2011–2016, 2013.

[59] S. Gupta, V. Moroz, S. Lee, Q. Lu, and K. C. Saraswat, "7-nm FinFET CMOS design enabled by stress engineering using Si, Ge, and Sn," *IEEE Trans. Electron Devices*, vol. 61, no. 5, pp. 1222–1230, 2014.

[60] C. Ventura, J. Querales Flores, J. Fuhr, and R. Barrio, "Electronic structure of $Ge_{1-x-y}Si_xSn_y$ ternary alloys for multijunction solar cells," *Prog. Photovoltaics Res. Appl.*, vol. 23, pp. 112–118, 2015.

[61] G. Sun, R. A. Soref, and H. H. Cheng, "Design of a Si-based lattice-matched room-temperature GeSn/GeSiSn multi-quantum-well mid-infrared laser diode.," *Opt. Express*, vol. 18, no. 19, pp. 19957–65, Sep. 2010.

[62] S. Zollner, J. Hildreth, and R. Liu, "Optical constants and ellipsometric thickness determination of strained $Si_{1-x}Ge_x$: C layers on Si (100) and related heterostructures," *J. Appl. Phys.*, vol. 88, no. 7, pp. 4102–4108, 2000.

[63] D. E. Aspnes, A. A. Studna, and E. Kinsbron, "Dielectric Properties of Heavily

Doped Crystalline and Amorphous Silicon from 1.5 to 6.0~eV," *Phys. Rev. B*, vol. 29, no. 2, p. 768, 1984.

[64] D. Nečas and P. Klapetek, "Gwyddion: an open-source software for SPM data analysis," *Cent. Eur. J. Phys.*, vol. 10, no. 1, p. 181, 2012.

[65] A. Gouyé, O. Kermarrec, A. Halimaoui, Y. Campidelli, D. Rouchon, M. Burdin, P. Holliger, and D. Bensahel, "Low-temperature RPCVD of Si, SiGe alloy, and $Si_{1-y}C_y$ films on Si substrates using trisilane (Silcore®)," *J. Cryst. Growth*, vol. 311, no. 13, pp. 3522–3527, 2009.

[66] F. Gencarelli, B. Vincent, L. Souriau, O. Richard, W. Vandervorst, R. Loo, M. Caymax, and M. Heyns, "Low-temperature Ge and GeSn Chemical Vapor Deposition using Ge_2H_6," *Thin Solid Films*, vol. 520, no. 8, pp. 3211–3215, 2012.

[67] T. R. Bramblett, Q. Lu, N.-E. Lee, N. Taylor, M.-A. Hasan, and J. E. Greene, "Ge(001) gas-source molecular beam epitaxy on Ge(001)2x1 and Si(00l)2x1 from Ge_2H_6: Growth kinetics and surface roughening," *J. Appl. Phys.*, vol. 77, no. 1, p. 1504, 1995.

[68] M. Liehr, C. M. Greenlief, S. R. Kasi, and M. Offenberg, "Kinetics of silicon epitaxy using SiH_4 in a rapid thermal chemical vapor deposition reactor," *Appl. Phys. Lett.*, vol. 56, no. 7, p. 629, 1990.

[69] W. B. De Boer and D. J. Meyer, "Low-temperature chemical vapor deposition of epitaxial Si and SiGe layers at atmospheric pressure," *Appl. Phys. Lett.*, vol. 58, no. 12, pp. 1286–1288, 1991.

[70] Q. Lu, M. R. Sardela, T. R. Bramblett, and J. E. Greene, "B-doped fully strained $Si_{1-x}Ge_x$ layers grown on Si(001) by gas-source molecular beam epitaxy from Si_2H_6, Ge_2H_6, and B_2H_6: Charge transport properties," *J. Appl. Phys.* , vol. 80, no. 8, pp. 4458–4466, 1996.

[71] B. M. H. Ning and J. E. Crowell, "The effect of germanium on the desorption of hydrogen from Si(100)," *Surface Science Letters*, vol. 295. p. A691, 1993.

[72] S. W. Bedell, D. K. Sadana, K. Fogel, H. Chen, and A. Domenicucci, "Quick turnaround technique for highlighting defects in thin Si/SiGe bilayers," *Electrochemical and Solid-State Letters*, vol. 7, no. 5. p. G105, 2004.

[73] M. Shinriki, K. Chung, S. Hasaka, P. Brabant, H. He, T. N. Adam, and D. Sadana, "Gas phase particle formation and elimination on Si (100) in low temperature reduced pressure chemical vapor deposition silicon-based epitaxial

layers," *Thin Solid Films*, vol. 520, no. 8, pp. 3190–3194, 2012.

[74] S.-J. Kahng, Y. Ha, J.-Y. Park, S. Kim, D. Moon, and Y. Kuk, "Hydrogen-Surfactant Mediated Growth of Ge on Si(001)," *Phys. Rev. Lett.*, vol. 80, no. 22, pp. 4931–4934, Jun. 1998.

[75] A. Mosleh, M. a. Alher, L. C. Cousar, W. Du, S. A. Ghetmiri, T. Pham, J. M. Grant, G. Sun, R. a. Soref, B. Li, H. a. Naseem, and S.-Q. Yu, "Direct Growth of $Ge_{1-x}Sn_x$ Films on Si Using a Cold-Wall Ultra-High Vacuum Chemical-Vapor-Deposition System," *Front. Mater.*, vol. 2, no. April, pp. 1–7, 2015.

[76] J. Liu, X. Sun, R. Camacho-Aguilera, L. C. Kimerling, and J. Michel, "Ge-on-Si laser operating at room temperature.," *Opt. Lett.*, vol. 35, no. 5, pp. 679–81, Mar. 2010.

[77] T. K. P. Luong, A. Ghrib, M. T. Dau, M. A. Zrir, M. Stoffel, V. Le Thanh, R. Daineche, T. G. Le, V. Heresanu, O. Abbes, M. Petit, M. El Kurdi, P. Boucaud, H. Rinnert, and J. Murota, "Molecular-beam epitaxial growth of tensile-strained and n-doped Ge/Si(001) films using a GaP decomposition source," *Thin Solid Films*, vol. 557, pp. 70–75, Apr. 2014.

[78] G. Lippert, H. J. Osten, D. Krüger, P. Gaworzewski, and K. Eberl, "Heavy phosphorus doping in molecular beam epitaxial grown silicon with a GaP decomposition source," *Appl. Phys. Lett.*, vol. 66, no. 23, p. 3197, 1995.

[79] M. Dashiell, R. Troeger, S. Rommel, T. N. Adam, P. R. Berger, C. Guedj, J. Kolodzey, A. C. Seabaugh, and R. Lake, "Current-voltage characteristics of high current density silicon Esaki diodes grown by molecular beam epitaxy and the influence of thermal annealing," *IEEE Trans. Electron Devices*, vol. 47, no. 9, pp. 1707–1714, 2000.

[80] G. Lippert, H. J. Osten, and D. Krüger, "Phosphorus doping in molecular beam epitaxial grown silicon and silicon/germanium using a GaP decomposition source," *J. Cryst. Growth*, vol. 157, no. 1–4, pp. 304–307, 1995.

[81] N. V. Den Driesch, D. Stange, S. Wirths, D. Rainko, G. Mussler, and P. Gr, "Direct bandgap GeSn light emitting diodes for short-wave infrared applications grown on Si," *SPIE Photonics West*, vol. 9752, pp. 1–9, 2016.

[82] J. Mathews, R. Roucka, J. Xie, S.-Q. Yu, J. Menéndez, and J. Kouvetakis, "Extended performance GeSn/Si(100) p-i-n photodetectors for full spectral range telecommunication applications," *Appl. Phys. Lett.*, vol. 95, no. 13, p. 133506, 2009.

[83] Y. Shimura, S. Takeuchi, O. Nakatsuka, B. Vincent, F. Gencarelli, T. Clarysse, W. Vandervorst, M. Caymax, R. Loo, A. Jensen, D. H. Petersen, and S. Zaima, "In-situ Ga doping of fully strained $Ge_{1-x}Sn_x$ heteroepitaxial layers grown on Ge(001) substrates," *Thin Solid Films*, vol. 520, no. 8, pp. 3206–3210, 2012.

[84] W. Wang, S. Vajandar, S. L. Lim, Y. Dong, V. R. D'Costa, T. Osipowicz, E. S. Tok, and Y.-C. Yeo, "In-situ gallium-doping for forming p+ germanium-tin and application in germanium-tin p-i-n photodetector," *J. Appl. Phys.*, vol. 119, no. 15, p. 155704, Apr. 2016.

[85] S. Kim, J. Gupta, N. Bhargava, M. Coppinger, and J. Kolodzey, "Current-voltage characteristics of GeSn/Ge heterojunction diodes grown by molecular beam epitaxy," *IEEE Electron Device Lett.*, vol. 34, no. 10, pp. 1217–1219, 2013.

[86] J. Werner, M. Oehme, M. Schmid, M. Kaschel, a. Schirmer, E. Kasper, and J. Schulze, "Germanium-tin p-i-n photodetectors integrated on silicon grown by molecular beam epitaxy," *Appl. Phys. Lett.*, vol. 98, no. 6, p. 61108, 2011.

[87] N. Bhargava, M. Coppinger, J. Prakash Gupta, L. Wielunski, and J. Kolodzey, "Lattice constant and substitutional composition of GeSn alloys grown by molecular beam epitaxy," *Appl. Phys. Lett.*, vol. 103, no. 4, p. 41908, 2013.

[88] H. Okumura, T. Akane, and S. Matsumoto, "Carbon contamination free Ge(100) surface cleaning for MBE," *Appl. Surf. Sci.*, vol. 125, no. 1, pp. 125–128, 1998.

[89] W.-X. Ni, K. Lyutovich, J. Alami, C. Tengstedt, M. Bauer, and E. Kasper, "X-ray reciprocal space mapping studies of strain relaxation in thin SiGe layers (100 nm) using a low temperature growth step," *J. Cryst. Growth*, vol. 227–228, pp. 756–760, Jul. 2001.

[90] Evans Analytical Group, www.eag.com.

[91] V. P. Kesan, S. S. Iyer, and J. M. Cotte, "Dopant incorporation in epitaxial germanium grown on Ge(100) substrates by MBE," *J. Cryst. Growth*, vol. 111, no. 1–4, pp. 847–855, 1991.

[92] D. H. Dickey, "Developments in ultrashallow spreading resistance analysis," *J. Vac. Sci. Technol. B Microelectron. Nanom. Struct.*, vol. 20, no. 1, p. 467, 2002.

[93] J. D. Sau and M. L. Cohen, "Possibility of increased mobility in Ge-Sn alloy system," *Phys. Rev. B*, vol. 75, no. 4, p. 45208, 2007.

[94] C. Schulte-Braucks, S. Glass, E. Hofmann, D. Stange, N. von den Driesch, Q. T. Zhao, D. Buca, S. Mantl, J. M. Hartmann, and Z. Ikonic, "Process modules for GeSn nanoelectronics with high Sn-contents," in *2016 Joint International EUROSOI Workshop and International Conference on Ultimate Integration on Silicon (EUROSOI-ULIS)*, 2016, vol. 9, no. 619509, pp. 24–27.

[95] D. B. Cuttriss, "Relation Between Surface Concentration and Average Conductivity in Diffused Layers in Germanium," *Bell Syst. Tech. J.*, vol. 40, no. 2, p. 509, 1961.

[96] O. Nakatsuka, N. Tsutsui, Y. Shimura, S. Takeuchi, A. Sakai, and S. Zaima, "Mobility Behavior of $Ge_{1-x}Sn_x$ Layers Grown on Silicon-on-Insulator Substrates," *Jpn. J. Appl. Phys.*, vol. 49, no. 4, p. 04DA10, Apr. 2010.

[97] J. Werner, M. Oehme, M. Schmid, M. Kaschel, A. Schirmer, E. Kasper, and J. Schulze, "Germanium-tin p-i-n photodetectors integrated on silicon grown by molecular beam epitaxy," *Appl. Phys. Lett.*, vol. 98, no. 6, p. 61108, 2011.

[98] A. A. Michelson, "On the application of interference-methods to spectroscopic measurements," *Phil. Mag.*, vol. 31, no. 5, p. 256, 1891.

[99] A. Gassenq, F. Gencarelli, J. Van Campenhout, Y. Shimura, R. Loo, G. Narcy, B. Vincent, and G. Roelkens, "GeSn/Ge heterostructure short-wave infrared photodetectors on silicon.," *Opt. Express*, vol. 20, no. 25, pp. 27297–303, Dec. 2012.

[100] B. R. Conley, J. Margetis, W. Du, H. Tran, A. Mosleh, S. A. Ghetmiri, J. Tolle, G. Sun, R. Soref, B. Li, H. A. Naseem, and S. Q. Yu, "Si based GeSn photoconductors with a 1.63 A/W peak responsivity and a 2.4 μm long-wavelength cutoff," *Appl. Phys. Lett.*, vol. 105, no. 22, p. 221117, Dec. 2014.

[101] M. Medikonda, G. R. Muthinti, R. Vasić, T. N. Adam, A. Reznicek, M. Wormington, G. Malladi, Y. Kim, Y.-C. Huang, and A. C. Diebold, "Optical properties of pseudomorphic $Ge_{1-x}Sn_x$ (x = 0 to 0.11) alloys on Ge(001)," *J. Vac. Sci. Technol. B, Nanotechnol. Microelectron. Mater. Process. Meas. Phenom.*, vol. 32, no. 6, p. 61805, Nov. 2014.

[102] K. Ye, W. Zhang, M. Oehme, M. Schmid, M. Gollhofer, K. Kostecki, D. Widmann, R. Körner, E. Kasper, and J. Schulze, "Absorption coefficients of GeSn extracted from PIN photodetector response," *Solid. State. Electron.*, vol. 110, pp. 71–75, 2015.

[103] C. Schulte-Braucks, D. Stange, N. von den Driesch, S. Blaeser, Z. Ikonic, J. M. Hartmann, S. Mantl, and D. Buca, "Negative differential resistance in direct

bandgap GeSn p-i-n structures," *Appl. Phys. Lett.*, vol. 107, no. 4, p. 42101, 2015.

[104] O. Madelung, *Semiconductors: Data Handbook*, 3rd ed. Heidelberg: Springer, 2004.

[105] N. Peyghambarian, S. W. Koch, and A. Mysyrowicz, *Introduction to Semiconductor Optics*. Englewood Cliffs: Prentice Hall, 1993.

[106] J. Tauc, "Optical properties and electronic structure of amorphous Ge and Si," *Mater. Res. Bull.*, vol. 3, no. 1, pp. 37–46, Jan. 1968.

[107] G. G. Macfarlane, T. P. McLean, J. E. Quarrington, and V. Roberts, "Fine Structure in the Absorption-Edge Spectrum of Ge," *Phys. Rev.*, vol. 108, no. 6, pp. 1377–1383, Dec. 1957.

[108] H. Lin, R. Chen, W. Lu, Y. Huo, T. I. Kamins, and J. S. Harris, "Investigation of the direct band gaps in $Ge_{1-x}Sn_x$ alloys with strain control by photoreflectance spectroscopy," *Appl. Phys. Lett.*, vol. 100, no. 10, p. 102109, 2012.

[109] Y. P. Varshni, "Temperature Dependence of the Energy Gap in Semiconductors," *Physica*, vol. 34, no. 1, p. 149, 1967.

[110] B. Conley, A. Mosleh, and S. Ghetmiri, "Temperature dependent spectral response and detectivity of GeSn photoconductors on silicon for short wave infrared detection," *Opt. Express*, vol. 22, no. 13, pp. 15639–15652, 2014.

[111] M. Oehme, K. Kostecki, M. Schmid, F. Oliveira, E. Kasper, and J. Schulze, "Epitaxial growth of strained and unstrained GeSn alloys up to 25% Sn," *Thin Solid Films*, vol. 557, pp. 169–172, 2014.

[112] D. Grutzmacher, D. Stange, N. von den Driesch, S. Wirths, S. Mantl, D. M. Buca, J. M. Hartmann, R. Geiger, and H. Sigg, "On the track towards an electrically pumped group IV laser," in *2016 IEEE Silicon Nanoelectronics Workshop (SNW)*, 2016, vol. 327, no. 2005, pp. 124–125.

[113] J. Hart, T. Adam, Y. Kim, Y.-C. Huang, A. Reznicek, R. Hazbun, J. Gupta, and J. Kolodzey, "Temperature varying photoconductivity of GeSn alloys grown by chemical vapor deposition with Sn concentrations from 4% to 11%," *J. Appl. Phys.*, vol. 119, no. 9, p. 93105, 2016.

[114] A. Rogalski, *Infrared Detectors*, 2nd Ed. CRC Press, 2011.

[115] V. Richard D'Costa, W. Wang, Q. Zhou, E. Soon Tok, and Y. C. Yeo, "Above-bandgap optical properties of biaxially strained GeSn alloys grown by molecular beam epitaxy," *Appl. Phys. Lett.*, vol. 104, no. 2, pp. 2012–2016, 2014.

[116] M. A. Contreras, L. M. Mansfield, B. Egaas, J. Li, M. Romero, R. Noufi, E. Rudiger-voigt, and W. Mannstadt, "Wide Bandgap Cu(In,Ga)Se_2 solar cells with improved energy conversion efficiency," *Prog. Photovolt Res. Appl.*, vol. 15, no. February 2013, pp. 659–676, 2007.

[117] X. Zhang, D. Zhang, J. Zheng, Z. Liu, C. He, C. Xue, G. Zhang, C. Li, B. Cheng, and Q. Wang, "Formation and characterization of Ni/Al Ohmic contact on n+-type GeSn," *Solid. State. Electron.*, vol. 114, pp. 178–181, 2015.

[118] S. Wirths, R. Troitsch, G. Mussler, J.-M. Hartmann, P. Zaumseil, T. Schroeder, S. Mantl, and D. Buca, "Ternary and quaternary Ni(Si)Ge(Sn) contact formation for highly strained Ge p- and n-MOSFETs," *Semicond. Sci. Technol.*, vol. 30, no. 5, p. 55003, 2015.

[119] J. D. Parsons and F. G. Krajenbrink, "Tin Doping of Gallium Arsenide by Metal Organic Chemical Vapor Deposition (MOCVD)," *J. Electrochem. Soc.* , vol. 130, no. 8, pp. 1780–1781, 1983.

[120] Z. Zhao, D. . Morel, and C. . Ferekides, "Electrical and optical properties of tin-doped CdO films deposited by atmospheric metalorganic chemical vapor deposition," *Thin Solid Films*, vol. 413, no. 1–2, pp. 203–211, 2002.

Appendix A

PERMISSIONS TO PUBLISH

The following copyright holders have granted permission to publish:

Figures 1.5 and 1.6 are published with permission from the Journal of Applied Physics. Originally published in Volume 113(7), page 73707 in 2013.

AIP PUBLISHING LLC LICENSE TERMS AND CONDITIONS

Dec 11, 2016

This Agreement between John T Hart ("You") and AIP Publishing LLC ("AIP Publishing LLC") consists of your license details and the terms and conditions provided by AIP Publishing LLC and Copyright Clearance Center.

License Number	4006220239282
License date	Dec 11, 2016
Licensed Content Publisher	AIP Publishing LLC
Licensed Content Publication	Journal of Applied Physics
Licensed Content Title	Achieving direct band gap in germanium through integration of Sn alloying and external strain
Licensed Content Author	Suyog Gupta,Blanka Magyari-Köpe,Yoshio Nishi, et al.
Licensed Content Date	Feb 19, 2013
Licensed Content Volume Number	113
Licensed Content Issue Number	7
Type of Use	Thesis/Dissertation
Requestor type	Student
Format	Print and electronic
Portion	Figure/Table
Number of figures/tables	2
Title of your thesis / dissertation	THE GROWTH AND CHARACTERIZATION OF GROUP IV ALLOYS FOR NEAR TO MID-INFRARED DETECTORS
Expected completion date	Jan 2017
Estimated size (number of pages)	194
Requestor Location	John T Hart 140 Evans Hall University of Delaware NEWARK, DE 19711 United States Attn: John T Hart
Billing Type	Invoice
Billing Address	John T Hart 140 Evans Hall University of Delaware NEWARK, DE 19711 United States Attn: John T Hart
Total	0.00 USD
Terms and Conditions	

Figures in Chapter 4 were originally published in the Journal of Crystal Growth, Volume 444, Pages 21–27 in 2016 as well as in Thin Solid Films, Volume 604, Pages 23–27 in 2016.

ELSEVIER LICENSE
TERMS AND CONDITIONS

Dec 11, 2016

This Agreement between John T Hart ("You") and Elsevier ("Elsevier") consists of your license details and the terms and conditions provided by Elsevier and Copyright Clearance Center.

License Number	4006191289136
License date	Dec 11, 2016
Licensed Content Publisher	Elsevier
Licensed Content Publication	Journal of Crystal Growth
Licensed Content Title	Silicon epitaxy using tetrasilane at low temperatures in ultra-high vacuum chemical vapor deposition
Licensed Content Author	Ramsey Hazbun,John Hart,Ryan Hickey,Ayana Ghosh,Nalin Fernando,Stefan Zollner,Thomas N Adam,James Kolodzey
Licensed Content Date	15 June 2016
Licensed Content Volume Number	444
Licensed Content Issue Number	n/a
Licensed Content Pages	7
Start Page	21
End Page	27
Type of Use	reuse in a thesis/dissertation
Intended publisher of new work	other
Portion	figures/tables/illustrations
Number of figures/tables/illustrations	6
Format	both print and electronic
Are you the author of this Elsevier article?	Yes
Will you be translating?	No
Order reference number	
Original figure numbers	Fig. 1, Fig. 2, Fig. 3, Fig. 5, Fig. 6, & Fig. 7
Title of your thesis/dissertation	THE GROWTH AND CHARACTERIZATION OF GROUP IV ALLOYS FOR NEAR TO MID-INFRARED DETECTORS
Expected completion date	Jan 2017
Estimated size (number of pages)	194
Elsevier VAT number	GB 494 6272 12
Requestor Location	John T Hart 140 Evans Hall University of Delaware

Copyright Clearance Center

Confirmation Number: 11606041
Order Date: 11/16/2016

Customer Information

Customer: John Hart
Account Number: 3001006071
Organization: John Hart
Email: hartjt@udel.edu
Phone: +1 (720)5602745
Payment Method: Invoice

This is not an invoice

Order Details

Thin solid films

Billing Status: **N/A**

Order detail ID:	70165016
ISSN:	0040-6090
Publication Type:	Journal
Volume:	
Issue:	
Start page:	
Publisher:	ELSEVIER S.A.

Permission Status: **Granted**
Permission type: Republish or display content
Type of use: Thesis/Dissertation
Order License Id: 3990930737334

Requestor type	Academic institution
Format	Print, Electronic
Portion	chart/graph/table/figure
Number of charts/graphs/tables/figures	5
Title or numeric reference of the portion(s)	Hart, J., Hazbun, R., Eldridge, D., Hickey, R., Fernando, N., Adam, T., ... Kolodzey, J. (2016). . Thin Solid Films, 604, 23–27. http://doi.org/10.1016/j.tsf.2016.03.010
Title of the article or chapter the portion is from	Tetrasilane and digermane for the Ultra-high vacuum chemical vapor deposition of SiGe alloys
Editor of portion(s)	N/A
Author of portion(s)	John Hart, Ramsey Hazbun, David Eldridge, Ryan Hickey, Nalin Fernando, Thomas Adam, Stefan Zollner, James Kolodzey
Volume of serial or monograph	604
Page range of portion	23–27
Publication date of portion	2016
Rights for	Main product
Duration of use	Life of current edition

Creation of copies for the disabled	yes
With minor editing privileges	yes
For distribution to	Worldwide
In the following language(s)	Original language of publication
With incidental promotional use	no
Lifetime unit quantity of new product	Up to 499
Made available in the following markets	academia
The requesting person/organization	John Hart, University of Delaware
Order reference number	
Author/Editor	John Hart
The standard identifier of New Work	TSF
The proposed price	$0
Title of New Work	The Growth and Characterization of Group IV Alloys for Near and Mid-IROptoelectronics
Publisher of New Work	Proquest
Expected publication date	Jan 2017
Estimated size (pages)	197

Note: This item was invoiced separately through our **RightsLink service.** More info **$ 0.00**

Total order items: 1 **Order Total: $0.00**

Figures in Chapter 8 were originally published in the Journal of Applied Physics, volume 119(9), page 93105 in 2016.

AIP PUBLISHING LLC LICENSE TERMS AND CONDITIONS

Dec 11, 2016

This Agreement between John T Hart ("You") and AIP Publishing LLC ("AIP Publishing LLC") consists of your license details and the terms and conditions provided by AIP Publishing LLC and Copyright Clearance Center.

License Number	4006191010660
License date	Dec 11, 2016
Licensed Content Publisher	AIP Publishing LLC
Licensed Content Publication	Journal of Applied Physics
Licensed Content Title	Temperature varying photoconductivity of GeSn alloys grown by chemical vapor deposition with Sn concentrations from 4% to 11%
Licensed Content Author	John Hart,Thomas Adam,Yihwan Kim, et al.
Licensed Content Date	Mar 4, 2016
Licensed Content Volume Number	119
Licensed Content Issue Number	9
Type of Use	Thesis/Dissertation
Requestor type	Author (original article)
Format	Print and electronic
Portion	Excerpt (> 800 words)
Will you be translating?	No
Title of your thesis / dissertation	THE GROWTH AND CHARACTERIZATION OF GROUP IV ALLOYS FOR NEAR TO MID-INFRARED DETECTORS
Expected completion date	Jan 2017
Estimated size (number of pages)	194
Requestor Location	John T Hart 140 Evans Hall University of Delaware NEWARK, DE 19711 United States Attn: John T Hart
Billing Type	Invoice
Billing Address	John T Hart 140 Evans Hall University of Delaware NEWARK, DE 19711 United States Attn: John T Hart
Total	0.00 USD
Terms and Conditions	